Università Ca'Foscari Venezia

**Scuola Dottorale di Ateneo
Graduate School**

**Dottorato di ricerca
in Scienze Chimiche
Ciclo XXVIII
Anno di discussione 2015**

Ensembles of Nanoelectrodes as Electrochemical and Electrochemiluminescence Sensing Platform for Molecular Diagnostics

Tesi in co-tutela con l'Università di Bordeaux, Francia

**SETTORE SCIENTIFICO DISCIPLINARE DI AFFERENZA: CHIM/01
Tesi di Dottorato di Henok Baye Habtamu, matricola 956026**

Coordinatore del Dottorato

Prof. Maurizio Selva

Tutore del Dottorando

Prof. Paolo Ugo

Prof. Neso Sojic

Università Ca'Foscari di Venezia

Dottorato di Recerca in SCIENZE CHIMICHE 28° Ciclo

Université de Bordeaux

École Doctorale des Sciences Chimiques

November 2015

ENSEMBLES OF NANOELECTRODES AS ELECTROCHEMICAL AND ELECTROCHEMILUMINESCENCE SENSING PLATFORM FOR MOLECULAR DIAGNOSTICS

A thesis submitted for the degree of

Doctor of Philosophy

By

HENOK BAYE HABTAMU

Supervisors: **Prof. Paolo Ugo**

Prof. Neso Sojic

Acknowledgments

My honored supervisor Professor Paolo Ugo is the person to whom I would like to express my sincere and utmost gratitude for giving me the opportunity to pursue my PhD study in his prominent research group and in the co-tutoring program between Ca'Foscari University of Venice and University of Bordeaux. He has constantly provided me inspiration, motivation, encouragement and stimulation to work smarter during the entire course of the study. I believe most of his supports are beyond his supervisory responsibility.

My deepest gratitude goes to my co-supervisor Professor Neso Sojic for accepting me in the co-tutoring program, for allowing me to use his excellent lab facilities and to have experience in his prominent research group. I would also like to appreciate his rich capability of solving scientific problems, his continuous follow-up, encouragement and support especially during my stay in Bordeaux.

I would like to acknowledge all previous and present members of the group of electrochemical sensors of Ca'Foscari University of Venice as well as NSYSA laboratory of University of Bordeaux. In particular: Prof. L. M. Moretto, Dr. M. Silvestrini, Dr. M. Ongaro, Dr. A. Stortini, Dr. M. Sentic, Dr. S. Arbault, A. Karajic and A. Simon-Lalande.

I am grateful to Prof. Tarciso Not and Dr. Luigina De Leo for their continuous material and technical support.

Special thanks go to Dr. Francesca Guidi for her indispensable support in facilitating administrative, academic and social issues. She is so kind and always supportive.

I would also like to acknowledge the Region of Veneto, Doctoral School of Ca'Foscari University, PRIN project, Erasmus Placement program and ISM of University of Bordeaux for providing me financial support.

This list would be incomplete without acknowledging the loving support of my family. I would like to extend my heartfelt gratitude to my beloved wife Bethelhem Zewdu Demeke, and my daughter Afomeya Henok Baye for their unconditional love, support and encouragement.

Table of Contents

List of Abbreviations

a.u.	Arbitrary unit
A_{act}	Electroactive area (cm^2)
Ab	Antibody
AFM	Atomic force microscopy
Ag	Antigen
A_{geom}	Geometric area (cm^2)
BP	Prussian blue
BPS	Phosphate buffer saline
bpy	Bipyridyl
BQ	Benzoquinone
BSA	Bovine serum albumin
C	Concentration
CCD	Charge coupled device
CD	Celiac disease
C_{dl}	Double-layer capacitance ($\mu F\,cm^{-2}$)
CE	Counter electrode
CV	Cyclic voltammogram
D	Diffusion coefficient ($cm^2\,s^{-1}$)
DBAE	2-(dibutylamino) ethanol
DGPAs	Deamidated gliadin peptide antibodies
DL	Detection limit
DMSO	Dimethylsulfoxide
DPV	Differential pulse voltammetry/voltammogram
e^-	Electron
E	Potential
$E_{1/2}$	Half wave potential
ECIS	Electrochemical immunosensor
ECL	Electrochemilumunesence/Electrogenerated chemiluminescence
EDS	Energy dispersive X-ray spectroscopy
EIS	Electrochemical impedance spectroscopy

ELISA	Enzyme-linked immunosorbent assay
EMAs	Endomysial antibodies
EMCCD	Electron multiplying charge coupled device
F	Faraday constant (C mol^{-1})
f	Fractional electrode area
FA$^+$	(Ferrocenylmethyl)trimethylammonium cation
FAD	Flavin adenine dinucleotide
FEIA	Fluoroenzyme immunoassay
FE-SEM	Field emission scanning electron microscope
FT-IR	Fourier transform infrared
GC	Glassy carbon
GDP	Guanosine diphosphate
GFD	Gluten free diet
Gln	Glutamine
GOx	Glucose oxidase
GTP	Guanosine triphosphate
H$_2$Q	Hydroquinone
HER2	Human epidermal growth factor receptor 2
HIV	Human immune virus
HLA	Human leukocyte antigen
HRP	Horseradish peroxidase
h-tTG	Human tissue transglutaminase
i	Current
i_c	Double-layer charging currents
I_{cat}	Catalytic current
IDDM	Insulin dependent diabetes mellitus
i_F	Faradaic current
IgA	Immunoglobulin A
IgG	Immunoglobulin G
I_{net}	Net current
i_p	Peak current
I_{pa}	Anodic peak current

I_{pc}	Cathodic peak current
IUC	Intensive care unit
IUPAC	International union of pure and applied chemistry
$k°$	Standard charge transfer rate constant
kDa	Kilo Dalton
K_m	Michaelis–Menten constant
K_m^{app}	Apparent Michaelis–Menten constant
$k°_{app}$	Apparent rate constant
M	Molarity
m	slope
MEA	Microelectrodes array
Med	Redox mediator
NEEs	Nanoelectrode ensembles
MNEA	Micro-/Nano-electrodes array
P	Product
PAA	Polyanthranilic acid
PBE	Partially blocked electrode
PBS	Phosphate buffer saline
PC	Polycarbonate
pI	Isoelectric point
PMT	Photomultiplier tube
PPY	Polypyrrole
PVP	Polyvinylpyrrolidone
QDs	Quantum dots
r	Pearson's coefficient
r	Radius
R^2	Correlation coefficient
RB	Red bull
RE	Reference electrode
RIA	Radioimmunoassay
r_s	Spearman's correlation
RSD	Relative standard deviation

S	Enzyme substrate
SA	Streptavidin
SD	Standard deviation
Sec-Ab	Secondary Antibody
SEM	Scanning electron microscopy
TOF-SIMS	Time of flight secondary ion mass spectrometry
TPrA	Tri-n-propylamine
tTG	Tissue transglutaminase
U	Unit
v	Scan rate
V	Volt
ΔE	Peak potential separation
λ	Wavelength
σ_b	Blank standard deviation

Summary

This thesis primarily describes the development and evaluation of novel electrochemical (EC) and electrogenerated chemiluminescence (ECL) biosensors for molecular diagnostics using nanoelectrode ensembles (NEEs).

NEEs are electrochemical devices composed of random arrays of electrodes each possessing at least one dimension less than 100 nm. Au NEEs can be reliably prepared using easily accessible facilities *via* electroless synthesis of metallic gold into commercial track-etched nanoporous polycarbonate (PC) membrane. The dimensions, density, shape and distribution of the nanoelectrodes is determined by the nanopores of the template. NEEs are attracting enormous attention for biosensors application primarily due to their peculiar electrochemical and analytical advantages, and their promising prospects for designing miniaturized and multiplexed biosensors. The dual surface composition of the NEEs is demonstrated to offer special biosensor platform where the insulating PC part serves for immobilization of the biomolecules, while the electroactive Au nanodisks support the electrochemical reaction.

In this work, NEEs are prepared, functionalized and tested to develop enzymatic and affinity sensors suitable for advanced molecular diagnostic purposes, namely development of a miniaturized glucose biosensor and preparation of novel EC and ECL immunosensors for celiac disease diagnostics.

For the first goal, a second generation enzymatic microbiosensor was developed exploiting the advantageous properties of the NEEs (Chapter 2). The micro-NEE glucose biosensor (overall radius of 400 μm) was obtained by immobilizing glucose oxidase (GOx) on the nonconductive PC component of the NEE, while the Au nanoelectrodes were used exclusively as transducers. The (Ferrocenylmethyl)trimethylammonium cation (FA$^+$) was used as the redox mediator. The proposed biosensor showed outstanding analytical performances with a detection limit of 36 μM for glucose.

The second goal concerns celiac disease (CD) diagnostics. CD is a chronic small intestinal autoimmune enteropathy triggered by exposure to dietary gluten in genetically predisposed individuals. The prevalence rate in the general population is about 1 %; but the incidence rate is dramatically increasing over time. People with CD exhibit abnormally high blood levels of anti-

tissue transglutaminase (anti-tTG) antibodies, suitable as biomarkers for its diagnosis. Existing serological diagnostic techniques lack the desired level of sensitivity and specificity so that a confirmatory biopsy test is required. To overcome this limitation, EC and ECL immunosensors are proposed and studied.

The two kinds of immunosensors employ the same biorecognition platform, based on tTG as biorecognition element and NEEs as electrochemical transducers. The EC and ECL sensors differ in the type of label used to develop the detection signal, and the method of signal detection. By exploiting the high affinity of PC for proteins, the capture antigen tTG is at first immobilized on the PC of the NEEs obtaining tTG–NEEs, which can capture the anti-tTG antibodies.

For EC detection, the bound anti-tTG is reacted with a secondary antibody labeled with horseradish peroxidase, so that signal is detected using H_2O_2 as enzyme substrate and hydroquinone as redox mediator to generate the detection signal (Chapter 3).

For ECL detection (Chapter 4), following the capture of anti-tTG, the immunosensor is reacted with a biotinylated secondary antibody to which streptavidinated $Ru(bpy)_3^{2+}$ luminophore can be bound. In this design, the electrochemical reaction and the location of the immobilized biomolecules where ECL is emitted are spatially separated. Application of an oxidizing potential in tripropylamine (TPrA) solution generates an intense ECL, suitable for the sensitive detection of anti-TG, at a potential much lower than the ECL initiated by the electrochemical oxidation of $Ru(bpy)_3^{2+}$. Since the luminophore does not undergo direct electro-oxidation at the surface of the nanoelectrodes, the ECL signal is generated only by the TPrA electro-oxidation. Note that TPrA acts as redox mediator and ECL co-reactant. Both EC and ECL sensors are applied to human serum samples, showing to be suitable to discriminate between healthy and celiac patients. A comparison between the two approaches indicates that the lowest detection limit, namely 0.5 ng mL^{-1} of anti-TG, is achieved with the ECL immunosensor.

Finally, preliminary results are reported in the appendix on the fabrication, characterization and modification of individually addressable microelectrode arrays, and on the use of lithographically fabricated nanoelectrode arrays for ECL immunosensor.

Organization of the Thesis

A general introduction on electrochemical biosensors and celiac disease (CD) is presented in Chapter 1. Since this work is mainly aimed at developing highly sensitive and specific electrochemical biosensors for diagnosis of CD and associated disorders, the chapter is dedicated to providing relevant background information on electrochemical biosensors, nanoelectrode ensembles (NEEs) transducers and on an emerging ECL detection strategy as well as general review on the disease to which the biosensors are developed.

Chapter 2 presents a new miniaturized glucose sensor developed by immobilizing the enzyme glucose oxidase on the polycarbonate portion of the Au NEEs. This work is included in this thesis because of two main reasons: firstly, since glucose oxidase is commonly used as a model biorecognition element to study new biosensor platforms, we used it to further investigate the effectiveness and reproducibility of proteins immobilization on the PC of miniaturized NEEs without any chemical modification, and secondly, insulin dependent diabetes mellitus (IDDM) is an autoimmune disorder frequently co-exists with CD so that a patient clinically identified to have one of the disorders is advisable to be diagnosed for the other. Therefore, it is quite interesting to develop a full package of biosensors (for both disorders) manufactured in the same way and that operate by the same principle.

Two NEEs based highly sensitive and specific novel immunosensors developed for diagnosis of CD are discussed in Chapters 3 and 4. In both cases the antigen tTG is directly and selectively immobilized on the PC part of the NEEs in order to capture the IgG isotype of anti-tTG. In Chapter 3, the conventional redox enzyme detection strategy using HRP labeled secondary Ab and H_2Q redox mediator are used to develop very stable and low detection limit immunosensor. In order to further enhance the sensitivity, specificity and detection limit of the immunosensor, an ECL detection based immunosensor is developed and evaluated in Chapter 4. ECL is one of the latest commercially feasible detection strategies for biosensors with many extraordinary analytical advantages.

Finally, attempts are made to selectively modify and immobilize biomolecules on homemade individually addressable microelectrode arrays (made up of discarded computer chips) in the intent of developing multiplexed biosensors for CD biomarkers and glucose sensing. The preliminary results are presented in the appendix of the thesis.

Chapter 1

General Introduction

1.1 Electrochemical biosensors

1.1.1 Definition and principles

A comprehensive and widely accepted definition of "electrochemical biosensor" is devised by IUPAC as: "an electrochemical biosensor is a self-contained integrated device, which is capable of providing specific quantitative or semi-quantitative analytical information using a biological recognition element which is retained in direct spatial contact with an electrochemical transduction element" [1].

Electrochemical biosensors are composed of a biorecognition element, transducer (electrode), signal amplification and display systems (Figure 1.1) [2,3].
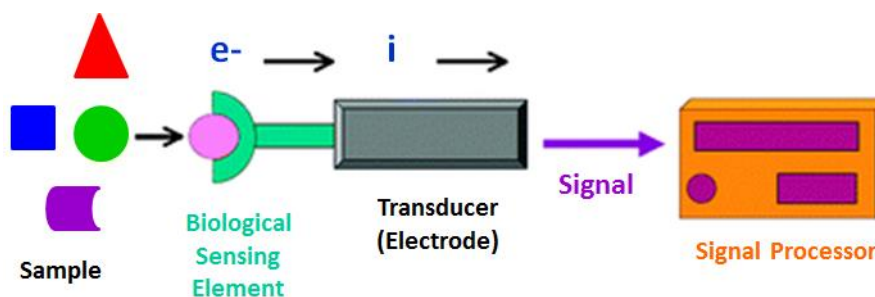
Figure 1.1 Scheme representing main components of a typical electrochemical biosensor.

The biorecognition element is composed of biological entities such as enzymes, antibodies (Ab)/antigens (Ag), proteins, nucleic acids, cells, tissues or receptors that are in direct contact or in close proximity with the transducer and is the part where signal originates from biochemical interactions. It incorporates sensitivity and selectivity to the system, thus minimizing matrix interferences. The transducer in turn, transforms the biochemical output from the biorecognition component into electrical energy (current, potential difference, conductance, capacitance or electrical resistance). The electrical signal depends, which on the concentration of the analyte, is further amplified and displayed as a meaningful output [2-5]. The type of electrode used

determines the sensitivity, cost, potential window, and method of biomolecule immobilization. Inert metals such as platinum, gold and different forms of carbon are most suitable electrodes.

Electrochemical biosensors have been intensively studied and widely applied in various areas, including   public health, drug discovery, food safety, environmental monitoring, forensics and security [5-8].

1.1.2 Classification and applications in medical diagnosis

Electrochemical biosensors can be divided into two categories based on the nature of the biological recognition process, i.e. biocatalytic and bioaffinity. The biocatalytic sensors include enzymes, whole cells or tissue components as recognition elements. They are naturally able to selectively detect the target analyte; in the case of redox enzymes, they can continuously produce or consume electroactive species [1,3]. Bioaffinity sensors, however, rely on the binding of the analyte *via* selective biochemical interaction with the biosensing components such as antibodies, oligo- or poly-nucleotides, or bioreceptors [1,3]. In this format, equilibrium response is monitored since there is no net consumption of the analyte by the immobilized agent [1,3].

The first practically feasible electrochemical biosensor for the determination of blood glucose level was introduced in 1962 by Leland C. Clark, who is considered the father of electrochemical biosensor [9,10]. After incessant efforts, the first commercial electrochemical glucose sensor was released into the market by Yellow Springs Instruments in 1975. Since then, research and applications in the electrochemical biosensors field is experiencing continuous advances and the widespread use of these analytical devices is changing the testing protocols in the health care system. Nowadays, electrochemical biosensors are used worldwide for blood glucose self-analysis; moreover they are widely applied for the detection of some tumor markers, for performing measurements at the single cell level, for real time continuous monitoring of physiological processes [11-13]. Owing to their specificity, speed, portability, low cost, short analysis time and simplicity to operate, electrochemical biosensors are widely accepted in decentralized clinical applications such as in physician's office, intensive care unit (ICU), emergency-room, bedside, and self-testing [12-17]. Unlike bulk techniques, the signal in electrochemical biosensors is localized at the electrode/solution interface making the detection sensitive and suitable for miniaturization. Moreover, the processes do not require (or reduce to a

minimum) sample pretreatment and biosensors can be applied for performing direct analysis even in colored and turbid samples like whole blood, serum or urine [18].

A) Electrochemical enzyme biosensors

The enzyme is usually confined in close proximity with the electrode in order to measure concentration of its substrate, product, inhibitor, substances involved in the *in situ* generation of the substrate or inhibitor, or even an electron transfer mediator [3]. Even when enzymes are immobilized directly onto the electrode, the direct electrons exchange between the two is usually difficult because the active site of most redox enzymes is buried within their tertiary protein structure. Therefore, enzyme-based biosensors often require artificial redox mediators which shuttle electrons between the redox center of the enzyme and the electrode [3].

The success of enzymatic electrochemical sensors is mainly due to excellent selectivity, sensitivity, short response time, low cost and easy preparation and use [19,20]. The enzymatic glucose sensor is the pioneering biosensor and it is used as the comparison benchmark for the development of other biosensors. It is based on the use of glucose oxidase that is a robust enzyme characterized by high turnover rate, excellent selectivity, good thermal and pH stability, low cost [19]. Enzymatic electrochemical biosensors are typically classified into 3 classes (Figure 1.2) on the basis of the mode by which the electrochemical signal is generated [5,6,12,21]. **First generation** biosensors base their functioning on the direct electrochemical detection of either the substrate consumed or product formed during the biocatalysis; obviously, in this case the substrate or the product must be electroactive. In **second generation** sensors, a redox mediator is used to facilitate fast electrons exchange between the enzyme and the electrode as well as to reduce the role of possible interferences. **Third generation** enzymatic biosensors are based on monitoring the biocatalytic process by direct detection of the electron exchange rate between the active site of the enzyme and the transducer (electrode). This approach is applicable only to few redox enzymes and often it requires the use of suitably modified electrode surfaces.
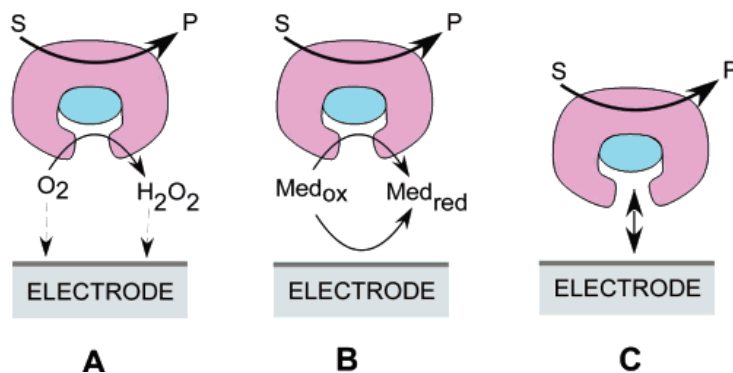
Figure 1.2 Three generations of enzyme electrodes for glucose based on the use of natural oxygen cofactor (**A**), artificial redox mediator (**B**), or direct electron transfer between GOx and the electrode (**C**) [6]. S – substrate, P – product.

Current advanced research on glucose and other enzymatic sensors focuses on the extreme miniaturization of the device and on the development of implantable sensors for *in vivo* monitoring of clinical and physiological parameters.

B) Electrochemical immunosensor

Electrochemical immunosensors are affinity biosensors which perform immunoassays based on Ag and Ab recognition. They have become vital for the determination of biochemical targets relating to health concerns ranging from cancer biomarkers in patient serum to bacterial species in food [2,22,23]. The electrochemical signal is generated directly or indirectly by the binding of the complementary species, typically *via* Ag/Ab interaction [22,23]. Immunological interactions have gained great attention for the development of biosensors thanks to i) their extraordinary specificity and affinity (about three orders of magnitude higher than enzyme-substrate complexes), ii) possibility of production of antibodies including recombinant human for many disease biomarkers, iv) suitability for labeling with reporter substances to monitor the interaction [18]. Even if the direct electrochemical detection of the binding event is possible typically *via* Electrochemical Impedance Spectroscopy (EIS), in the majority of electrochemical immunosensors, detection is performed indirectly using electroactive labels such as enzymes (Figure 1.3) or electroactive probes [18,23-25].
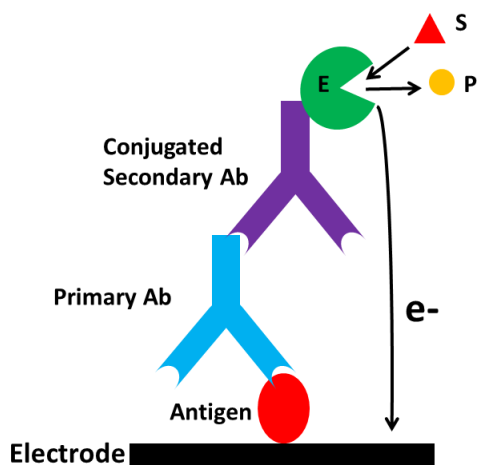
Figure 1.3 Scheme showing the sequential biochemical interactions and signal detection processes in an electrochemical immunosensor. An antigen is used as biorecognition element and signal detection is based on redox enzyme labeled secondary antibody.

In most immunosensor platforms, the label is tagged on to a secondary Ab (Sec-Ab). The use of Sec-Ab to indirectly detect the target Ag/Ab requires more steps than using the primary Ab alone. However, it offers increased sensitivity due to the signal amplification resulting from multiple Sec-Abs binding to a single primary Ab, and in immunosensors where the primary Ab itself is the analyte to be determined [26]. It is worth noting that, often, it is easier and less expensive to bind a label to a Sec-Ab rather than to the target protein. Moreover, many labeled Sec-Abs are commercially available and they can be used for generating signals using different analytical schemes and for different analytes: the selectivity and sensitivity of the method is indeed determined by the specific interaction of the analyte with the primary antibody, the labeled Sec-Ab being added in a final step, after extensive washing of the sensors and consequent removal of possible interferences. The drawback is that this is a delicate and time-consuming procedure.

1.1.3 Biomolecule immobilization strategies

Biorecognition element immobilization is the most important step in biosensor development. It enhances the analytical sensitivity *via* concentrating the detection processes at the electrode-solution interface. Also, it facilitates intermediate washings in order to remove interfering species and excess detection probe [27]. Mechanisms of biomolecule immobilization are

classified into adsorption, entrapment, covalent, cross-linking, self-assembled monolayer and affinity. In addition to these conventional methods, new approaches have been introduced such as hydrogel and sol-gel matrices, lipid membranes, magnetic beads, screen-printing and molecular imprints [27,28]. The immobilization process is practically the most challenging step in biosensor development [9,29]. The choice of a suitable immobilization method depends on the simplicity and reproducibility of immobilization, the nature of the biorecognition element to be immobilized, the type of transducer used, the physicochemical properties of the analyte, the conditions in which the biosensor will be used, and most importantly the biological element should exhibit optimum activity in the immobilized form [9]. Moreover, the biomolecule must be accessible to the analyte, nonreactive towards the host structure and remain tightly bound during the use of the biosensor [9,28].

Biomolecules very rarely form analytically adequate direct binding to electrode surfaces, thus, in the majority of the biosensors, modification of the electrode surface is required prior to the immobilization of biorecognition elements. Some times the modification requires multiple steps and the use of additional reagents [9,30]. The immobilization process on nanoelectrodes is more complex than on macro-electrodes due to two main reasons. i) Due to the very small surface area, biomolecule loading capability is too low. Sophisticated signal amplification system is required to get analytically meaningful response. ii) The electrode surface modification creates an additional diffusion layer that further reduces the feeble overall current at nanoelectrodes [30]. In order to solve these problems, a new biomolecule immobilization approach on the non-conductive polymeric surface of polycarbonate (PC) templated nanoelectrode ensembles (NEEs) is reported (sufficient details and references are provided elsewhere in this document).

1.2 Ensembles of nanoelectrodes

Nanoelectrode ensembles are electrochemical devices composed of randomly spaced electrodes each possessing at least one dimension less than 100 nm, and find application in a wide range of fields, ranging from nanosensors to bio-analytical devices, from energy storage to magnetic materials [31-33].

Miniaturization of electrochemical devices is attracting huge research attention mainly because it reduces cost, eases mass production, improves portability, facilitates multiplexing and automation, lowers sample size, simplifies sample analyses, enhances speed of analysis and reduces invasiveness of implantable devices [34-37]. Electrochemical miniaturization is mainly focused on reducing the size of the working electrode to as low as the nanoscale [4,38,39]. These electrodes offer unique electrochemical properties different from macro-electrodes opening a new research domain [40,41]. The benefits include: i) Electrochemical experiments can be performed in poorly conducting media (even in absence of supporting electrolyte) because ohmic drop is significantly low [4,32]; ii) Double-layer capacitance, a function of the electrode area, is greatly reduced allowing measurements at very fast scan rates; iii) The high rate of mass transport to and from the electrode enhances the signal-to-noise ratio; iv) Very small amount of sample is required; v) Suitable for *in vivo* measurements; and vi) The slow electron transfer rate at nanoelectrode is helpful for studying the kinetics of fast redox processes. All these properties lead to enhanced performances with increased sensitivity and lowered detection limit by orders of magnitudes [4,31,32,42].

Besides the unique analytical and electrochemical advantages of nano-sized electrodes, manufacturing, and controlling of their position, shape and size are major challenges. One method of solving these problems is using template based manufacturing so that the parameters of the nanoelectrodes are well controlled and predetermined by the pores of the host [32,43].

The first template based fabrication of NEEs for electrochemistry was established by Menon and Martin [44-46]. The method relies on precipitation of metallic gold particles into pores of track-etched PC filter membrane producing densely populated random arrays (known as "ensembles") of Au nanofibers with cross-section down to 10 nm [47,48]. This concept has been used for

preparing nanoelectrodes of diameter as small as 2 nm which is quite difficult to achieve with lithographic techniques [49].

The commercial track-etched PC ultrafiltration membranes, used as template, are industrially manufactured by two main steps that determine the pore size, density and geometric alignment [50,51]. The first step is "tracking" of a micrometer thickness PC film either by irradiation from nuclear fission or ion beam to form latent damages that will be transformed to pores. The second step is the "chemical etching" whereby the damaged zones of the latent tracks are chemically removed using alkali solution (KOH or NaOH) forming cylindrical pores [50,52].
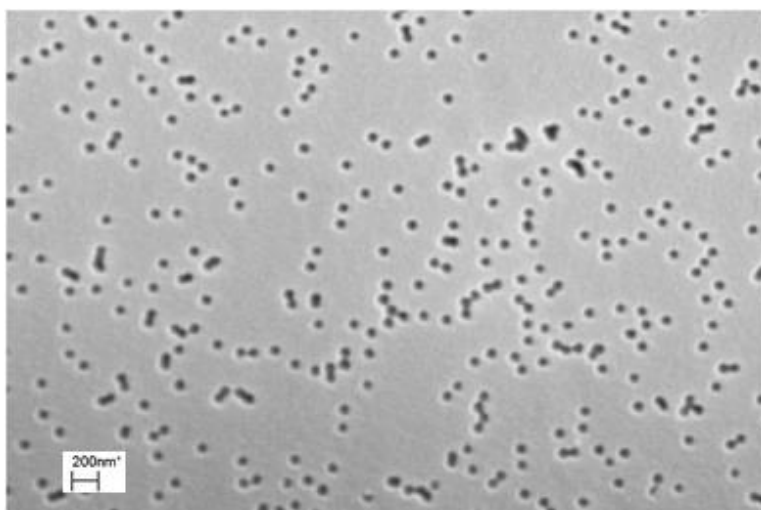
Figure 1.4 SEM image of a commercial track-etched polycarbonate membrane.

The filters can be used as hydrophobic (chemical structure shown below) or rendered hydrophilic by cold plasma activation followed by impregnating with a hydrophilic polymer such as polyvinylpyrrolidone (PVP) [53]. Due to better wettability and suitability for sensitizing by $SnCl_2$, the hydrophilic type is used in electroless fabrication of gold NEEs.

Virgin PC   **PVP**
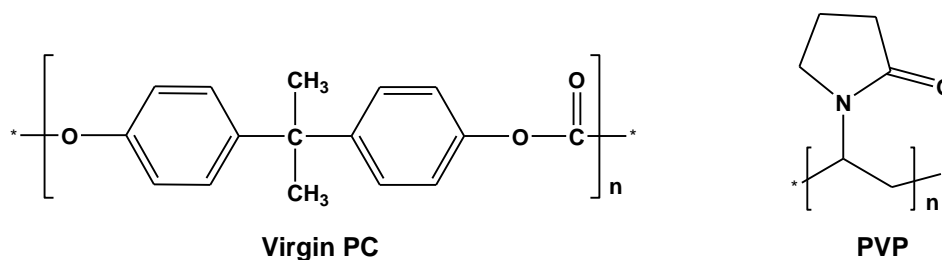
1.2.1 Preparation of Au NEEs

A) Steps in electroless deposition of gold

Electroless synthesis of Au nanowires or nanotubes into nanoporous PC filter membrane involves the following steps as detailed by C. Martin and P. Ugo's groups [44-46,54]: i) *Membrane wetting* – carried out by immersing the membrane in methanol for 2 h. ii) *'Sensitization'* – is an initial chemical process by which Sn^{2+} binds to the amine and carbonyl groups of PVP, both inside the pores and on the two faces of the membrane from $SnCl_2$ hydro-alcoholic solution acidified with trifluoroacetic acid. iii) *'Activation'* – when sensitized membrane is immersed in aqueous ammoniacal $AgNO_3$ solution, the internal walls of the pores and outer faces of the membrane become coated with discrete, nanoscopic metallic Ag particles formed by reduction of Ag^+ by membrane bound Sn^{2+}.
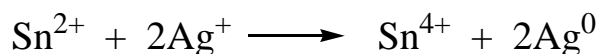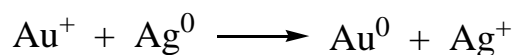
$$Sn^{2+} + 2Ag^+ \longrightarrow Sn^{4+} + 2Ag^0$$

iv) *Gold deposition* – effected by immersion of the activated membrane in to an aqueous Au plating bath (whose temperature is maintained between 0 and 5 ^oC) containing salt of Au^+, Na_2SO_3 and formaldehyde.

$$Au^+ + Ag^0 \longrightarrow Au^0 + Ag^+$$

Catalytic cores of Au metallic particles are formed by galvanic displacement of Ag particles on the pore walls and two sides of the membrane. The Au particles in turn serve as seeds for further reduction of Au^+ using formaldehyde as reductant.

$$2Au^+ + CH_2O + 3OH^- \longrightarrow 2Au^0 + CHOO^- + 2O_2H$$
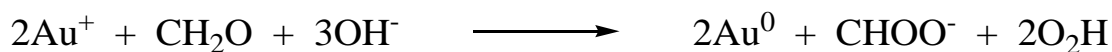
Because the growth of the nanofibers starts from the walls of the pores, termination of the Au deposition after relatively short time produces gold nanotubes. However, if deposition is continued for a period of 24 h, nanowires traversing the whole thickness of the membrane are formed [45,46]. v) *Cleaning* - the membrane bearing the gold is rinsed with distilled water and immersed in 10 % HNO_3 to dissolve residual Ag and Sn.

B) Assembly of NEEs

This process allows to define the shape, size, geometric and active area of the NEE as well as to transform a golden PC membrane into a handy and useful electrochemical device.

Details of the assembly process can be found from Menon and Martin, and Ugo's group [45,55]. Briefly: a piece of membrane bearing the nanowires and thin film of Au on both faces of the membrane is placed partly on a conductive adhesive strip of copper foil and partly on Al foil tape such that the rough face of the membrane faces towards the foils.
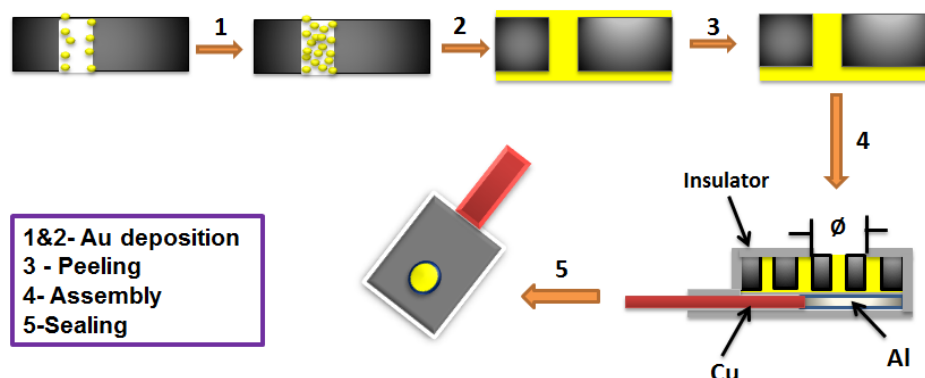
Figure 1.5 The three main steps (gold deposition, peeling and assembly) of manufacturing Au-NEEs using track-etched polycarbonate membrane as template.

Peeling of the Au film from the upper face exposes the disk-shaped heads of nanowires surrounded by the membrane template. These scattered nanodisks offer active electrode surfaces for electrochemical processes. Then, the two surfaces of the assembly are covered with thermo-sealable monokote (a hole that defines the electrode's geometric area is previously punched into the upper piece) in order to insulate the Al and Cu foil tapes. Finally, the junctions between the nanowires and the polymer wall are sealed by heating the electrodes at 150 °C (a little above the glass transition temperature of PC) for 15 min. Efficient sealing of the junctions prevents solution creeping during electrochemical experiments. All nanodisks of the NEE are interconnected by the Au film of the unpeeled face so that they all experience the same applied potential. The copper foil tape serves as a current collector and working electrode lead for the NEE [52,45].

1.2.2 Electrochemical properties

In order to explain the electrons transfer kinetics and mass transport at nanoelectrodes using the existing theories, two important assumptions are made; i) nanodisks of NEEs can be regarded as densely populated very small ultramicroelectrodes, and ii) a NEE can be considered as an electrode with partially blocked surface, that is regular electrode of the same geometric area of the NEE whose large fraction of surface is covered by an insulator [56]. According to Amatore *et al.* model, the current response at partially blocked electrode (PBE) is identical to that at a bare electrode of the same overall geometric area [56]. However, electron transfer kinetics appears slower than at the macro-electrode and is inversely related to the extent of coverage by the insulator. The apparent rate constant (k^o_{app}) at PBE is related to the true standard charge transfer rate constant (k^o) and the fractional electrode area (f).

$$k^o_{app} = k^o\ f$$

The nature of the voltammetric responses at the NEEs is governed by the distance between the neighboring nanodisks, and the experimental time scale which determines the diffusion layer thickness at each element [57-59]. Although intermediate diffusion regimes may occur on tuning the two factors, two boundary conditions can be considered: "total diffusion layer overlap" regime – where the distance between the nanodisks is smaller than the radius of the diffusion layer thickness or the voltammetric measurement time scale is long enough causing complete diffusion layers overlap; or "pure radial" – when separation between nanoelectrodes is larger than the thickness of diffusion layer so that each nanoelectrode behaves independently (Figure 1.6) [31,41,55,57,58,60-62].

PURE RADIAL

$I_{lim} = 4nFDCrA_{geom}q$

TOTAL OVERLAP

$I_p = 2.69 \times 10^5 \, n^{3/2} \, A_{geom} v^{1/2} D^{1/2} C$

Scan rate

Electrode distance

I/nA

E/V

I/nA

E/V
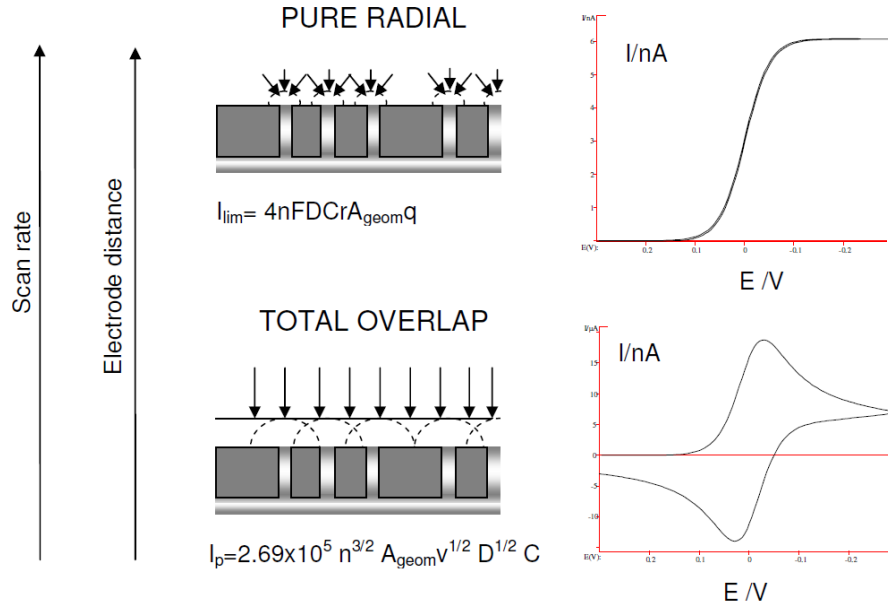
Figure 1.6 Schematic drawings of pure radial diffusion and total diffusion layer overlap regimes at NEEs [52].

The density and the diameter of the nanodisks are determined by the density and diameter of the pores of the membrane template respectively. PC filter membranes with high pore density and pore diameters ranging from 10 nm to 10 μm are commercially available [47,51]. NEEs prepared using these membranes (where all the pores are filled and fibers are intact) operate in the total-overlap response regime forming a planar uniform thickness diffusion layer across the entire geometric area of the NEE. Therefore, they behave like a macrodisk electrode producing peak-shaped CVs, although a large portion of the electrode geometric area is the insulating PC host and only a tiny fraction is therefore electroactive. The faradaic current (i_F) is proportional to the total geometric area (A_{geom}) of the NEE (both polymeric and metallic), while the double-layer charging currents (i_c) are a function of only the electroactive area (A_{act}) [52,60,63]. As a result, the ratio of the faradaic-to-background currents can be as much as 3 orders of magnitude higher than at a macro-electrode of equal geometric area. This is the secrete behind the extremely low detection limits offered by the NEEs [45,51,52,55,64-66].

$$i_C = v C_{dl} A_{act}$$

where C_{dl} is the double-layer capacitance of Au nanodisks and experimentally determined for macro gold electrode to be 21 µF.cm^{-2}, v is the scan rate (V sec^{-1}).

$$i_p = 2.69 \times 10^5 n^{3/2} A_{geom} D^{1/2} C^* v^{1/2}$$

where i_p is the peak current, D is the diffusion coefficient (cm^2 sec^{-1}), C^* is the bulk concentration of redox species (mol. cm^{-3}).

1.2.3 Analytical and bioanalytical applications of NEEs

So far, NEEs are demonstrated to be attractive devices for analytical and bioanalytical applications ranging from trace analysis to biosensor development due to increased sensitivity and lowered detection limits [67]. Although the real-world application of nanoelectrodes is at infancy, they are considered to be promising devices for single cell level studies, real time monitoring of physiological phenomenon and multianalyte sensing [24,39,68,69]. Finding a suitable method of immobilizing biorecognition element without compromising their innate advantages is the key step in the successful development of advanced nanoelectrochemical biosensors. The conventional approaches are based on depositing the biomolecule either on the entire geometric surface or selectively on the gold nanoelectrodes [66,70]. The later requires etching of the PC template to increase the exposed metallic surface maximizing the biomolecule loading. However, as the exposed metallic surface increase, the capacitive current correspondingly increases reducing signal-to-background current ratio [54].

Besides the original functions of the PC membrane for holding, aligning, shape defining, and area determining of the nanoelectrodes, it is recently used as a selective substrate for immobilizing the biorecognition elements of biosensors. By this way, the gold nanodisks are used only for electrochemical transduction [71,72].

Using the new approach, two detection schemes have been established. Scheme A, based on the direct immobilization of the target protein on the PC of the NEE, and scheme B, based on the immobilization of a capture Ab or Ag on PC (Figure 1.7) [73].
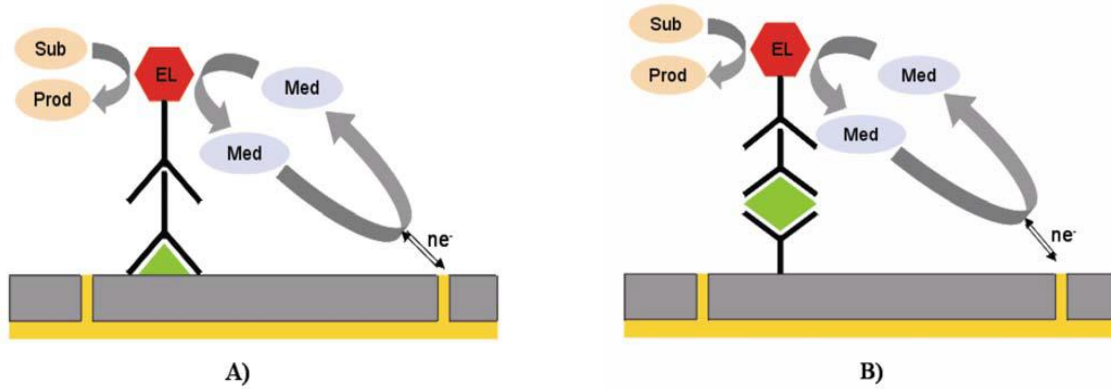
Figure 1.7 Schematic representations of the two possibilities of immunosensor architectures based on selective immobilization on the PC of Au NEEs. **A**) Target protein is directly immobilized, and **B**) the target analyte is captured by an antibody previously immobilized on the PC [73].

A possible drawback of scheme A could be competitive binding of other proteins to the PC surface especially when the sample is composed of complex matrix like in blood.

Further works are in progress in order to enhance the biomolecule loading capability of the PC through plasma or chemical activation to create additional sites suitable for biomolecule binding (–COOH groups) [74,75].

1.3   Electrogenerated chemiluminescence

1.3.1 Definition and developments

Electrogenerated chemiluminescence/Electrochemiluminescence (ECL) is a form of chemiluminescence initiated by electrochemical generation of reactive species that can undergo high-energy electron-transfer reactions to produce excited state luminophore which eventually emits light [76-78]. The overall procedure involves electrochemical, chemical and luminescent processes. The electrochemical process is most important without which the species in the system do not undergo the following cascade of reactions to produce emission [76-78].

Historically, emission of light during electrochemical reactions was first observed in the 19th century [79]. In 1928, Harvey managed to generate light emission from luminol in alkaline solution [80]. After a decade (in 1939), Tamamushi and Akiyama [81] observed flash of light at a Pt cathode immersed in a basic solution containing lucigenin. However, ECL was well understood only after 1964 following a pioneering in-depth explanation by David M. Hercules [82]. A more extensive study on the ECL emission of lucigenin, both in aqueous and non-aqueous media, was reported by Legg and Hercules in 1969 [83]. In the development of ECL, the discovery of $Ru(bpy)_3{}^{2+}$ as water soluble luminophore in 1972 and the emergence of co-reactants in 1977 are considered to be most remarkable [84-86]. These discoveries are important turning points for the application of the technique in the area of bioanalysis [85] which is still on an exponential growth.

1.3.2 Advantages of ECL

Although chemiluminescence (from which ECL evolved) has long been established for analysis of a wide range of compounds, the analytical importance of ECL was recognized only half a century ago. The new technique, ECL, is dominating its ancestor due to the advantages that it offers. Namely [80,85,87], (i) measurement is simple and rapid; (ii) dramatic improvement in sensitivity and limit of detection due to the localization of emission at the electrode interface, and *in situ* recycling of lumuniphore allowing multiple emissions from a single molecule; (iii) wide dynamic range; (iv) requires fewer reagents than chemiluminescence since reactive species can be produced from nonreactive precursor(s); (v) initiation, rate and course of emission can be controlled by manipulating the applied potential to the extent that it can effectively be switched

'on and off'; (vi) the electrochemical process applied to generate reactive species, introduces an additional selectivity and provides further analytical information about the analyte; (vii) multiple luminophore labels can be coupled to biological molecules without affecting immune-reactivity, solubility, or ability to hybridize; and (viii) better for multiplexing through using multiple luminophore labels which have different excitation potential or different emission wavelength, or by controlling the position of emission by interrogating each electrode in an array.

1.3.3 Classification of ECL systems

ECL emission systems can be classified into different classes based on different criteria. This document is limited to describing classifications based on type of luminophore, solvent used and mechanism of emission.

A) Classification based on type of luminophores

So far, three main groups of ECL emitters have been explored: organic, inorganic/metal complexes and nanomaterials [88,89]. The dominance of organic luminophores mainly lucigenin, rubrene and luminol started to decline following the discovery of metal chelate emitters especially $Ru(bpy)_3^{2+}$ by Tokel and Bard in 1972 [86,87,90]. Besides Ru complexes, other transition metal chelates of Os, Ir, Rh, Re, Eu, Pd, and Mo have been discovered to produce ECL [91]. Metal complex emitters are the main interests of researchers due to: First, their attractive electrochemistry, suitable solubility, and stability. Second, they offer broad spectrum of applications by either direct detection of analytes that can serve as co-reactants, or indirect detections using external co-reactant. Third, Ru complexes in particular $Ru(bpy)_3^{2+}$ have caused a paradigm shift in the field of ECL and played pivotal role in the transformation of the technique into practically applicable commercial bioassays. This is because of its high sensitivity, wide dynamic range, rapidness, simplicity, and stability as a label for immune and DNA probe assays. Fourth, metal complexes (example iridium complexes) enable easy color tuning in light emitting devices and multiplex analytical applications [88].

Recently, semiconductor nanocrystals or quantum dots (QDs) have also been exploited as emerging ECL emitters [92,93]. Compared to conventional molecular emitters, QDs own several distinctive merits like size/surface-trap controlled luminescence and good stability against photo-bleaching [94,95].

B) Classification based on type of solvent

Nonaqueous solvent

Early studies of annihilation ECL have almost always been performed in nonaqueous solvents such as N,N-dimethylformamide, tetrahydrofuran or acetonitrile [78,96-98]. The presence of even residual amounts of water and dissolved oxygen quench the ECL reaction. Hence experiments have been usually carried out under dried conditions. The major difficulties of designing ECL systems in aqueous solutions were (i) limited solubility of the organic luminophores, (ii) reactivity of electrochemically generated radical ions with water, and (iii) the limited potential window of water [80,96].

Aqueous solvents

The discovery of water soluble luminophores (e.g. $Ru(bpy)_3^{2+}$ in 1972) with relatively stable intermediates, and the emergence of aqueous co-reactants (oxalate in 1981 was the first) allowed ECL to be generated in aqueous media. This opened a key entry point for a new era of ECL in the field of biosensors [77,99,100]. Since these remarkable discoveries, both components of ECL (luminophores and co-reactants) are being intensively researched and utilized for real world applications.

C) Classification based on mechanism of ECL emission

There are two main mechanisms of ECL emission: annihilation and co-reactant. In both schemes, electrochemically oxidized and/or reduced species combine to generate an excited state that relaxes emitting light [87,101].
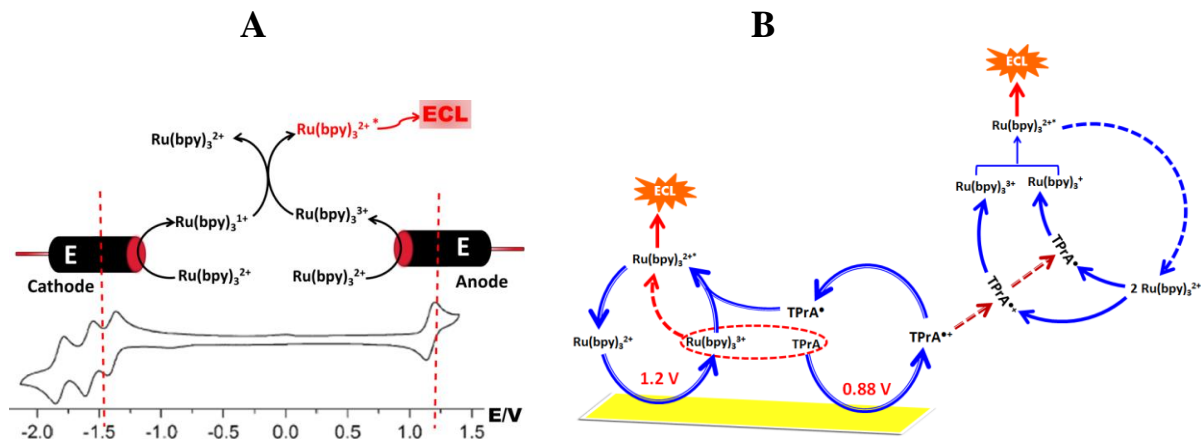
Figure 1.8 Schemes showing annihilation (**A**) and co-reactant (**B**) ECL emission processes by Ru(bpy)$_3^{2+}$ luminophore. "**B**" outlines the electrochemical, chemical and optical processes using TPrA as co-reactant.

Annihilation ECL

ECL is generated from an excited state luminophore produced by energetic electron transfer reaction between electrochemically oxidized and reduced forms of a reagent. These species can be generated either by applying alternating pulse of oxidizing/reducing potentials to a single working electrode, or at two electrodes each set at a reductive or oxidative potential [79,89,101].

In addition to the requirement of an emitter to have both the oxidized and reduced forms, another important drawback of the annihilation processes is the very wide potential window required to simultaneously produce both species. Accordingly, the solvent and supporting electrolyte need to have a potential window wide enough to permit both the oxidation and reduction processes. For example, ECL generation from the well-known Ru(bpy)$_3^{2+}$ *via* annihilation route requires application of either pulses of potentials at around +1.2 and -1.4 V *vs* Ag/AgCl, or cycling the potential between these values to produce the reactive intermediates (Figure 1.8A). This is why almost all early ECL reactions have been carried out in organic solvents [84,87].

Co-reactant ECL

A co-reactant is a sacrificial reagent that after electrochemical oxidation/reduction may undergoes chemical transformation to form a strong reducing/oxidizing intermediate that can either react with the luminophore directly, or after electrochemical oxidation or reduction of the

luminophore. The chemical reaction between the two species produces excited state luminophore that eventually relaxes emitting light (Figure 1.8B) [79,101,102,103].

The invention and practical application of co-reactants offered distinct benefits over the annihilation ECL [77,87]. Namely, (i) since the reactive species of the luminophore and the co-reactant are generated in a narrow potential window, only a single potential step or unidirectional sweep is sufficient to initiate emission (this property permitted the use of solvents of narrow potential window like water), (ii) suitable for luminophores that can undergo only electrochemical reduction or oxidation, (iii) amenable for luminophores producing unstable radicals (this is due to the reason that the potentials required to produce radical ions from the luminophore and the co-reactant are close to each other avoiding the lag time in producing reactive species), (iv) generates more intense emission from systems whose annihilation ECL is less efficient, (v) less prone to quenching of atmospheric oxygen, and (vi) allows emission in the absence of electrochemical oxidation/reduction of the luminophore at the potential of the co-reactant (e.g. $Ru(bpy)_3^{2+}$/TPrA). These are the main reasons why overwhelming majority of commercially available ECL instruments are based on co-reactant ECL systems [77, 101,104].

Following the discovery of oxalate as the first aqueous ECL co-reactant [96], many compounds have been investigated for the same application. A compound is an ideal ECL co-reactant if; its standard potential is close to the standard potential of the luminophore, its *in situ* generated intermediates are stable for the duration of the ECL measurement, it should not emit light alone, soluble in the solvent used, stable and nontoxic, the reaction of the intermediate(s) with the emitter must be rapid, and the co-reactant itself and the intermediates should not quench the emission [77,79,87].

The tertiary amine tri-*n*-propylamine (TPrA) (E^o = +0.88 V *vs* Ag/AgCl) introduced by Leland and Powell in 1990, is a model co-reactant satisfying many of the requirements. Therefore, it is commonly used in research and commercial devices involving $Ru(bpy)_3^{2+}$ as luminophore [87]. However, toxicity and volatility are its main drawbacks. A more recent nontoxic amine derivative known as 2-(dibutylamino)ethanol (DBAE) is reported to be an excellent substitute to TPrA with about 100× increment in ECL intensity than TPrA [105].

Depending on the nature of the sequential electrochemical and chemical reactions that the co-reactant undergoes prior to reacting with the luminophore, the process can be ''oxidative-

reduction'' or ''reductive-oxidation''. The former expression is used when highly reducing intermediates are generated following electrochemical oxidation of the co-reactant, while in the latter case; highly oxidizing intermediates are produced following the electrochemical reduction [77].

The $Ru(bpy)_3^{2+}$/TPrA system is typical example of oxidative-reduction ECL where TPrA is electrochemically oxidized to $TPrA^{\bullet+}$ which deprotonates to produce a strongly reducing $TPrA^{\bullet}$ [87]. Electrochemical oxidation of $Ru(bpy)_3^{2+}$ is not always necessary for ECL emission. Therefore, anodic potential sweeping of this ECL system emits at two distinct potentials (Figure 1.9A) *via* four possible pathways (Figure 1.9B) [106,107]. Except in Scheme 1 (Figure 1.9B), in the other pathways electrochemical oxidation of $Ru(bpy)_3^{2+}$ is mandatory for the ECL emission.
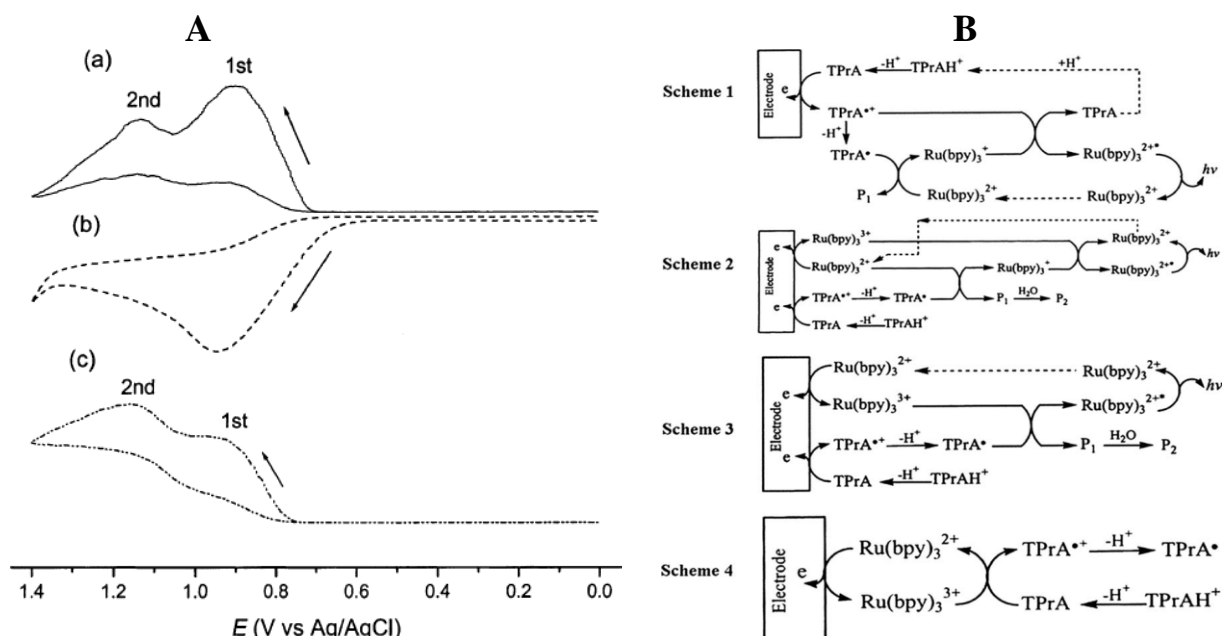
Figure 1.9 A) ECL (a) and cyclic voltammogram (b) of 1.0 nM $Ru(bpy)_3^{2+}$ in the presence of 0.1 M TPrA with 0.1 M Tris/0.1 M $LiClO_4$ buffer (pH= 8) at a 3 mm diameter GC electrode at a scan rate of 50 mV s^{-1}. (c) As (a) but with 1.0 μM $Ru(bpy)_3^{2+}$; and **B**) Schemes representing the four different routes of ECL emission by $Ru(bpy)_3^{2+}$/TPrA system [106].

The first ECL peak (< +1.0 V *vs* Ag/AgCl) is initiated exclusively by electrochemical oxidation of TPrA followed by subsequent reactions between the co-reactant radicals ($TPrA^{\bullet+}$ and $TPrA^{\bullet}$) and the bulk $Ru(bpy)_3^{2+}$ to produce $Ru(bpy)_3^{2+*}$ unlike the second peak (at > +1.0 V *vs* Ag/AgCl) which requires simultaneous electrochemical generation of $Ru(bpy)_3^{3+}$ [106,108,109].

It seems that the low potential ECL is initiated by the reaction between the diffused reactive radicals of TPrA and the $Ru(bpy)_3^{2+}$ found at a distance from the electrode surface while the second peak could be due to the reaction of the radicals with $Ru(bpy)_3^{3+}$ at the electrode interface. The fact that electrode surface modifications that hamper electrochemical oxidation of $Ru(bpy)_3^{2+}$ or facilitate TPrA electro-oxidation enhanced the intensity of the first ECL wave [110,111] as well as the high sensitivity of microbead based commercial ECL biosensors, give a clue on the effect of the distance of $Ru(bpy)_3^{2+}$ from the electrode surface on the intensity and potential of ECL [112]. When the luminophore is within electron tunneling distance (*ca.* $1 - 2$ nm), it possibly undergoes electrochemical oxidation resulting in a dominant emission at the oxidation potential of $Ru(bpy)_3^{2+}$. Conversely, when the luminophore is out of the electron tunneling distance but not greater than about 6 µm (maximum distance that TPrA radical cation can diffuse before deprotonation), the intensity of the first ECL peak dominates.

The fact that the first ECL emission intensity is stronger for sub-micromolar concentration of $Ru(bpy)_3^{2+}$ [106,113], is an excellent privilege for developing ECL biosensors operating at lower detection potential. Because, in electroanalytical techniques using low potential offers benefits including; reduced interference from side reactions particularly in samples of complex matrix (e.g. blood), reduces the noise arising from the reaction between $Ru(bpy)_3^{3+}$ and hydroxide [113], lowers damage on susceptible proteins and oligonucleotides [87], and avoids oxide layer formation on Au and Pt electrodes enhancing analytical reproducibility [104,110,111,114].

1.3.4 Tris-(2,2'-bipyridyl)Ruthenium(II) as luminophore

$Ru(bpy)_3^{2+}$, an orange light emitter ($\lambda = 620$ nm), is the most thoroughly researched and adopted for commercial ECL devices [86]. ECL assays based on this emitter have been widely used in the areas of clinical diagnostics [87], food and water testing [115], environmental monitoring, biowarfare agent detection, and forensics [87].

This is for reasons including strong luminescence, solubility in both aqueous and nonaqueous media, strong emission at physiological pH, undergoes reversible one-electron transfer reactions at easily attainable potentials, formation of stable reduced and oxidized species, high sensitivity, suitability for both oxidative-reduction and reductive–oxidation co-reactants, low background signal, regenerability at the electrode surface and suitability for immobilization in different

matrixes to construct ECL sensors [116,117]. By introducing reactive groups on the bipyridyl, $Ru(bpy)_3^{2+}$ can be easily attached to biologically important molecules such as antibodies, haptens, and nucleic acids, where it serves as a label for detection of analyte binding [84,118-120]. Chemical structures of some commercially available derivatives are shown in figure 9. These modifications do not alter the luminophoric properties of $Ru(bpy)_3^{2+}$ [84,85,94].
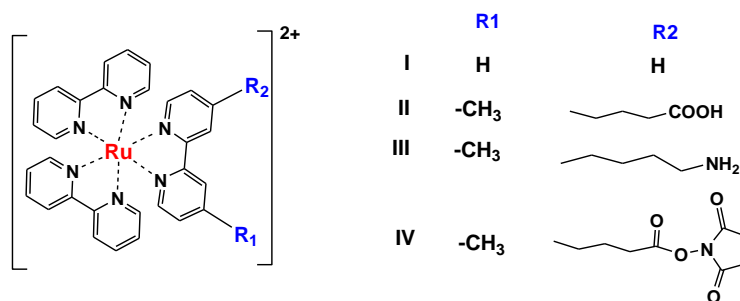
Figure 1.10 Structures of $Ru(bpy)_3^{2+}$ and its derivatives suitable for covalent binding on biomolecules [84,85,94].

Although, kinetics studies revealed that $Ru(bpy)_3^{2+}$ is one of the most efficient luminophores with an ECL efficiency (photons produced per redox event) of 5 %, recently more efficient emitters of Ir complexes are reported [80,121-125]. Most importantly, by changing the ligand identity or composition of Ir, it is possible to tune the frequency of luminescence and quantum yields. This is one of the drawbacks of Ru complexes which hamper their application in multiplexed biosensors [89,103,122-125].

1.3.5 Factors affecting $Ru(bpy)_3^{2+}$/TPrA ECL intensity

The ECL intensity of this system strongly depends on:

- *Solvent polarity* – hydrogen bonding and dipole forces positively influence the intensity of emission *via* their effect on ground- and excited- state properties of emitters [87].

- *Solution pH* – maximum ECL intensity occurs at pH 7.5 (Figure 1.11). In strongly acidic condition, deprotonation of the radical cation of TPrA will be suppressed while in strongly basic media, the background signal resulting from the reaction of $Ru(bpy)_3^{3+}$ and OH^- will be high [87,94].

Figure 1.11 Effect of pH on the ECL intensity of Ru(bpy)$_3^{2+}$/TPrA system [79].

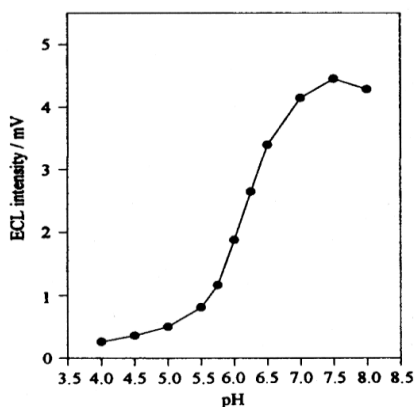- *Electrode material* – intensity of emission is stronger at GC electrode than at Pt and Au electrodes where surface oxide layer formation inhibits electrochemical oxidation of TPrA [87].

- *Electrode surface modification* – hydrophobic modifications facilitate the oxidation of the TPrA resulting in increased ECL intensity [107,110].

- *Dissolved oxygen* – when TPrA concentration is low, the intermediates will be effectively intercepted by oxygen before reaching to the luminophores found far from the electrode but are responsible for the first ECL wave [87].

- *Halogen ions* – halides are shown to inhibit oxide layer formation on Au and Pt electrodes enhancing electro-oxidation of TPrA and ECL emission [107].

1.3.6 Instrumentation and ECL detection

A typical ECL instrumentation includes a potentiostat for applying an appropriate ECL initiating electric potential, and an optical detection system housed in a dark chamber [77]. Optical detection is carried out either by measuring the emitted light intensity (for quantitative analysis) or imaging the emission (for qualitative analysis). A photomultiplier tube (PMT) biased at a high voltage with a high voltage power supply, a photodiode or a charge coupled device (CCD) can be used [76,79,87,126]. Recently, the use of smart phones and sensitive photo cameras are reported for ECL imagining giving an excellent prospect for decentralized use of the technique [127,128].

1.3.7 ECL biosensors in clinical testing

Following the successful generation of ECL in aqueous media especially at physiological pH, tremendous effort has been made on the practical application of the technique in the determination of wide range of bioanalytes. So far, clinical diagnosis is the most successful commercial application of ECL; the majority relying on $Ru(bpy)_3^{2+}$ and its derivatives as emitters and TPrA as the co-reactant [77,89,90,129,130]. Since most of the biological targets of clinical interest are not ECL-active, ECL tags are required to label the biomolecules with $Ru(bpy)_3^{2+}$ derivatives or in limited cases the analytes themselves can serve as co-reactants [90,94,111].

Although initial interest of exploiting ECL in the clinical arena arise because of capability to detect very low concentrations of biomarkers, during the development, it was revealed that the technique provides maximum specificity and sensitivity by combining spectroscopic and electrochemical techniques with that of biologicals such as antibody-antigen and DNA. So far, many ECL methods of clinical interest have been developed including diagnostic methods for different type of cancers, HIV, cardiac problems and for different pathogenic microbes [15, 129,131-135]. To date, more than 150 magnetic bead based ECL immunoassays have been commercialized [76,87,90,136].

1.4   Celiac Disease

1.4.1 Definition

The term celiac disease (CD) was derived from a Greek word "*koeliakos*" meaning "*suffering of the bowels*" [137]. It is defined as a chronic small intestinal immune-mediated enteropathy triggered by exposure to dietary gluten in genetically predisposed individuals [138,139].

1.4.2 Brief history of celiac disease

The first written document on CD was found in the manuscript of Aretaeus (in the 2nd century) in which it is described as a bowl discomfort associated with diarrhea and malabsorption [138,140]. In 1888, Samuel Gee published a detailed clinical description in a compilation known as "Coeliac Affection" where he recommended avoiding starch from food [140]. The exact cause of the disease was unexplained until Willem K. Dicke identified that the toxic "factor" in wheat and barley causing intestinal dysfunction is a protein [141]. Initially, he noticed symptomatic improvements of his patients when bread was withdrawn from their diet, due to food shortage during the 2nd World War, but the symptoms resumed when bread was reintroduced. Based on this observation, Dicke initiated a well-designed experiment which proved that wheat, barley, and rye triggered malabsorption is not caused by their starch content but by the prolamin proteins (gliadins) of gluten [137,141-143]. The histological effects of CD on the small intestinal lining were explained by Paulley in1954. Later, Michael N. Marsh (in 1992) designed a histological level of celiac lesions ranging from hyper-proliferative crypts with intraepithelial lymphocytosis to total villous atrophy [141,144]. Also, the year 1961 was remarkable due to the identification of anti-gliadin antibodies as the first noninvasive serological markers for CD [138,140]. In 1997, tissue transglutaminase (tTG) was identified as an autoantigen of CD permitting development of anti-tTG IgA based ELISA test method [145].

1.4.3 Prevalence of celiac disease

CD has long been considered to be a rare health problem affecting only societies of the western world [146,147]. However, it is recently recognized as a global health problem affecting all societies irrespective of age, gender and race [147,148]. Incidences of the disease have been reported even from countries whose staple diet is not wheat [147,149]. Large scale screening

studies and projections based on clinically identified cases show that the current average global prevalence is around 1% (Figure 1.12), with dramatically increasing trend [140,149-151]. Unexpectedly high prevalence rates are reported from countries like Finland and Algeria [152].
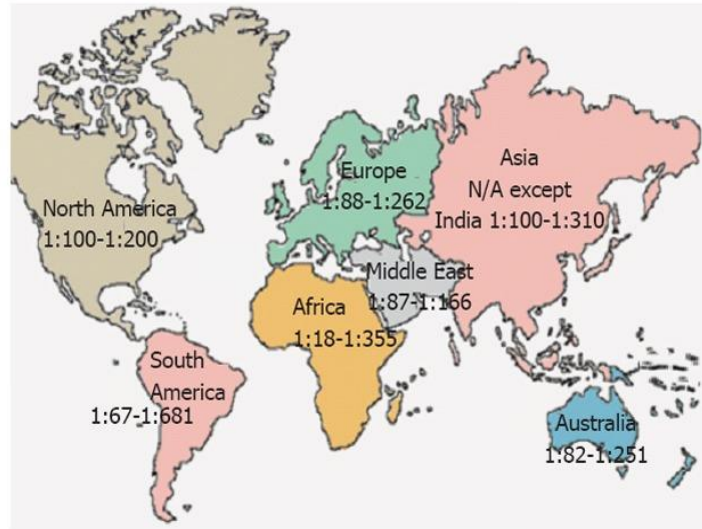
Figure 1.12 Worldwide prevalence of celiac disease [147]. N/A: not available.

1.4.4 Pathogenesis

Genetic, immune and environmental factors are mandatory for manifestation and maintaining CD [148,150,151,153-155].

Gluten

Other environmental factors

Gliadin

Epithelial absorptive cells

Increased intestinal permeability

Villous atrophy
Crypt hyperplasia
Intraepithelial lymphocytosis

Overexpression of interleukin-15

Tissue transglutaminase

Intraepithelial lymphocytes

Deamidated gliadin

TCR

CD4 T cell

Cytokine release

Lamina propria

HLA-DQ2

B cell

Antigen-presenting cell

Genetic factors

Antibodies (antigliadin, antiendomysial, and tissue transglutaminase)

*TCR= T-cell receptor

Figure 1.13 Interactions of gluten with environmental, immune, and genetic factors in celiac disease processes [148].

After cascades of biochemical reactions involving genetic and environmental factors, the body's immune system releases chemicals that damage the small intestinal wall and antibodies against the trigger antigens (Figure 1.13). Based on the extent of the small intestinal damage, Marsh graded the disease conditions into Marsh Type 0, I, II and III (see Table 1.1).

Table 1.1 The modified Marsh classification of gluten-induced small intestinal damage [156].

|	Marsh type	Intraepithelial lymphocytes	Inflammation in lamina propria	Crypt hyperplasia	Villous atrophy
0	Normal mucosa	Normal	Normal	Absent	No
I	Infiltrative lesion	Increased	Normal or mild increase in cellularity	Absent	No
II	Hyperplastic type	Increased	Mild increase in cellularity	Present	No
IIIa	Destructive lesion	Increased	Increased cellularity	Present	Partial atrophy
IIIb	Destructive lesion	Increased	Increased cellularity	Present	Subtotal atrophy
IIIc	Destructive lesion	Increased	Increased cellularity	Present	Total atrophy

A) Environmental factors

The main exogenous trigger factor to CD is gliadin. Gastrointestinal infections, drugs, α-interferon and surgery potentially enhance the permeability of the small intestine to the antigen playing substantial role in the disease process [140,148].

The Role of gluten in the disease development

The term gluten encompasses all prolamine proteins found in wheat (gliadins and glutenins), rye (secalin), barley (hordein) and other related cereals. It is composed of almost equal proportions of gliadin and glutenin. Gliadin is the most potent fraction of gluten in triggering CD [151]. It is alcohol soluble but poorly dissolves in aqueous solvents of neutral pH, which corresponds to its isoelectric point (*ca.* 7.8) [151,157]. The peptides consist of a hydrophilic central domain rich in glutamine (Gln) and proline (Pro), and two hydrophobic terminal domains containing low levels of these amino acids [157].
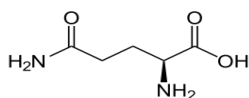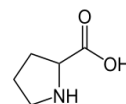
Glutamine   Proline

The Pro renders gliadin resistant to enzymatic breakdown in the proximal small intestine. The intact protein infiltrates in to the lamina propria of the intestine, possibly during intestinal infection or increased intestinal permeability, where its antigenicity to the immune system is increased *via* deamidation by tTG [139,148,150,151,157-160].

B) Genetic factors

The fact that the incidence of CD is significantly higher among twins and relatives of CD patients than in the general population, gives a clue on the involvement of a genetic factor [144]. All CD patients share HLA-DQ2 or HLA-DQ8 alleles as common genetic components [148,151]. However, all individuals carrying the genetic factors do not develop the disease indicating that their presence is necessary but not sufficient [148,160]. It is worth to note that the disease is not caused by gene defect, but rather the collective effect of normally functioning variant gene products [161].

C) Immunological factors

Naturally, the immune system is meant to protect the body from pathogens that can potentially cause disease. The system has special natural selectivity to identify antigens that are not part of either the organism or edible proteins. However, sometimes the system can act against these proteins causing autoimmune and inflammatory diseases. CD is the result of this inappropriate immune response against ingested gliadin and the body's own enzyme tTG stimulating the T-cells to release cytokines (initiate intestinal inflammation, villous atrophy and crypt hyperplasia) and B-cells to excessively release antibodies against gliadin, tTG, and endomysium) [144,145,148,160,161].

1.4.5 Role of tissue transglutaminase in CD

Tissue transglutaminase is a Ca^{2+} dependent (assumes the enzymatically active conformation in the presence of Ca^{2+}) enzyme found in most mammalian tissues including the brain [162-164]. The enzyme is mainly intracellular and is latent during the normal cell lifespan due to the insufficient level of Ca^{2+} and the inhibitory effect of GTP/GDP [165]. In conditions where homeostasis is disturbed by cell stress or trauma, large amount of Ca^{2+} infiltrates into the cell triggering cross-linking of intracellular proteins [162]. Cellular damage caused by mechanical

stress, inflammation or infection, cause the intracellularly confined tTG release outside the cell inducing extracellular functions [155,162-164].

Abnormalities in the level of tTG cause many diseases including CD, neurodegenerative diseases, tissue fibrosis, and cancers [164,166,167]. In celiac patients, tTG has been detected in all layers of the small intestinal wall [161].

Human tTG, a 78 kDa protein (pI 5.3) composed of 687 amino acids, has four structural domains: *N-terminal β-sandwich* - contains the fibronectin and integrin binding site, *catalytic core* -contains the catalytic triad for the acyl-transfer reaction, and *two C-terminal Barrels* (Figure 1.14). The guanine binding site, absent in other transglutaminases is located between the catalytic core and the first α-turn motif [164,168-171].
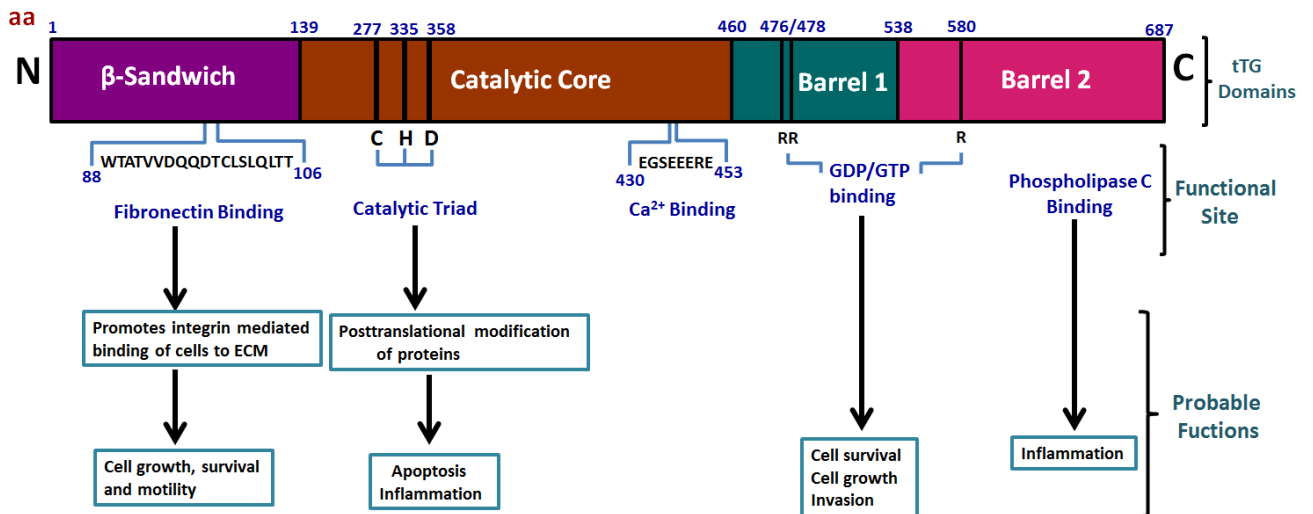
Figure 1.14 The four domains of tTG and proposed functions of each domain [162].

The enzymatically active center bearing cysteine residue is located in a cleft within the catalytic domain. If the enzyme is inactive and unbound to Ca^{2+}, the site is hidden from access to substrates by overlayering the C-terminal domains (''closed'' conformation) whereas, when it is activated, it undergoes remarkable conformational change during which the C-terminal domains move away from catalytic domain, thereby opening access to the active site (''open'' conformation) (see Figure 1.15) [167].

Figure 1.15 X-ray crystal structures of the closed (left) and open (right) conformations of human tTG [168].

The tTG catalyzed proteins' deamidation and transamidation take place when the tTG enzyme is in an open conformation. The enzyme reacts with glutamine of peptides forming a thioester intermediate from which the acyl group is transferred to an amine substrate resulting in crosslinking. In the absence of a suitable amine, water can act as an alternative nucleophile, leading to deamidation of the glutamine residue to glutamate as shown in Figure 1.16 [163,164,168,172].
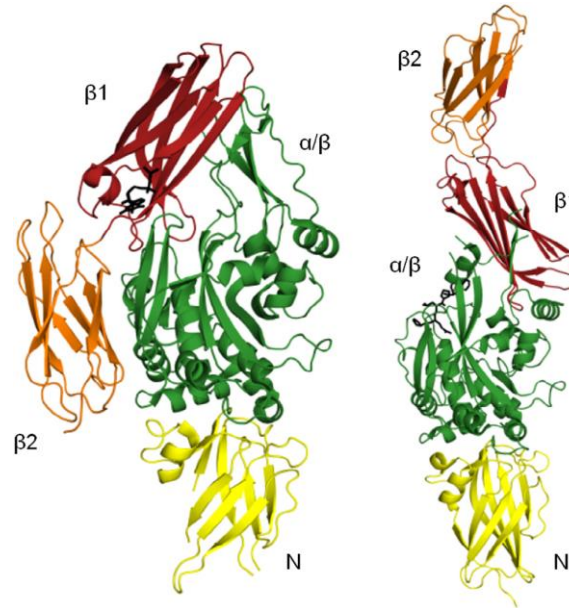
In vitro studies have proved that transamidation is the major reaction. The deamidation reaction takes place when the tTG activity is high, gliadin is in excess, and the level of acceptor amines is low. During episodes of intestinal inflammation, such situations could occur. Inflammation induces tTG activity, disturbs epithelial integrity, and notably increases the need for polyamines, in that cross-linking of polyamines by tTG is critical for normal repair of the intestinal mucosa. Inflammation may thus cause a local depletion of polyamines concurrently with an increased leakage of gliadin across the epithelial barrier [161,173].

Because of its large amount of glutamine residues, gliadin is an excellent substrate for tTG [145,174]. The selective modification of these residues to negatively charged glutamates by tTG

enhances gliadin's affinity to the positively charged pockets of HLA-DQ2 and HLA-DQ8 eventually boosting its antigenicity (Figure 1.16) [139,148,159,160,175-177].
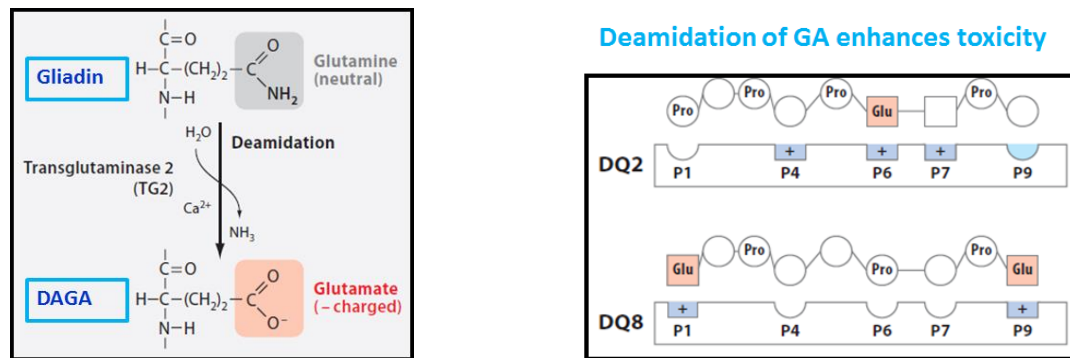

Figure 1.16 Tissue transglutaminase catalyzed gliadin deamidation enhances binding of gliadin peptides to HLA-DQ2. The deamidation generates negatively charged glutamic acid residues from neutral glutamines. The negatively charged residues are preferred at positively charged antigen-binding groves of HLA-DQ2/DQ8 [144].

In addition, intestinal biopsies of CD patients revealed that tTG can cross-link itself to deamidated gliadin forming deamidated gliadin peptide-tTG complexes. This might be the reason why almost all CD patients develop autoantibodies against tTG [144,176]. Although the mechanism by which the autoantibodies develop has not yet been confirmed, it is postulated that the formation of deamidated gliadin peptide-tTG complex causes epitope spreading from gliadin to tTG [172]. Currently, these autoantibodies are the most specific biomarkers for serological tests of CD [178].

1.4.6 Screening, diagnosis and follow-up tests

Diagnosis of CD is complicated due to the variability of clinical manifestations, similarity of symptoms to other disorders, involvement of multiple body systems and majority of patients remain asymptomatic or with mild symptoms [154,179,180]. The symptomatic stage exhibits wide range and mostly nonspecific clinical manifestations. Patients suffer from gastrointestinal symptoms such as diarrhea, flatulence, abdominal discomfort, delayed gastric emptying and heartburn. Many of the extraintestinal symptoms are secondary to malabsorption of nutrients caused by villous damage [151,154].

Currently, clinical diagnosis of CD is based on combinations of patient history, clinical presentations, serology, gene test, histology and improvement of symptoms on gluten free diet [138,140,150,154,181]. An example of CD diagnosis algorithm is shown in Figure 1.17.
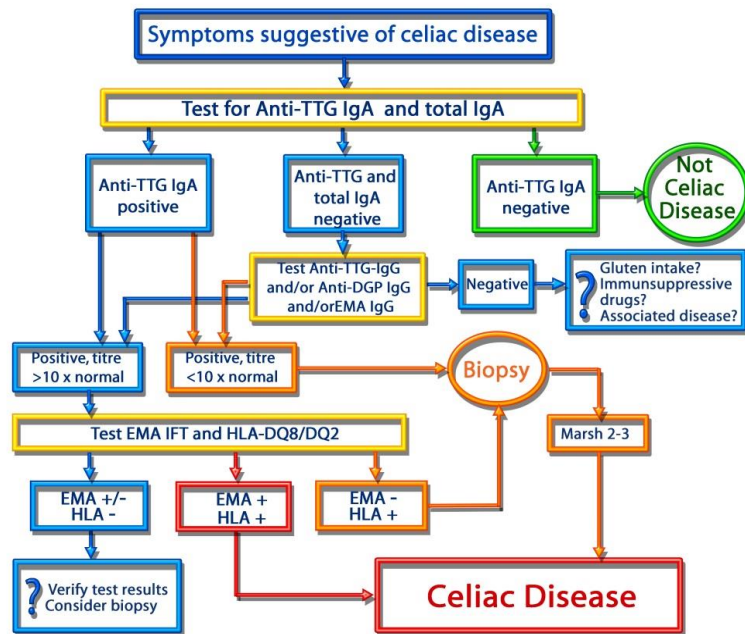
Figure 1.17 A typical celiac disease diagnosis algorithm.

In individuals with characteristic clinical presentations and confirmed HLA-DQ2 or DQ8 alleles, positive CD-specific serology with concomitant confirmatory intestinal biopsy is considered to be the gold standard [154,150,179]. These conditions are mostly observed in the presence of small intestinal villous atrophy and crypt hyperplasia, typical of Marsh III [179].

Screening and follow-up tests are much more complicated than diagnosis of symptomatic CD due to absence of clinical presentations or mucosal healing/disappearance of serum antibodies respectively. In case of nonrefractory CD, follow-up of adherence to GFD is more difficult because of the reduction in the level of the antibodies and intestinal mucosal healing [140]. On the other hand, if the physiological changes after GFD are unrecognized, it can increase the risk of life-threatening complications for example, intestinal lymphoma, cancer, malignant lymphomas, small-bowel neoplasia, oropharyngeal tumors, large intestine adenocarcinomas, infertility, osteoporosis, nutritional deficiencies, stunted growth, psychosocial retardation, impairment of quality of life, increased mortality and additional autoimmune conditions

[182,183]. False positive results, on the other hand, can compromise the life quality of individuals, obliging them to unnecessary, but heavy cautions.

A) Serological test

As shown in Figure 1.13, the body releases abnormally high levels of CD specific antibodies when gliadin infiltrates into the lumina propria of genetically predisposed individuals. The antibodies belong to the IgA or IgG isotypes of anti-gliadin (against gliadin or deamidated gliadin) or anti-self (against tTG and antiendomesial). They are important serological biomarkers for screening, diagnosis and follow-up tests of untreated CD. The specificity and sensitivity of the biomarkers is highly variable ranging from 29 to 100 %. However, combination tests perform better, yielding positive and negative predictive values close to 100 % [179,182].

False positive serological results are mainly attributed to cross-reactivity of the antibodies; but, false negative results may be associated to selective IgA deficiency (occurs in 0.5 to 6 % of CD patients), young children (< 2 years) may not produce some of the anti-self antibodies, as their immune system is not well matured, personal error of antiendomysial test (highly subjective test), and absence of gluten in the patient's diet. Also, autoimmune diseases like insulin dependent diabetes mellitus and hepatitis, enteric infection, congestive heart failure, and chronic liver disease are sources of false positive result [151,154,184].

Historically, the first serological tests were established for anti-gliadins by indirect immunofluorescence assay and ELISA methods. Currently, they are replaced with tests for the determination of antibodies of tTG, endomysium (EMAs) and deamidated gliadin peptides (DGPAs) because of poor sensitivity and specificity [151,178,179,183-186].

Endomysial antibodies bind to endomysium, the connective tissue around smooth muscles. They are determined by indirect immunofluorescence method. In this method, the serum sample is initially incubated with a section of human umbilical cord or monkey esophagus. After further incubation with fluorescein labeled Sec-Ab, the tissue is visually examined by fluorescent microscopy [186]. The result is reported semi-quantitatively as positive or negative. Even though the method is highly sensitive and specific, its clinical uses are limited by the technical difficulty, tediousness, subjectivity, and requirement of highly experienced personnel [184,185,186].

Assays of anti-tTG and anti-DGP antibodies are based on optical ELISA [151,178,179]. The anti-tTG ELISA test was developed following the identification of the tTG against which antiendomysial antibodies are directed [151,178]. It measures the same thing as IgA EMA but with lower cost, and without any subjectivity. Owing to these advantages, serum anti-tTG IgA ELISA test is the most preferred CD test method except in selective IgA deficiency [151,187] and in young children (under 2 years). In these conditions, IgG- tTG or the newer IgG-DGP test methods should be considered or referred to biopsy [154,184,188].

In contrast to biopsy, serological tests are less invasive, simpler, faster, and do not rely on villous atrophy (because the atrophy can be caused by other diseases or may not be completely observed during asymptomatic stages). However, there is a considerable heterogeneity among different reports on the sensitivity and specificity of the different antibodies and their isotypes [182,188].

Also, there is continuing debate on the sole use of non-invasive serological tests to diagnose CD. In fact, usually the clinical, serological, and histological findings coincide and the diagnosis of the disease is straightforward. For example, in cases where the IgA-tTG and -EMA are at high titers with typical symptoms, the probability of identifying a celiac enteropathy with the biopsy test is almost 100%. In this case, the small intestinal biopsy does not add any relevant information for the clinical decision [189]. Based on this practical observation, new guideline is proposed for the diagnosis of the disease [140]. It suggests that in symptomatic patients in whom the IgA-tTG level exceeds 10 times the upper limit of normal, EMA antibodies are positive on a separately taken blood sample, and HLA-DQ2 or -DQ8 are positive, then biopsies do not need to be performed to confirm the diagnosis [140].

In general, serological tests are better for Marsh I patients where biopsy cannot provide definite result [181]. Moreover, serological tests are more useful for screening CD and follow-up of adherence to the GFD. The existing serological tests, on the other hand, require qualified personnel and expensive laboratory facilities, and results are available only after a time delay. Therefore, development of more sensitive, specific, simple and rapid CD diagnostic methods is urgently required. To this goal, electrochemical immunosensors can be most promising [151,179].

B) Biopsy and endoscopy

According to the current CD diagnosis algorithms, biopsy test is initiated for patients with positive serology and clinical symptoms suggesting the disease. In addition, the test is recommended for following-up the outcomes of gluten free diet [190]. During the biopsy procedure, the doctor eases a long, thin tube (called endoscope) equipped with small camera at the end, through the mouth and stomach into the small intestine of sedated or anesthetized patient and take tissue samples [191]. The tissue samples are examined under a microscope for signs of damage. CD is confirmed if the villi are partially or totally flattened. Moreover, drastic reduction of brush border enzymes and elevated number of T-cell lymphocytes (white blood cells) are indicators of the disease [161,179].

Sometimes the histologic damage may not be due to CD, as similar lesions are observed in other disorders including immune disorders, food hypersensitivity, infection, drugs, and neoplasia [140,150,192]. This is the main reason why biopsy is not separately used for confirming the diagnosis and hence the result should be sealed with serological test(s) [140]. The severity and extent of the histologic damage of the proximal small intestine seem to correlate with the intensity of the clinical symptoms. The damage may be mild in atypical or silent cases, with little or no abnormality detectable [150,151].

Major drawbacks of biopsy test are i) lack of specificity to lesion caused by CD, ii) requirement of highly trained personnel, iii) poor patient and operator compliance and iv) invasiveness, discomfort and possible complications limit the use of re-biopsy in routine follow-up [190], v) some CD patients who have been identified by positive serology, may not have villous atrophy.

C) Gluten challenge test

Prior to initiating the lifelong gluten-free diet, diagnosis of CD should accurately be established. The accuracy is finally confirmed by improvement of clinical symptoms, decline in levels of serum antibodies and intestinal mucosal healing following exclusion of gluten from diet. In cases of failure to respond to a gluten-free diet, gluten challenge is the sole option to verify the accuracy of the initial diagnosis [192]. In children under 5 years of age, gluten challenge should be discouraged unless the child is HLA-DQ2 and -DQ8 negative or has been placed on a GFD

without proper testing. The diagnosis of CD is confirmed if CD-specific antibodies become positive and clinical symptoms and/or histological relapse is observed [193].

D) Gene test

The other laboratory test for CD is HLA typing specifically for the DQ2 and DQ8 alleles. These alleles are the major genetic predisposing factors and are stable markers at any disease condition and throughout life. A negative test has a more significant value because, CD almost doesn't occur in their absence so that further diagnostic procedures are unnecessary [140,194]. A positive test indicates only genetic susceptibility but does not necessarily mean the disease development. The strengths of the gene test are non-invasiveness, stability of the biomarker during any disease condition and absolute indicator of negative result. However, its main weaknesses are positive test result is less meaningful and the test cannot be used for follow-up of the disease condition [193].

1.4.7 Celiac disease and insulin dependent diabetes mellitus

Studies have demonstrated elevated prevalence rates of CD among individuals with insulin dependent diabetes mellitus (IDDM). Both disorders share the same genetic factors (DQ2 and DQ8). In average 3.5 to 10 % of individuals with CD develop IDDM and *vice versa*. Screening for the other is recommended in individuals already diagnosed with one disorder. If a subject is suspected of having both disorders, it is advisable to diagnose the IDDM first because it is easier to diagnose and symptoms are more obvious than CD. Most CD patients with associated IDDM, however, do not have typical gastrointestinal symptoms of CD, despite the presence of characteristic intestinal lesions. They are therefore, at risk of remaining undetected and untreated [195-197]. In the future, it could be interesting to develop a full package of biosensors for diagnosis of both CD and blood glucose level [198,199].

1.4.8 Management of celiac disease

The only treatment for CD is a life-long gluten free diet. No food or medication containing gluten from wheat, rye, and barley, or their derivatives can be taken [150,195]. Recently, enormous efforts are being made to develop therapeutic agents that act *via* hydrolyzing gliadin, blocking small intestinal absorption of gliadin, inhibition of tTG, HLA-DQ blocking and restoring immune tolerance to gluten [147,178].

1.5 Goal of the Thesis

Celiac disease is gluten induced chronic autoimmune disorder with a global average prevalence rate of about 1%. Since no curative drug has been introduced into the market, patients should be kept on life-long gluten free diet. Early diagnosis reduces development of refractory cases and associated mortality rate. However, the disease is underdiagnosed mainly because of inaccessibility, unaffordability and complexity of the existing diagnostic procedures especially for communities in developing countries. Furthermore, the existing methods are characterized by high levels of false negative and positive diagnostic results. This imposes the use of complex diagnostic algorithms to confirm the clinical outcome.

After identifying this practical gap, we set a goal to develop simple, cheap, portable, less invasive, accurate and reliable serological diagnostic methods for CD. To this goal, NEEs based electrochemical immunosensors with state of the art sensitive and specific detection strategies are chosen. Besides the profound electrochemical advantages such as increased signal-to-noise ratio and low limit of detection, simplicity of fabrication and biorecognition element immobilization are additional benefits of track-etched PC templated gold NEEs. A reagent free and one step biomolecules immobilization strategy selectively on the PC portion of the electrode is implemented. This novel approach has been demonstrated by our group to enhance biomolecule loading capability without compromising the electrochemical performance of the active metallic surface of the NEEs. On the basis of the clinically proven association between celiac disease and insulin dependent diabetes mellitus, we studied the applicability of NEE-based biosensors also for glucose detection, by focusing on the implementation of a highly miniaturized enzymatic biosensor. Finally, in the field of CD diagnostics, with the aim of developing a highly sensitive analytical method we completed the study by examining the possibility to combine the excellent electrochemical performances of NEEs with the use of one of the most sensitive detection techniques, which is electrochemically induced luminescence.

References

[1]   D. R. Theavenot, K. Toth, R.A. Durst, G.S. Wilson, *Pure Appl. Chem.* 1999, **71**, 2333.

[2]   B. Hock, *Anal. Chim. Acta* 1997, **347**, 177.

[3]   N. J. Ronkainen, H.B. Halsall, W. R. Heineman, *Chem. Soc. Rev.*, 2010, **39**, 1747.

[4]   D. Wei, M.J. A. Bailey, P. Andrew, T. Ryhanen, *Lab. Chip*, 2009, **9**, 2123.

[5]   P. D'Orazio, *Clinica Chimica Acta* 2003, **334**, 41.

[6] J. Wang, *Chem. Rev.* 2008, **108**, 814.

[7] Y. Wang, H. Xu, J. Zhang, G. Li, *Sensors* 2008, **8**, 2043.

[8] M. Pohanka, P. Skladal, *J. Appl. Biomed*. 2008, **6**, 57.

[9] A. Sassolas, L.J. Blum, B.D. Leca-Bouvier, *Biotechnol. Adv.* 2012, **30**, 489.

[10] L. C. Clark Jr, C.A. Duggan, *Diabetes Care* 1982, **5**, 174.

[11] A. Rasooly, J. Jacobson, *Biosens. Bioelectron.* 2006, **21**, 1851.

[12] A. Chen, S. Chatterjee, *Chem. Soc. Rev.* 2013, **42**, 5425.

[13] J. Wang, *Biosens. Bioelectron.* 2006, **21**, 1887.

[14] A. T. Sage, J.D. Besant, B. Lam, E.H. Sargent, S.O. Kelley, *Acc. Chem. Res.* 2014, **47**, 2417.

[15] J. Zhou, N. Gan, T. Li, F. Hu, X. Li, L. Wang, L. Zheng, *Biosens. Bioelectron.* 2014, **54**, 199.

[16] H. Yu, F. Yan, Z. Dai, H. Ju, *Anal. Biochem.* 2004, **331**, 98.

[17] R. K. Kobos, *TrAC Trends Anal. Chem.* 1987, **6,** 6.

[18] J. Yakovleva, J. Emneus, in Bioelectrochemistry: Fundamentals, Experimental Techniques and Applications (Ed. P.N.Bartlett), John Wiley and Sons, Chichester, England, 2008, pp. 377-410.

[19] A. Harper, M.R. Anderson, *Sensors* 2010, **10**, 8248.

[20] X. Chen, B. Su, X. Song, Q. Chen, X. Chen, X. Wang, *Trends Anal. Chem.* 2011, **30**, 665.

[21] P. R. Coulet, in Biosensor Principles and Applications (Ed. L.J. Blum and P.R. Coulet), Marcel Dekker, New York, 1991, pp. 1-45.

[22] D. W. Kimmel, G. LeBlanc, M.E. Meschievitz, D. E. Cliffel, *Anal. Chem.* 2012, **84**, 685.

[23] C. L. Morgan, D.J. Newman, C. P. Price, *Clin. Chem.* 1996, **42**, 193.

[24] O. A. Sadik, A.O. Aluoch, A. Zhou, *Biosens. Bioelectron.* 2009, **24**, 2749.

[25] M. Vestergaard, K. Kerman, E. Tamiya, *Sensors* 2007, **7**, 3442.

[26] N. B. Ramirez , A. M. Salgado, B. Valdman, *Braz. J. Chem. Eng.* 2009, **26**, 227.

[27] Z. Xu, X. Chen, S. Dong, *Trends Anal. Chem.* 2006, **25**, 899.

[28] F. R.R. Teles, L.P. Fonseca, *Mater. Sci. Eng. C* 2008, **28**, 1530.

[29] F. Ricci, G. Adornetto, G. Palleschi, *Electrochim. Acta* 2012, **84**, 74.

[30] J. C. Claussen, M.M. Wickner, T.S. Fisher, D.M. Porterfield, *Appl. Mater. Interfaces* 2011, **3**, 1765.

[31] P. Krzyczmonik, E. Socha, *CHEMIK* 2015, **69**, 11.

[32] S. M. Oja, M. Wood, B. Zhang, *Anal. Chem.* 2013, **85**, 473.

[33] C. R. Martin, D.T. Mitchell, in *Electroanalytical Chemistry: a Series of Advances*, edited by A.L. Bard, I. Rubinstein, Marcel Dekker Inc., New York vol.21**,** 1999, pp 1-74.

[34] S. Vaddiraju, I. Tomazos, D.J. Burgess, F.C. Jain, F. Papadimitrakopoulos, *Biosens. Bioelectron.* 2010, **25**, 1553.

[35] D. Grieshaber, R. MacKenzie, J. Voros, E. Reimhult, *Sensors* 2008, **8**, 1400.

[36] Y. Lu, M. Yang, F. Qu, G. Shen, R. Yu, *Bioelectrochemistry* 2007, **71**, 211.

[37] J. E. Koehne, H. Chen, A.M. Cassell, Q. Ye, J. Han, M. Meyyappan, J. Li, *Clin. Chem.* 2004, **50**, 1886.

[38] C. Zhu, G. Yang, H. Li, D. Du, Y. Lin, *Anal. Chem.* 2015, **87**, 230.

[39] J. Cabaj, J. Sołoducho, *Materials Sciences and Applications* 2014, **5**, 752.

[40] J. Wang, *Analyst* 2005, **130**, 421.

[41] M. P. Nagale, I. Fritsch. *Anal. Chem.* 1998, **70**, 2902.

[42] J. Hees, R. Hoffmann, A. Kriele, W. Smirnov, H. Obloh, K. Glorer, B. Raynor, R. Driad, N. Yang, O.A. Williams *et al*, *ACS Nano* 2011, **5**, 3339.

[43] S. E. Creager, P.T. Radford, *J. Electroanal. Chem.* 2001, **500**, 21.

[44] C. R. Martin, *Science* 1994, **266**, 1961.

[45] V. P. Menon, C. R. Martin, *Anal. Chem.* 1995, **67***,* 1920.

[46] C. R. Martin, *Chem. Mater.* 1996, **8***,* 1739.

[47] M. Ongaro, P. Ugo, *Anal. Bioanal. Chem.* 2013, **405**, 3715.

[48] C. G. Zoski, N. Yang, *Anal. Chem.* 2007, **79**, 1474.

[49] Y. H. Lanyon, G. De Marzi, Y.E. Watson, A.J. Quinn, J.P. Gleeson, G. Redmond, D.W. M. Arrigan, *Anal. Chem.* 2007, **79**, 3048.

[50] E. Ferain, R. Legras, *Nucl. Instrum. Methods B* 2003, **208**, 115.

[51] P. Ugo, N. Pepe, L.M. Moretto, M. Battagliarin, *J. Electroanal. Chem.* 2003, **560**,51.

[52] P. Ugo, L.M. Moretto, in C. Zoski (ed) *Handbook of Electrochemistry*, Amsterdam, Elsevier, 2007, p698.

[53] M. Henry, C. Dupont-Gillain, P. Bertrand, *Langmuir* 2003, **19***,* 6271.

[54] M. De Leo, F. C. Pereira, L. M. Moretto, P. Scopece, S. Polizzi, P. Ugo, *Chem. Mater.* 2007, **19***,* 5955.

[55] P. Ugo, L.M. Moretto, M. De Leo, A.P. Doherty, C. Vallese, S. Pentlavalli, *Electrochimica Acta* 2010, **55**, 2865.

[56] C. Amatore, J. M. Saveant, D. Tessier, *J. Electroanal. Chem.* 1983, **147**, 39.

[57] P. Tomcik, *Sensors* 2013, **13**, 13659.

[58] J. Orozco, C. Fernandez-Sanchez, C. Jimenez-Jorquera, *Sensors* 2010, **10**, 475.

[59] N. Godino, X. Borrise, F.X. Munoz, F.J. del Campo, R.G. Compton, *J. Phys. Chem. C* 2009**, 113***, 11119.

[60] L. Xiao, I. Streeter, G.G. Wildgoose, R.G. Compton, *Sensor. Actuator B* 2008, **133**, 118

[61] R. G. Compton, G.G. Wildgoose, N.V. Rees, I. Streeter, R. Baron, *Chem. Phys. Lett.* 2008, 459, 1.

[62] D. W.M. Arrigan, *Analyst* 2004, **129**, 1157.

[63] M. Wirtz, CR. Martin, *Adv. Matter.* 2003, **15**, 455.

[64] L. M. Moretto, N. Pepe, P. Ugo, *Talanta* 2004, **62**, 1055.

[65] B. Brunetti, P. Ugo, L.M. Moretto, C.R. Martin, *J. Electroanal. Chem.* 2000, **491**, 166.

[66] P. Ugo, L.M. Moretto, S. Bellomi, V.P. Menon, C.R. Martin, *Anal. Chem.* 1996, **68**, 4160.

[67] B. K. Jena, C.R. Raj, *Anal. Chem.* 2008, **80**, 4836.

[68] M. Pumera, S. Sanchez, I. Ichinose, J. Tang, *Sensor. Actuator. B* 2007, **123**, 1195.

[69] C. Jianrong, M. Yuqing, H. Nongyue, W. Xiaohua, L. Sijiao, *Biotechnol. Adv.* 2004, **22**, 505.

[70] J. J. Gooding, D.B. Hibbert, *TrAc. Trens. Anal. Chem.* 1999, **18**, 525.

[71] M. Silvestrini, K. Bortolozzo, D. Paladin, P. Ugo, *ECS Transactions* 2010, **25**, 1.

[72] S. Pozzi Mucelli, M. Zamuner, M. Tormen, G. Stanta, P. Ugo, *Biosens. Bioelectron.* 2008, **23**, 1900.

[73] M. Zamuner, S. Pozzi Mucelli, M. Tormen, G. Stanta, P. Ugo, *Eur. J. Nanomed.* 2008, **1***, 33.

[74] M. Silvestrini, L. Fruk, L.M. Moretto, P. Ugo, *J. Nanosci. Nanotechnol.* 2015, **15**, 3437.

[75] M. Silvestrini, L. Fruk, P. Ugo, *Biosens. Bioelectron.* 2013, **40**, 265.

[76] L. Hu, G. Xu, *Chem. Soc. Rev.* 2010, **39**, 3275.

[77] W. Miao. *Chem. Rev.* 2008, **108**, 2506.

[78] A. Zweig, A.K. Hoffmann, D.L. Maricle, A.H. Maurer, *J. Am. Chem. Soc.* 1968*, **90***, 261.

[79] A. J. Bard. *Electrogenerated Chemiluminescence*, 2004, Marcel Dekker Inc., New York, USA.

[80] A. W. Knight, *Trends Anal. Chem.* 1999, **18**, 47.

[81] B. Tamamushi, H. Akiyama, *Trans. Faraday Soc.* 1939, **35**, 491.

[82] D. M. Hercules, *Science* 1964, **145**, 808.

[83] K. D. Legg, D.M. Hercules, *J. Am. Chem. Soc.* 1969, **91**, 1902.

[84] R. Pyati, M.M. Richter, *Annu. Rep. Prog. Chem. Sect. C* 2007, **103**, 12.

[85] G. F. Blackburn, H.P. Shah, J.H. Kenten, J. Leland, R.A. Kamin, J. Link, J. Peterman, M.J. Powell, A. Shah, D.B. Talley *et al.*, *Clin. Chem.* 1991, **37**, 1534.

[86] N. E. Tokel, A.J. Bard, *J. Am. Chem. Soc.* 1972, **94**, 2862.

[87] J. Li, X. Jia, E. Wang, *Spectrosc. Prop. Inorg. Organomet. Compd.* 2013, **44**, 1.

[88] Z. Liu, W. Qi, G. Xu, *Chem. Soc. Rev.* 2015, **44**, 3117.

[89] M. M. Richter, *Chem. Rev.* 2004, **104**, 3003.

[90] H. Wei, E.Wang, *Luminescence* 2011, **26**, 77.

[91] M. M. Richter, A.J. Bard, *Anal. Chem.* 1996, **68**, 2641.

[92] S. Liu, X. Zhang, Y. Yu, G. Zou, *Anal. Chem.* 2014, **86**, 2784.

[93] S. K. Poznyak, D.V. Talapin, E.V. Shevchenko, H. Weller, *Nano Lett.* 2004, **4**, 693.

[94] K. Muzyka, *Biosens. Bioelectron.* 2014, **54**, 393.

[95] S. Deng, H. Ju, *Analyst* 2013, **138**, 43.

[96] I. Rubinstein, A.J. Bard, *J. Am. Chem. Soc.* 1981, **103**, 512.

[97] S. M. Park, A.J. Bard, *J. Am. Chem. Soc.* 1975, **97**, 2978.

[98] L. R. Faulkner, A.J. Bard, *J. Am. Chem. SOC.* **1968**, 90, 6284-6290.

[99] J. E. Dick, C. Renault, B.-K. Kim, A.J. Bard, *J. Am. Chem. Soc.* 2014, **136**, 13546.

[100] D. Ege, W.G. Becker, A.J. Bard. *Anal. Chem.* 1984, **56**, 2413.

[101] E. K. Walker, D.A.V. Bout, K.J. Stevenson, *J. Phys. Chem. C* 2011, **115**, 2470.

[102] C. S. Haslag, M.M. Richter, *J. Lumin.* 2012, **132**, 636.

[103] B. D. Muegge, S. Brooks, M. M. Richter, *Anal. Chem.* 2003, **75**, 1102.

[104] X. Lu, D. Liu, J. Du, H. Wang, Z. Xue, X. Liu, X. Zhou, *Analyst* 2012, **137**, 588.

[105] X. Liu, L. Shi, W. Niu, H. Li, G. Xu, *Angew. Chem. Int. Ed.* 2007, **46**, 421.

[106] W. Miao, J.-P. Choi, A.J. Bard, *J. Am. Chem. Soc.* 2002, **124**, 14478.

[107] Y. Zu, A.J. Bard, *Anal. Chem.* 2001, **73**, 3960.

[108] B. Sun, H. Qi, F. Ma, Q. Gao, C. Zhang, W. Miao, *Anal. Chem.* 2010, **82**, 5046.

[109] T. L. Pittman, W. Miao, *J. Phys. Chem. C* 2008, **112**, 16999.

[110] Z. Chen, Y. Zu, *J. Phys. Chem. C* 2009, **113**, 21877.

[111] M. Milutinovic, S. Sallard, D. Manojlovic, N. Mano, N. Sojic, *Bioelectrochem.* 2011, **82**, 63.

[112] M. Sentic, M. Milutinovic, F. Kanoufi, D. Manojlovic, S. Arbault, N. Sojic, *Chem. Sci.* 2014, **5**, 2568.

[113] M. J. Li, Z. Chen, V. W. W. Yam, Y. Zu, *ACS Nano* 2008, **2**, 905.

[114] F. Li, Y. Zu, *Anal. Chem.* 2004, **76**, 1768.

[115] Z. Xu, J. Yu, *Nanotechnology* 2010, **21**, 245501.

[116] Y. Gao, J. Li, X. Yang, Q. Xiang, K. Wang, *Electroanalysis* 2014, **26**, 382.

[117] F. Li, H. Cui, X.Q. Lin. *Luminescence* 2002, **17**, 117.

[118] G. J. Barbante, E.H. Doeven, E. Kerr, T.U. Connell, P.S. Donnelly, J.M. White, T. Lopes, S. Laird, D.J.D. Wilson, P.J. Barnard *et al*., *Chem. Eur. J.* 2014, **20**, 3322.

[119] F. Deiss, C.N. LaFratta, M. Symer, T.M. Blicharz, N. Sojic, D.R. Walt, *J. Am. Chem. Soc*. 2009, **131**, 6088.

[120] M. Staffilani, E. Hoss, U. Giesen, E. Schneider, F. Hartl, H.P. Josel, L. De Cola, *Inorg. Chem.* 2003, **42**, 7789.

[121] B. D. Stringer, L.M. Quan, P.J. Barnard, D.J. Wilson, C. F. Hogan, *Organometallics 2014,* **33**, 4860.

[122] E. H. Doeven, G.J. Barbante, E. Kerr, C.F. Hogan, J.A. Endler, P.S. Francis, *Anal. Chem.* 2014, **86**, 2727.

[123] E. H. Doeven, E.M. Zammit, G.J. Barbante, P.S. Francis, N.W. Barnett, C.F. Hogan, *Chem. Sci.* 2013, **4**, 977.

[124] E. H. Doeven, E.M. Zammit, G.J. Barbante, C.F. Hogan, N.W. Barnett, P.S. Francis, *Angew. Chem.* 2012, **124**, 4430.

[125] Y. P. Dong, Z. Ni, J. Zhang, B. Tong, X.F. Chu, *J. Lumin.* 2013, **136**, 165.

[126] A. Chovin, P. Garrigue, N. Sojic, *Bioelectrochem.* 2006, **69**, 25.

[127] M. Sentic, G. Loget, D. Manojlovic, A. Kuhn, N. Sojic, *Angew. Chem. Int. Ed.* 2012, **51**, 11284.

[128] J. L. Delaney, C.F. Hogan, J. Tian, W. Shen, *Anal. Chem.* 2011, **83**, 1300.

[129] B. V. Chikkaveeraiah, A.A. Bhirde, N.Y. Morgan, H.S. Eden, X. Chen, *ACS Nano* 2012, **6**, 6546.

[130] B. Zhang, K.L. Adams, S.J. Luber, D.J. Eves, M.L. Heien, A.G. Ewing. *Anal. Chem*. 2008, **80**, 1394.

[131] N. Gan, J. Zhou, P. Xiong, T. Li, S. Jiang, Y. Cao, Q. Jiang, *Int. J. Mol. Sci.* 2013, **14**, 10397.

[132] H. Qi, X. Qiu, D. Xie, C. Ling, Q. Gao, C. Xiao, *Anal. Chem.* 2013, **85**, 3886.

[133] L. Xu, Y. Li, S. Wu, X. Liu, B. Su, *Angew. Chem.* 2012, **124**, 8192.

[134] X. Bi, H. Ning, T. Wang, D. Li, Y. Liu, T. Yang, J. Yu, C. Tao, *PLOS One*, 2012, **7**, e48162.

[135] L. Indrawati, J.H. Heinrichs, E.P. Wen, J.M. Skinner, *World J. Vaccines* 2012, **2**, 27.

[136] W. Miao, A.J. Bard, *Anal. Chem.* 2004, **76**, 7109.

[137] F. Cataldo, G. Montalto. *World J. Gastroenterol.* 2007, **13**, 2153.

[138] S. Guandalini, A. Assiri, *JAMA Pediatr.* 2014, **168**, 272.

[139] J. F. Ludvigsson, D.A. Leffler, J.C. Bai, F. Biagi, A. Fasano, P.H.R. Green, M. Hadjivassiliou, K. Kaukinen, C.P. Kelly, J.N. Leonard *et al*., *Gut* 2013, **62**, 43.

[140] J. F. Ludvigsson, J.C. Bai, F. Biagi, T.R. Card, C. Ciacci, P.J. Ciclitira, P.H.R. Green, M. Hadjivassiliou, A. Holdoway, D.A. van Heel *et al*. *Gut* 2014, **0**, 1.

[141] M. N. Marsh, Gastroenterology 1992, **102**, 330.

[142] J. H. Van De Kamer, H.A. Weijers, W.K. Dicke, *Acta Paediatrica* 1953, **42**, 223.

[143] W. K. Dicke, H.A. Weijers, J.H. Van De Kamer, *Acta Paediatrica* 1953, **42**, 34.

[144] V. Abadie, L.M. Sollid, L.B. Barreiro, B. Jabri, *Annu. Rev. Immunol.* 2011, **29**, 493.

[145] W. Dieterich, T. Ehnis, M. Bauer, P. Donner, U. Volta, E.O. Riecken, D. Schuppan, *Nat. Med.* 1997, **3**, 797.

[146] F. Tucci, L. Astarita, A. Abkari, M. Abu-Zekry, T. Attard, M.B. Hariz, J.R. Bilbao, G. Boudraa, S. Boukthir, S. Costa *et al., BMC Gastroenterology* 2014, **14**, 24.

[147] N. Gujral, H.J. Freeman, A.B.R. Thomson, *World J. Gastrol.* 2012, **18**, 6036.

[148] P. H.R. Green, C. Cellier, *New Engl. J.Med.* 2007, **357**, 1731.

[149] D. H. Kaswala, G. Veeraraghavan, C.P. Kelly, D.A. Leffler, *Diseases* 2015, **3**, 86.

[150] J. C. Bai, M. Fried, G.R. Corazza, D. Schuppan, M. Farthing, C. Catassi, L. Greco, H. Cohen, C. Ciacci, R. Eliakim *et al.*, *Clin. Gastroenterol.* 2013, **47**, 121.

[151] N. E. Castillo, T.G. Theethira, D.A. Leffler, *Gastroenterology Report* 2014, 1.

[152] S. Lohi, K. Mustalahti, K. Kaukinen, K. Laurila, P. Collin, H. Rissanen, O. Lohi, E. Bravi, M. Gasparin, A. Reunanen *et al., Aliment. Pharmacol. Ther.* 2007, **26**, 1217.

[153] M. Giannetto, M. Mattarozzi, E. Umiltà, A. Manfredi, S. Quaglia, M. Careri, *Biosens. Bioelectron.* 2014, **62**, 325.

[154] T. D. Pelkowski, A.J. Viera, *Am. Fam. Physician* 2014, **89**, 99.

[155] D. Schuppan. *Gastroenterol.* 2000, **119**, 234.

[156] C. Ho-Yen, F. Chang, J. van der Walt, T. Mitchell, P. Ciclitira, *Histopathology* 2009, **54**, 783.

[157] B. G. Thewissen, I. Celus, K. Brijs, J.A. Delcour, *J. Agric. Food Chem.* 2011, **59**, 1370.

[158] A. Sapone, J.C. Bai, C. Ciacci, J. Dolinsek, P.H.R. Green, M. Hadjivassiliou, K. Kaukinen, K. Rostami, DS Sanders, M. Schumann *et al.*, *BMC Medicine* 2012, **10**, 13.

[159] F. Koning, L. Gilissen, C. Wijmenga. *Springer Semin. Immun.* 2005, **27**, 217.

[160] J. A. Murray, *Am. J. Clin. Nutr.* 1999, **69**, 354.

[161] O. Molberg, S.N. McAdam, L.M. Sollid, *J. Pediatr. Gastr. Nutr.* 1999, 30, 232.

[162] K. Mehta, A. Kumar, H. Kim, *Biochem. Pharmacol.* 2010, **80**, 1921.

[163] D. M. Pinkas, P. Strop, A.T. Brunger, C. Khosla, *PLoS Biol.* 2007, **5**, 2288.

[164] M. Lesort, J. Tucholski, M.L. Miller, G.V.W. Johnson, *Prog. Neurobiol.* 2000, **61**, 439.

[165] R. Casadio, E. Polverini, P. Mariani, F. Spinozzi, F. Carsughi, A. Fontana, P.P. de Laureto, G. Matteucci, C.M. Bergamini. *Eur. J. Biochem.* 1999, **262**, 672.

[166] T. H. Jang, D.S. Lee, K. Choi, E.M. Jeong, I.G. Kim, Y.W. Kim, J.N. Chun, J.H. Jeon, H.H. Park, *PLOS One* 2014, **9**, e107005.

[167] M. S. Pavlyukov, N.V. Antipova, M.V. Balashova, M.I. Shakhparonov, *Biochem. Bioph. Res. Co.* 2012, **421**, 773.

[168] M. Pietsch, R. Wodtke, J. Pietzsch, R. Löser, *Bioorg.Med. Chem. Lett.* 2013, **23**, 6528.

[169] J. Kaczkowski, *Pol. J. Food Nutr. Sci.* 2005, **14**, 3.

[170] L. Fesus, M. Piacentini, *Trends Biochem. Sci.* 2002, **27**, 534.

[171] A. Ichinose, R.E. Bottenus, E.W. Davie, *J. Biol. Chem.* 1990, **265**, 13411.

[172] T. Matthias, S. Pfeiffer, C. Selmi, M. E. Gershwin, *Clin. Rev. Allerg. Immunol*. 2010, **38**, 298.

[173] W. Dieterich, E. Laag, H. Schopper, U. Volta, A. Ferguson, H. Gillett, E.O. Riecken, D. Schuppan. *Gastroenterol.* 1998, **115**, 1317.

[174] J. Wolf, I. Lachmann, U. Wagner, A.A. Osman, T. Mothes, *Anal. Biochem.* 2011, **419**, 153.

[175] K. Kenrick, A.S. Day, *Aust. Fam. Physician* 2014, **43**, 674.

[176] D. Schuppan, Y. Junker, D. Barisani. *Gastroenterol.* 2009, **137**, 1912.

[177] J. S.K. Chen, K. Mehta, *Int. J. Biochem.Cell B.* 1999, **31**, 817.

[178] S. Reif, A. Lerner, *Autoimmun. Rev.* 2004, **3**, 40.

[179] K. A. Scherf, P. Koehler, H. Wieser, *Advances in Chemical Engineering and Science* 2015, **5**, 83.

[180] M. Bozzola, E. Bozzola, S. Pagani, A. Mascolo, R. Porto, C. Meazza, *Italian Journal of Pediatrics* 2014, **40**, 4.

[181] D. H. Dewar, P.J. Ciclitira, *Gastroenterol.* 2005, **128**, S19.

[182] A. Lerner, *International Journal of Celiac Disease* 2014, **2**, 64.

[183] J. Bai, E. Zeballos, M. Fried, G.R. Corazza, D. Schuppan, M.J.G. Farthing, C. Catassi, L. Greco, H. Cohen, J.H. Krabshuis, WGO 2007, **1**.

[184] A. C. Schyum, J.J. Rumessen, *U. E. G.* 2013, **1**, 319.

[185] A. Rostom, C. Dube, A. Cranney, N. Saloojee, R. Sy, C. Garritty, M. Sampson, L. Zhang, F. Yazdi, V. Mamaladze, I. Pan, J. Macneil, D. Mack, D. Patel, D. Moher, *Gastroenterology* 2005, **128**, S38.

[186] V. Baldas, A. Tommasini, C Trevisiol, I Berti, A Fasano, D Sblattero, A Bradbury, R Marzari, G Barillari, A Ventura, T Not, *Gut* 2000, **47,** 628–631.

[187] M. Ahmed, *JSM Gastroenterol. Hepatol.* 2014, **2**, 1017.

[188] A. Rubio-Tapia , I.D. Hill, C.P. Kelly, A.H. Calderwood, J. A. Murray, *Am. J. Gastroenterol.* 2013, 108,656.

[189] C. Catassi, A. Fasano, *Am. J.Med.* 2010, **123**, 691.

[190] E.Vecsei**,** S. Steinwendner**,** H. Kogler**,** A. Innerhofer**,** K. Hammer**,** O.A. Haas**,** G. Amann**,** A. Chott**,** H. Vogelsang**,** R. Schoenlechner**,** W. Huf**,** A. Vecsei, *BMC Gastroenterology* 2014, **14**,28.

[191] Celiac Disease Center, The University of Chicago, http://www.cureceliacdisease.org/wp-content/uploads/2011/09/CDCFactSheets5_Diagnosis.pdf

[192] M. J. Bruins, *Nutrients* 2013, **5**, 4614.

[193] S. Husby, S. Koletzko, I.R. Korponay-Szabo´, M.L. Mearin, A. Phillips, R. Shamir, R. Troncone, K. Giersiepen, D. Branski, C. Catassi *et al*., *JPGN* 2012, **54**, 136.

[194] F. Megiorni, A. Pizzuti. *J. Biomed. Sci.* 2012, **19**, 88.

[195] D. Schuppan, K.P. Zimmer, *Dtsch Arztebl Int.* 2013, **110**, 835.

[196] J. Crone, B. Rami, W.D. Huber, G. Granditsch, E. Schober, J. Pediatr. Gastroenterol. Nutr. 2003, **37**, 67.

[197] C. Cronin, F. Shanahan, *The Lancet* 1997, **349**, 1096.

[198] A. Akirov, O. Pinhas-Hamiel, *World J. Diabetes* 2015, **6**, 707.

[199] K. Larsson, A. Carlsson, E. Caderwall, B. Jonsson, J. Neiderud, A. Lernmark, S.A. Evarsson, *Pediatric Diabetes* 2008, **9**, 354.

Chapter 2

Miniaturized Enzymatic Biosensor *via* Biofunctionalization of the Insulator of Nanoelectrode Ensembles

2.1 Introduction

Research in the field of nanoelectrodes and electrochemical nanobiosensors is gaining impulse by recent developments in nanotechnology and nanoscience, which made nanoelectrodes and their arrays available for developing sensors tailored to specific analytical and diagnostic applications [1-4].

Arrays of nanoelectrodes offer significantly higher overall current signal (a function of the number of nanoelectrodes in the array) [5,6], avoiding the requirements of using picoammeters and faraday cage to measure the feeble current at a single nanoelectrode. Moreover, they open an important prospect for multiplex biosensors design. The ordered arrays can be prepared by complex microfabrication procedures such as ion-beam or electron beam lithography [7-9]. The template synthesis of randomly spaced arrays of nanoelectrodes, on the other hand, is a cheaper, simpler and more accessible alternate fabrication technique [10]. In this work, NEEs prepared by the later technique are used. A commercial PC filter membrane of 30 nm nominal pore diameter, 6 µm thickness, 47 mm overall membrane diameter as well as about 6×10^8 pores per cm^2 is used as template. This pore size is chosen due to better effectiveness of pores filling and heat sealing, as well as easier peeling of the Au layer during preparation of the NEEs [10].

As indicated in the previous chapter, the geometric area of the NEEs is controlled by the hole size punctured on the strapping monokote cover. By reducing the hole size, the NEEs can be miniaturized to the sub-millimeter diameter range with negligible border effects [11] since a NEE with A_{geom} as small as 0.001 cm^2 still contains at least 10^5 nanoelectrodes. Previously, NEEs of geometric area as small as 0.008 cm^2 have been fabricated by our group [11]. Miniaturization of the geometric area of NEEs reduces the active electrode area proportionally. This in turn lower the biorecognition element loading capability on the active area of the electrode, e.g. *via* bridging by self-assembled monolayer of thiols [12]. Low biomolecule loading capability is one of the major limitations in transforming nanostructured electrodes into

viable electrochemical biosensors. In fact, biomolecule loading capability can be boosted by increasing the exposed metallic electrode area by etching the polymer template [13,14]. But, this causes an increase of the double-layer charging current, affecting negatively the signal-to-background current ratio [15].

The new approach of biorecognition agent immobilization exclusively on the PC surface surrounding the nanodisk electrodes [16,17] seems particularly attractive for preparing miniaturized enzymatic biosensors since the PC area available for the functionalization is more than 100 times larger than the metallic active area of the NEE. In such a design, the transducer and biorecognition layer are integrated in strict proximity but not overlapped. Moreover, since no increase in A_{act} is required, voltammetric signals are generated at the highest signal-to-background current ratio. So far, this approach has been successfully used for developing novel affinity biosensors [18,19], but has not been reported for electrocatalytic sensors in which the analyte is the enzyme substrate. In order to test the feasibility of such an approach, we choose the preparation of a micro-NEE glucose sensor as a case study. Developing a glucose biosensor is chosen because of two main reasons: firstly, glucose oxidase is well studied with many beneficial properties and hence is an excellent model enzyme to study newly developed method, and secondly, up to 11 % of IDDM patients develop CD so that a patient clinically identified to have one of the disorders is advisable to be diagnosed for the other. Therefore, it is quite interesting to develop a full package of biosensors (for both disorders) manufactured in the same way and that operate by the same principle.

Scheme 2.1 shows a simplified drawing illustrating the sensor's architecture and functioning principle. Briefly, GOx is immobilized on the PC membrane of the NEE, by exploiting the interaction between the PC surface [18,19] and the enzyme. Recent studies based on fourier transform infrared (FT-IR), time of flight secondary ion mass spectrometry (TOF-SIMS), atomic force microscopy (AFM), electrical and electrochemical measurements demonstrated that proteins bind efficiently onto the PC of track-etched membranes [20-22]. In particular, Silvestrini *et al* [20] showed that the PC of NEEs keeps the same high protein binding properties typical of virgin PC [21,22].

Concerning the biosensor proposed here, sketched in Scheme 2.1, the presence of glucose in the electrolyte solution, initiates an electrocatalytic cycle involving the enzyme glucose oxidase

immobilized on the PC of the NEE, glucose in the sample solution and the redox mediator (Ferrocenylmethyl)trimethylammonium (FA^+), which shuttles electrons between the GOx redox site and the nanoelectrodes. It is worth stressing that, notwithstanding the wide number of reports devoted to the development of electrochemical glucose biosensors [23-26], relatively few studies dealt with the use of arrays of nanoelectrodes to this aim [15,27,28] and no one dealt with miniaturized arrays. Note also that in all the above studies, the biorecognition layer is bound onto the metal surface of the nanoelectrodes and not on the insulator between them, as done here.
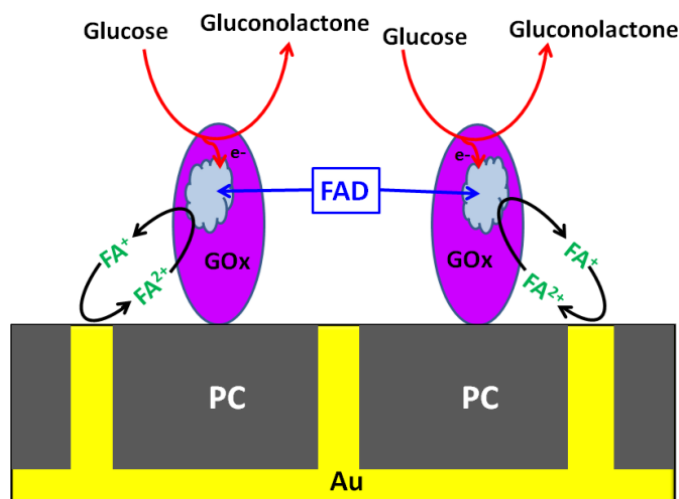
Scheme 2. 1 Schematic of the lateral section of the NEE based glucose biosensor. Note that the different elements are not drawn to scale.

2.2 Experimental

2.2.1 Instrumentation and materials

Cyclic voltammetric (CV) measurements were carried out at room temperature (21 ± 1 ^{o}C) with a CHI 620A potentiostat, using a three electrode cell equipped with a Pt spiral counter electrode, an Ag/AgCl (in KCl-saturated) reference electrode and the NEE as working electrode. CHI software was used to perform the digital simulations of the CVs.

Scanning electron microscope (SEM) and energy dispersive X-ray spectroscopy (EDS) analysis were performed using a TM3000 Hitachi table top scanning electron microscope coupled with a Swift ED3000 X-ray microanalysis system.

Track-etched polycarbonate membrane (47 mm diameter, 6 μm thickness, 6×10^8 pores per cm^2, 30 nm nominal pore diameter and average center-to-center pore distance 200 nm) were purchased from SPI-pore. Commercial gold electroless plating solution (Oromerse Part B, Technic Inc.) was used for synthesizing nanodisks. GOx from *Aspergillus niger,* bovine serum albumin (BSA), and Tween 20 surfactant were from Sigma-Aldrich. $FA^+PF_6^-$ was prepared by metathesis of the (ferrocenylmethyl)trimethylammonium iodide with potassium hexafluorophosphate (Alfa Aesar). All other reagents were of analytical grade and were used as received.

2.2.2 Preparation of NEEs

Electroless deposition of gold into nanoporous PC membrane and the subsequent fabrication of NEEs were carried out as described previously [10,29,30,31]. Briefly: after wetting the 6 μm thick, 47 mm diameter circular PC membrane for 2 h in methanol, the membrane was sensitized with $SnCl_2$ by immersion into a solution of 0.026 M $SnCl_2$ and 0.07 M trifluoroacetic acid in a mixture of methanol-water (50:50 vol/vol) for 5 minutes. After rinsing with three aliquots of methanol for 5 min, the sensitized membrane was immersed in 0.029 M $Ag[(NH_3)_2]NO_3$ for 10 min. The membrane was then kept in the Au plating bath (diluted Oromerse, part B, see above) which was 7.9 x 10^{-3} M in $Na_3Au(SO_3)_2$, 0.127 M in Na_2SO_3. After 30 minutes, 0.625 M formaldehyde was added to the plating bath; the delay time was introduced to allow the formation of the first gold nuclei (produced by galvanic displacement of metallic Ag^0 particles with Au^0 nuclei) in the pores of the PC before further catalytic growth of gold induced by adding formaldehyde. The temperature of the bath was maintained between 0 and 2 °C. The electroless deposition was allowed to proceed for 15 hours, and followed by addition of 0.3 M formaldehyde. The deposition was continued for another 9 hours, after which the membrane was taken off the bath and consecutively rinsed with water, immersed in 10% HNO_3 for 12 hours and rinsed with water again. The membrane bearing the deposited gold was gently dried with clean air before cutting into small pieces. The final assembly of the NEEs (for obtaining electrodes handy for use in an electrochemical cell) was carried out as detailed in Chapter 1. Before use, NEEs were treated in an oven for 30 min at 150 °C (slightly above the glass transition temperature of PC) to improve the sealing between PC and the Au nanowires. The geometric area, A_{geom}, of the NEE was determined by the diameter of a hole punched in the insulating film (Monokote by Topflite) that covers the peeled face of the NEEs. The electrical contact was

established with a copper tape attached to the NEE before placing the insulating tape. In this experiment, NEEs with two different hole dimensions were prepared: hole diameter 3 mm, to obtain NEEs with a $A_{geom}= 0.07$ cm^2 and NEEs with hole diameter of 800 µm, to obtain $A_{geom} = 0.005$ cm^2. For the smaller NEE the hole was made with a glowed needle and the effective dimension of the hole was checked by SEM measurements.

From each membrane, 50 to 60 electrodes were prepared. The NEEs with excellent electrochemical and morphological properties were isolated before functionalizing with biomolecules. Previously established parameters [31], based on extent of agreement between experimental and digital simulation CV parameters (see below), were applied. In average, about 60% of the NEEs were found to be fit for the biosensor development.

2.2.3 Enzyme immobilization

Glucose oxidase functionalized NEEs (GOx-NEEs) were prepared by incubating the NEEs with 20 µL of 1 µg µL^{-1} GOx in 0.1 M acetate or phosphate buffer (depending on the pH required) plus 0.2 M KCl, for 0.5, 1, 2, 4 or 12 h at room temperature. After thoroughly washing with Mill-Q water, CVs were recorded in 0.05 M phosphate buffer (pH 6.8) solution containing 100 µM $FA^+PF_6^-$, in the presence and absence of glucose.

2.3 Results and discussion

2.3.1 Characterization of the NEE

In this work, two groups of NEEs are employed. In both cases the density and diameter of the Au nanoelectrodes are identical. However, the overall electrode surface area or the geometric area which is composed of the Au nanodisks and the PC is different, causing a proportional difference in the number and area of Au nanodisks. The first group of NEEs (hereafter called macro-NEEs) are 3 mm overall diameter (geometric area (A_{geom}) $= 0.07$ cm^2) and contains Au nanodisks sharing an area of about 8.2×10^{-4} cm^2. The second group (hereafter called Micro-NEEs) is 800 µm in overall diameter ($A_{geom.} = 0.005$ cm^2) and the Au nanodisks share about 5.9×10^{-5} cm^2 of the geometric area.

Once the NEEs are prepared as described above, the electrochemical performance of each NEE was evaluated by recording CVs in a solution of $FA^+PF_6^-$ and the reversibility of the resulting CVs is tested by the reversibility parameters (peaks separation, current ratio, half peak potentials) and compared with digital simulations (Figure 2.1 and 2.2). Moreover, morphological and chemical make-up studies of the electrodes' surface are performed using EDS equipped SEM in order to distinguish best NEEs for biofunctionalization (Figure 2.3).

Figure 2.1 Shows CVs of typical 3 mm and 0.8 mm diameter NEEs at different scan rates in a solution of 0.05 M PBS pH 6.8 containing 100 µM $FA^+PF_6^-$ as a well known reversible redox probe. Reduction of the geometric area of the NEEs from 0.07 cm^2 to 0.005 cm^2 resulted in a reduction of anodic peak current by a factor of 14. However, the miniaturized NEE still produced peak shaped voltammogram down to reasonably low scan rates indicating that border effect is negligible.

For all NEEs used for developing the biosensors the reversibility parameters are in the acceptable range, i.e. linear I_p *vs* $v^{1/2}$ plot, I_{pa}/I_{pc} ratio of about 1, ΔE of 60 to 75 mV, and $E_{1/2}$ of around 0.420 (at scan rate of 50 mV s^{-1}).
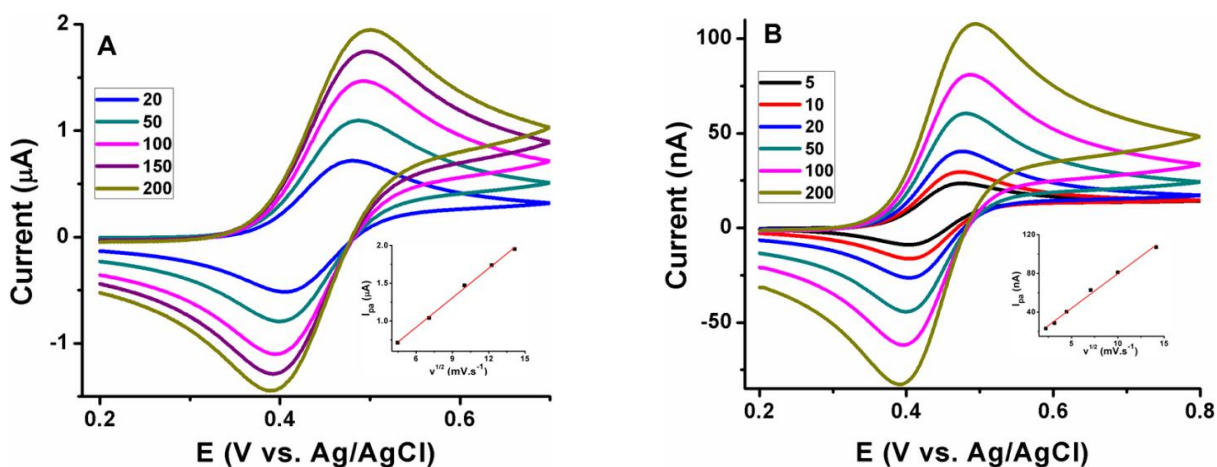

Figure 2.1 Cyclic voltammograms at different scan rates (mV) in 0.05 M phosphate buffer pH 6.8 containing 100 µM $FA^+PF_6^-$, **A**) NEE of A_{geom}=0.07 cm^2, **B**) NEE of A_{geom} = 0.005 cm^2. *Insets*: Plots of the dependence of faradaic peak current on square root of scan rate ($v^{1/2}$).

Figure 2.2 shows the comparison of the CVs of experimental (solid lines) and digital simulations (dashed lines) of the macro-NEEs (Figure 2.2A) and the micro-NEEs (Figure 2.2B) in 100 µM

$FA^+PF_6^-$ solution. In both cases, the observed electrochemical behaviors agree with the occurrence of one-electron reversible oxidation of the Fe(II) of the bis-cyclopentadienyl complex to Fe(III) [10, 29].

$$FA^+$$
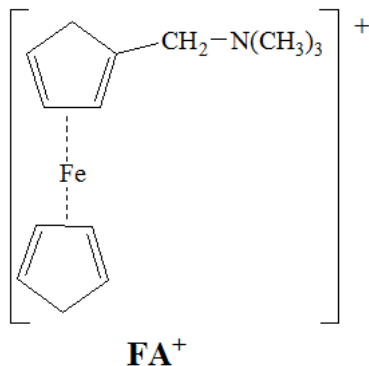
The digital simulations were performed using the following parameters and the CHI 660B software: $E° = 0.44$ V, $k° = 0.008$ and $D = 4 \times 10^{-6}$ cm^2 s^{-1} [33], where $E°$ is the formal potential, $k°$ is the heterogeneous electron transfer rate constant and D is the diffusion coefficient. Note that $k°$ is really the apparent rate constant ($k°_{app}$); as originally demonstrated by Menon and Martin [10], NEEs behave as electrodes with partially blocked surface (PBEs) [34]. Voltammetric currents at PBEs are indeed the same as those at bare electrodes of equivalent overall geometric area, but with a smaller apparent standard rate constant which depends on the fraction of blocked surface [34]. It was demonstrated [10,33,35] that for NEEs:

$$k°_{app} = k_{sh}° \times f \qquad\qquad (1)$$

where $k_{sh}°$ is the "true" heterogeneous rate transfer constant and f is the fractional area, $f = A_{act}/A_{geom}$. For the FA$^+$ case, $k° = 0.56$ [33], with $f = 1.2 \times 10^{-2}$.

The satisfactory fitting between experimental and simulated curves, together with the linear dependence of the anodic peak current with the square root of the scan rate (shown in Figure 2.1) indicates that the process is diffusion controlled and that both NEEs operate under total overlap diffusion conditions. Even if the oxidation peak current in Figure 2.2B is 14 times smaller than in Figure 2.2A, the faradaic-to-background current ratio is practically the same in both voltammetric patterns. This confirms that, even if the overall geometric radius of the micro-NEEs is quite small (r = 400 µm) in comparison to the macro-NEE, the critical dimension

governing the electrochemical behavior of the NEE is still larger than the thickness of the diffusion layer [8,9].
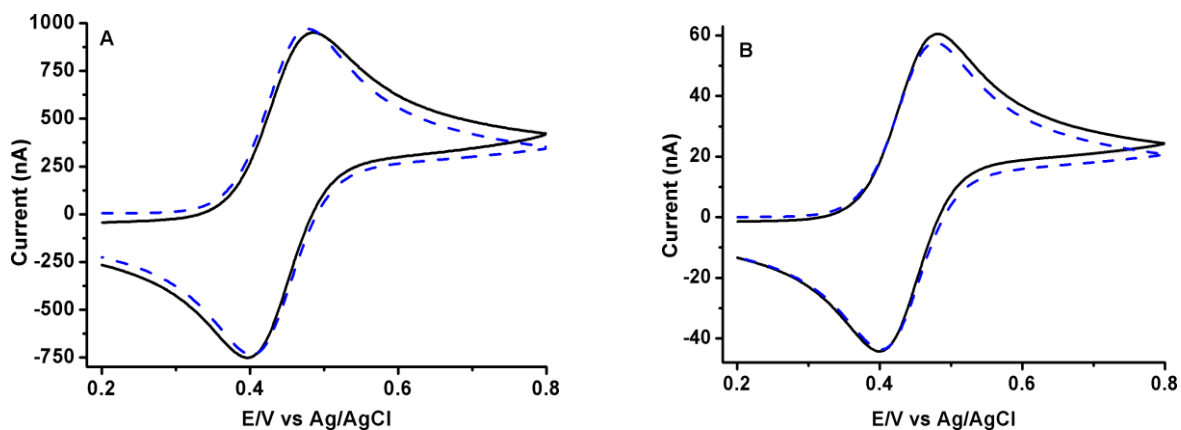

Figure 2.2 Experimental (solid lines) and simulated (dashed lines) CVs at a NEE recorded in 100 µM $FA^+PF_6^-$, 0.05 M phosphate buffer, pH 6.8 at 50 mV s^{-1}, **A**) $A_{geom.}= 0.07$ cm^2; $A_{act.}= 8.2 \times 10^{-4}$ cm^2; **B**) $A_{geom.} = 0.005$ cm^2, $A_{act.} = 5.9 \times 10^{-5}$ cm^2.

The SEM image reported in Figure 2.3 displays the surface of the NEE where the randomly scattered white spots are the surfaces of the metallic nanodisks emerging from the dark polycarbonate template. The fading lines behind the nanodisks are the traces of the nanofibers grown inside the PC membrane. The traces are visible due to the partial transparency of the polycarbonate template under the electron beam [30]. Also, the image clearly shows that all the nanofibers are not aligned parallel because of the angles of the original trajectories of the pores of the membrane developed during industrial tracking process.

Although, the average nominal diameter of the pores of the membrane used for preparation of the NEEs is reported as 30 nm by the manufacturer, the average diameter of the Au nanodisks of the NEEs was estimated by the SEM to be 50 ± 10 nm. Since the nanoelectrodes' density in the NEEs is about 6×10^8 per cm^2, the small micro-NEE ($A_{geom} = 0.005$ cm^2) still contains about 3 million nanoelectrodes. Based on the density and diameter of the nanodisks as well as the geometric area of the NEEs, the total active areas of the macro- and micro-NEEs are calculated to be 8.2×10^{-4} and 5.9×10^{-5} cm^2, respectively. Elemental analysis of the surface of a representative NEE using SEM-EDS produced the spectrum shown in Figure 2.3B. The Au peak is characteristic of the Au nanolectrodes and the well-defined peaks of C and O originated from the polycarbonate membrane. Moreover, the relative proportion of each element on the surface

of the NEE was automatically generated by the instrument and in this particular case the composition of the Au is found to be about 18 %.
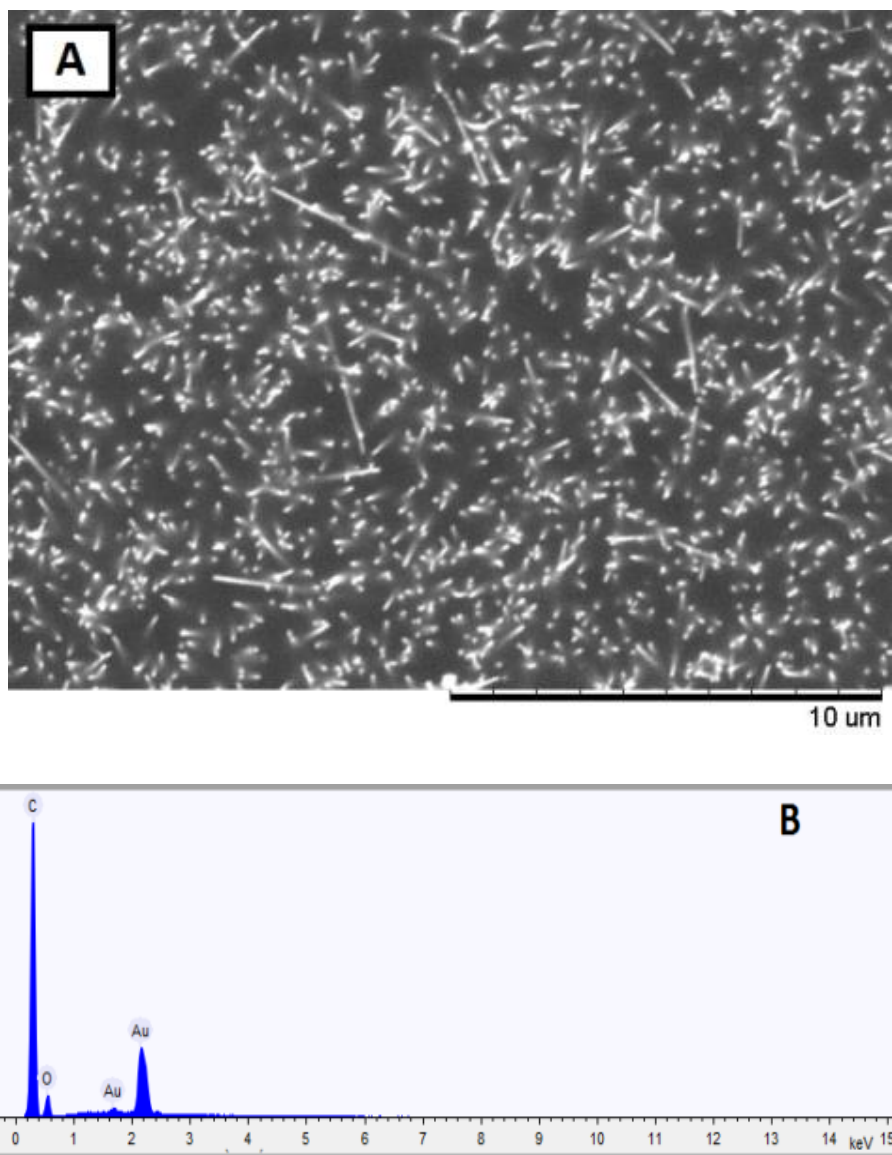

Figure 2.3 A) SEM image and **B**) SEM-EDS spectrum of the NEE used for developing the biosensor. SEM-EDS spectrum was taken from a portion of the NEE surface composed by the nanodisk electrodes and the black insulating surface surrounding them.

Previous AFM studies [20] demonstrated that the surface roughness of the PC membrane is quite high, i.e. about 50 nm which is comparable to the diameter of the nanodisks used in this experiment. This hampers the use of scanning tip microscopies to obtain more information about the nanodisks before and after biofunctionalization of the PC of the NEEs.

2.3.2 Modification of the NEEs

At variance with traditional mode of immobilization of GOx directly onto the active surface of the electrode [17,23,24,27,28,36,37], in this work, we propose a new biosensor platform where the GOx is selectively immobilized on the insulating polymer surrounding the metallic electrodes, as described in Scheme 2.1, using the procedure whose optimization is presented in the next section.

A well reversible CV pattern typical of a reversible one-electron oxidation of FA^+ is observed at the functionalized NEE in the absence of glucose, with $E_{1/2}$ of 0.432 V and anodic peak currents linearly related with the square root of the corresponding scan rates. The fact that the FA^+ response in the absence of glucose is practically unchanged from that recorded with a bare NEE confirms that the GOx is bound mainly onto the PC of the NEE, keeping almost unaltered the electron transfer kinetics at the Au nanoelectrodes. Also, it confirms that the presence of the biomolecule on the PC surface adjacent to the nanodisks, does not cause significant change in the cyclic voltammetric responses of NEEs. As can be evidenced from Figure 2.4, only slight increase (*ca.* 10 mV) in anodic and cathodic peak potential separation (ΔE_p) and an anodic peak current decrease of only 7 % resulted after the functionalization of the NEE with GOx.
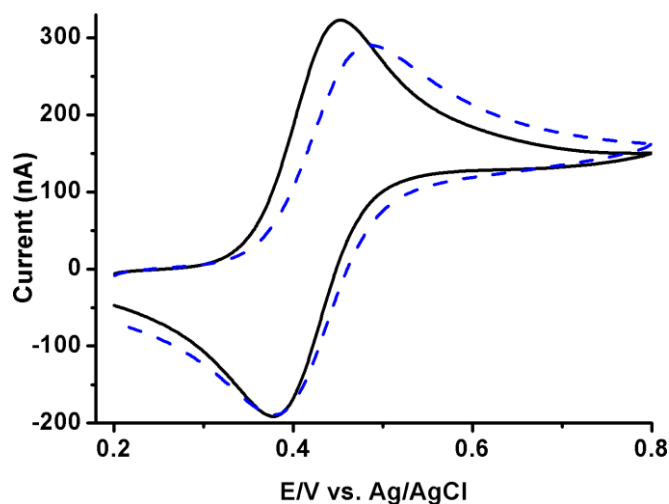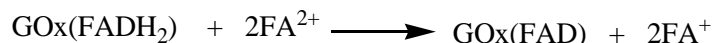

Figure 2.4 CVs recorded at a 3 mm NEE before (solid line) and after (dash line) functionalization with GOx in 100 μM $FA^+PF_6^-$, 0.05 M phosphate buffer, pH 6.8 at 5 mV s^{-1}.

Figure 2.5A on the other hand, shows the cyclic voltammograms recorded at 5 mV s^{-1} at a the functionalized macro-NEE (A_{geom} = 0.07 cm^2) functionalized with GOx in 0.05 M phosphate buffer solution pH 6.8 containing 100 μM FA$^+$PF$_6$, both in the absence (full line) and presence (dash line) of 50 mM glucose. It is quite clear that after addition of glucose into the electrolyte solution containing the redox mediator, the cyclic voltammetric pattern at the functionalized NEE is dramatically changed (see dashed line in Figure 2.5A) in such a way that the anodic peak current abruptly increased establishing a steady state, while the reverse cathodic peak is completely disappeared giving a typical electrocatalytic sigmoidally shaped CV pattern. This agrees with the following electrocatalytic cycle [38-41]:

$$FA^+ \rightleftharpoons FA^{2+} + e^-$$

$$GOx(FAD) + D\text{-Glucose} \longrightarrow GOx(FADH_2) + D\text{-Glucono-1,5-lactone}$$

$$GOx(FADH_2) + 2FA^{2+} \longrightarrow GOx(FAD) + 2FA^+$$

where, GOx (FADH$_2$) and GOx (FAD) represent reduced and oxidized forms of glucose oxidase, while FA$^+$ and FA^{2+} are the reduced and oxidized forms of the mediator.
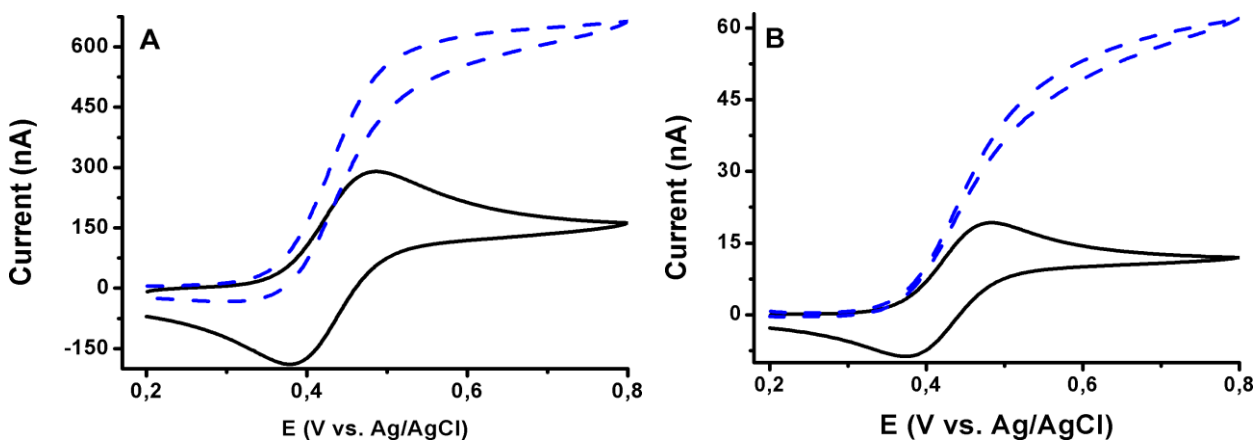

Figure 2.5 CVs recorded at GOx-NEEs in 100 μM FA$^+$PF$_6^-$, 0.05 M phosphate buffer (pH 6.8), in the absence (solid lines) and presence of 50 mM glucose (dashed lines) at 5 mV s^{-1}; **A**) A_{geom}= 0.07 cm^2, **B**) A_{geom}= 0.005 cm^2.

The well-defined sigmoidally shaped catalytic wave is developed as a consequence of GOx catalyzed oxidation of glucose followed by chemical reduction of two molecules of the

electrochemically oxidized form of the mediator per each molecule of the reduced form of the enzyme. All the above results indicate that analytically sufficient GOx enzyme is efficiently immobilized on the polymeric part of the NEE, without affecting its enzymatic activity.

Similarly, Figure 2.5B reports the results of the same experiment performed, however, with a functionalized micro-NEE characterized by a much smaller geometric area, that is 0.005 cm^2 (*vs* 0.07 cm^2 for the NEE in Figure 2.5A). The CV of FA$^+$ recorded in the absence of glucose is peak shaped and reversible, as expected for an array with overall critical dimension higher than the thickness of the diffusion layer (with 400 μm overall radius of the ensemble *vs* diffusion layer thickness of approximately 25 μm). Interestingly, the anodic peak current of FA$^+$ at the macro-NEE (Figure 2.5A) is about 15 times greater than the one recorded at the micro-NEE (Figure 2.5B), is in agreement with the geometric area ratio of the two electrodes which is about 14. However, the ratio of the experimentally measured steady state catalytic currents at the sensor of bigger electrode size to that of smaller electrode size, in the presence of glucose, gave a value close to 10. The fact that this value is less than the peak current ration of the two sensors recorded in the absence of glucose, proofs that the miniaturized biosensor is catalytically more efficient than the conventional NEE. Also, the experimentally derived ratios of catalytic currents of the sensors in the presence of glucose (I_{cat}) to the one in the absence of glucose (I_p) at scan rate of 5 mV s^{-1} was 3.7 for Figure 2.5A (macro-NEE), and 4.6 for Figure 2.5B (micro-NEE). These values are in agreement with previously reported values and can be taken as measures of catalytic efficiency of the modified electrode [42].

2.3.3 Optimization of analytical parameters

Since GOx is stable in wide pH range [41], the influence of the incubation pH during its immobilization step was studied by monitoring the resulting catalytic performance of the enzyme as evidenced by the electrochemical responses. The enzyme immobilization efficiency and its electrocatalytic performance at pH 4.2 and pH 5.6 acetate buffer, as well as in 0.05 M PBS pH 6.8 were investigated. Excellent immobilization, as determined by the resulting CVs in the presence of the substrate, was observed when the NEE was incubated with a GOx solution of pH 4.2. In addition to the immobilization pH, the influence of the pH of the electrolyte solution during the electrochemical measurements is studied at pH 5.6 and 6.8. The obtained results are listed in Table 1, where I_{cat} and I_p are the currents recorded at potential of 0.7 V in the presence

and absence of 50 mM glucose, respectively. According to these data, the maximum values for the $I_{Net} = (I_{cat} - I_p)$ and I_{cat}/I_p parameters are obtained when the incubation is done at pH 4.2 while the signal measurements are performed at pH 6.8.

Table 1 Effect of the pH of both the incubation solution and the CV supporting electrolyte, on the electrochemical response of the biosensor. Acetate buffer was used for solutions of pH 4.2 and 5.6, but phosphate buffer for pH 6.8.

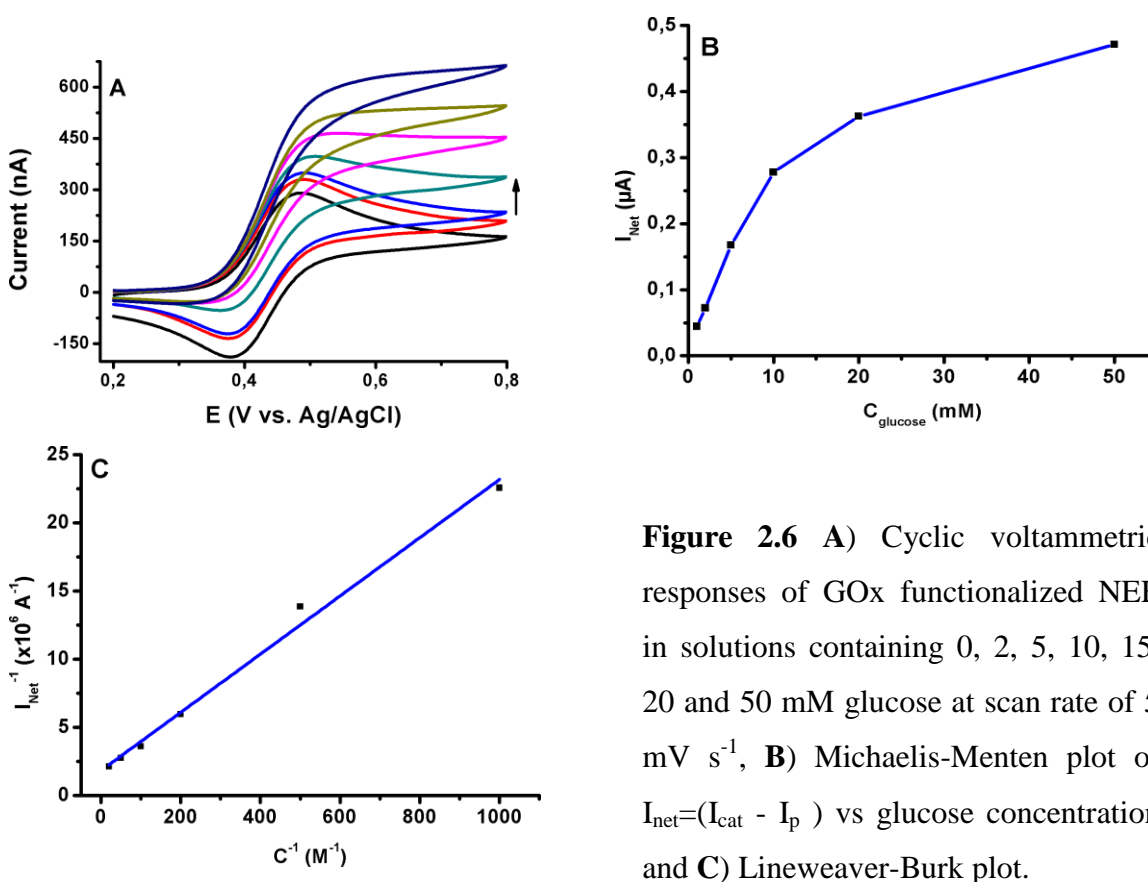| GOx Immobilization pH	Electrolyte pH	$I_{Net} = (I_{cat}-I_p)$ (µA)	I_{cat}/I_p
6.8	6.8	0.1870	1.1
5.6	5.6	0.0906	1.2
5.6	6.8	0.4273	2.2
4.2	6.8	0.4710	3.7

The closeness of the values of the optimal incubation pH and the enzymes' isoelectric point [43] suggests the involvement of both hydrophobic/hydrophilic and ionic interactions in the immobilization process. However, the absence of significant level of enzyme desorption from the surface the electrode on increasing the pH to 6.8 for the electrochemical measurements, gives a clue on the possible involvement of other forms of interactions to the immobilization. Due to the reason that very small amount of enzyme immobilized (but quite sufficient for electrocatalysis) and the presence of interfering functional groups in the protein (e.g. peptide bonds), it is difficult to obtain experimental data suitable to unambiguously determine the nature of the binding interaction between GOx and PC, for instance using FT-IR or attenuated total reflectance spectroscopy.

The effect of the length of the incubation time with GOx solution on the catalytic activity of the enzyme, was investigated by incubating the NEEs for different time interval (1, 2, 4 or 12 h) keeping other experimental conditions the same. The experimental results show that best performances are observed for NEEs incubated for 4 h or overnight (12 h).

2.3.4 Kinetic and analytical parameters

The effect of the concentration of the substrate on the voltammetric catalytic current of the biosensor is reported in Figure 2.6A. Relevant current increments, calculated as $I_{net} = (I_{cat} - I_p)$ are reported in Figure 2.6B as a function of glucose concentration. The plot evidences that the

biosensor follows Michaelis-Menten enzyme kinetics where the enzyme catalyzed current progressively increases with the concentration of the substrate until a saturation point above which the curve assumes an asymptomatic profile. The double reciprocal Lineweaver-Burk plot reported in Figure 2.6C shows the characteristics expected for Michaelis–Menten kinetics. From this plot, an apparent Michaelis–Menten constant (K_m^{app}) value of 12 mM is calculated. This value is in the range of the smallest values reported in the literature, [44-46] indicating that the GOx immobilized on the PC of the NEE is characterized by a high enzymatic activity. From the slope (m) of the linear calibration (Lineweaver-Burk plot) plot in the concentration range $2 – 50$ mM and from the blank standard deviation (σ_b) calculated as the standard deviation of 6 independent FA$^+$ peak current measurements with no glucose added, a detection limit of 36 µM is estimated ($3\sigma_b$/m criterion). Because the normal blood glucose level is from 4.4 to 6.6 mM [24], the linear range of our sensor is suitable for diagnostic purposes without the requirement of sample preconcentration.

Figure 2.6 A) Cyclic voltammetric responses of GOx functionalized NEE in solutions containing 0, 2, 5, 10, 15, 20 and 50 mM glucose at scan rate of 5 mV s^{-1}, **B**) Michaelis-Menten plot of $I_{net}=(I_{cat} - I_p)$ vs glucose concentration and **C**) Lineweaver-Burk plot.

2.3.5 Stability of the biosensor and effect of scan rate on the catalytic current

To evaluate the change in enzyme activity and intactness of the immobilized enzyme layer against repetitive exposure to electric field, multiple CVs are recorded consecutively at a single micro-NEE biosensor in the presence of 50 mM glucose. As reported in Figure 2.8 no significant reduction in catalytic current is observed indicating absence of significant loss of activity or leaching of immobilized enzyme for at least up to 25 repeated measurements.
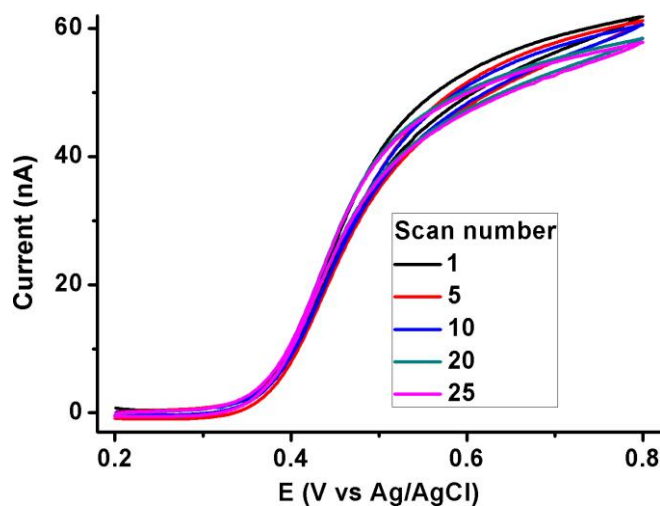

Figure 2.7 Representative CVs recorded when performing repeated scan cycles with the micro-NEE biosensor in 50 mM glucose. Other parameters are as indicated in Figure 2.5.

Short time stability assessment was carried out by measuring the electrocatalytic current stability for 3 consecutive days by storing the sensor at +4 ^{o}C when it is not in use. The electrocatalytic response at the micro-NEE biosensor did not show any noticeable reduction.

The effect of duration of the electrochemical experiment, governed by the scan rate, was studied against the resulting steady state electrocatalytic current of the biosensor. At reasonably slow scan rates (5 – 50 mV s^{-1}) the electrocatalytic current is almost the same indicating that the experimental time scale is long enough for the enzyme-substrate reaction to take place (Figure 2.7).
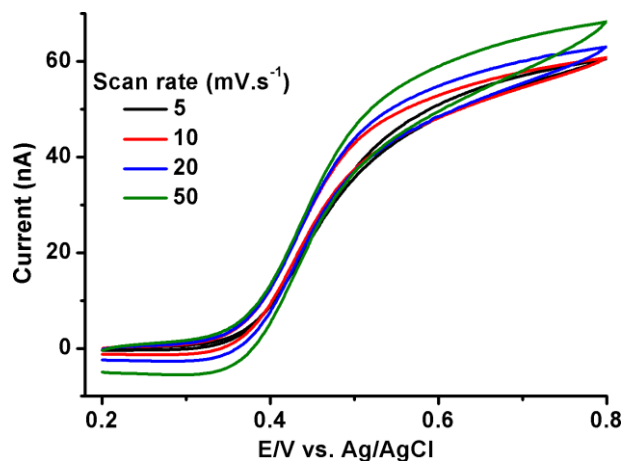
Figure 2.8 Cyclic voltammograms at a micro-NEE sensor at different scan rates. All experimental conditions are as in figure 2.5.

2.3.6 Samples analysis

A preliminary evaluation of the performance of the proposed sensor towards real samples was carried out on four Red Bull energy drinks. No significant catalytic current was observed for the sugar free labeled product (RB0), whereas significant catalytic currents were recorded from the three sugar containing products (RB1, RB2, RB3).
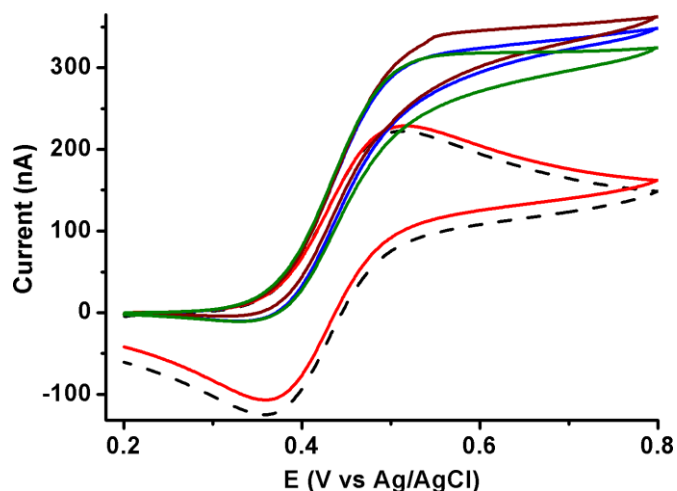

Figure 2.8 Glucose sensor in PBS (pH 6.8) containing 100µM FA$^+$ (dash line) and after addition of RB0 (red), RB1 (green), RB2 (blue) or RB3 (brown) at scan rate of 5 mV s^{-1}.

These results are encouraging for further evaluation of the sensor in the determination of glucose in more complex clinical serum samples.

2.4 Conclusion

The present study demonstrated that the relatively large surface of the PC of templated NEEs can be exploited to efficiently immobilize an enzymatic biorecognition layer in order to develop sensitive miniaturized biosensor, with critical dimension in the hundreds of micrometer range, while keeping excellent CV signals and detection capabilities. The development of a NEE-based glucose micro-sensor is taken as a case study to demonstrate the general applicability of the concept. The key point is the possibility of immobilization of the enzyme on the nonconductive PC of the templating membrane rather than functionalizing the metallic surface of the nanoelectrodes, as commonly reported in the literature. In the new approach, the biorecognition layer (on the polycarbonate) and the transducer (i.e. the nanoelectrodes) are integrated and kept in close proximity, but not overlapped. This approach allows immobilization of larger amount of enzyme than immobilizing only on the metallic part of a NEE with the same geometric area, and the immobilization is simplified to a single step. Moreover, since the enzyme is deposited on an organic polymer (PC), the biorecognition layer is in a more "natural" environment, being less exposed to electrical and electrochemical stress. The results obtained here demonstrate that the very high density of nanoelectrodes in the NEE (in excess to 10^8 nanoelectrodes per cm^2) allows the overall miniaturization of the biosensor down to sub-mm dimensions, without losing the analytical advantages of NEEs, namely highly improved signal to noise ratio and enhanced diffusion. The present results open the way to interesting applicative prospects for improving glucose detection with miniaturized biosensors for biomedical, environmental and food control purposes.

References

[1] M. Ongaro, P. Ugo, *Anal. Bioanal. Chem.* 2013, **405**, 3715.
[2] J. Li, J.E. Koehne, A.M. Cassell, H. Chen, H. Tee Ng, Q. Ye, W. Fan, J. Han, M. Meyyappan, *Electroanalysis* 2005, **17**, 15.
[3] S. Campuzano, J. Wang, *Electroanalysis* 2011, **23**, 1289.
[4] A. Walcarius, *Anal. Bioanal. Chem.* 2010, **396**, 261.
[5] D.W.M. Arrigan, *Analyst* 2004, **129**, 1157.
[6] P. Ugo, L.M. Moretto, F. Vezza, *Chem. Phys. Chem.* 2002, **3**, 917.

[7]   Y.H. Lanyon, G. De Marzi, Y.E. Watson, A.J. Quinn, J.P. Gleeson, G. Redmond, D.W.M. Arrigan, *Anal. Chem.* 2007, **79**, 3048.

[8]   L.M. Moretto, M. Tormen, M. De Leo, A. Carpentiero, P. Ugo, *Nanotechnology* 2011, **22**, 185305.

[9]   M.E. Sandison, J.M. Cooper, *Lab. Chip.* 2006, **6**, 1020.

[10] V.P. Menon, C.R. Martin, *Anal. Chem.* 1995, **67**, 1920.

[11] L.M. Moretto, N. Pepe, P. Ugo, *Talanta* 2004, **62**, 1055.

[12] J.J. Gooding, D.B. Hibbert, *TrAc. Trens. Anal. Chem.* 1999, **18**, 525.

[13] R. Gasparac, B.J. Taft, M.A. Lapierre-Devlin, A.D. Lazareck, J.M. Xu, S.O. Kelley, *J. Am. Chem. Soc.* 2004, **126**, 12270.

[14] K. Krishnamoorthy, C.G. Zoski, *Anal. Chem.* 2005, **77**, 5068.

[15] M. De Leo, A. Kuhn, P. Ugo, *Electroanalysis* 2007, **19**, 227.

[16] S. Pozzi Mucelli, M. Zamuner, M. Tormen, G. Stanta, P. Ugo, *Biosens. Bioelectron.* 2008, **23**, 1900.

[17] M. Zamuner, S. Pozzi Mucelli, M. Tormen, G. Stanta, P. Ugo, *Eur. J. Nanomed.* 2008, **1**, 33.

[18] F. Bottari, P. Oliveri, P. Ugo, *Biosens. Bioelectron.* 2014, **52**, 403.

[19] M. Silvestrini, L. Fruk, P. Ugo, *Biosens. Bioelectron.* 2013, **40**, 265.

[20] M. Silvestrini, P. Schiavuta, P. Scopece, G. Pecchielan, L.M. Moretto, P. Ugo, *Electrochim. Acta* 2011, **56**, 7718.

[21] K.J. Kim, A.G. Fane, M. Nystrom, A. Pihlajamaki, *J. Membrane Sci.* 1997, **134**, 199.

[22] M. Henry, C. Dupont-Gillain, P. Bertrand, *Langmuir* 2003, **19**, 6271.

[23] A. Heller, B. Feldman, *Acc. Chem. Res.* 2010, **7**, 963.

[24] J. Wang, *Chem. Rev.* 2008, **108**, 814.

[25] M. Portaccio, D. Durante, A. Viggiano, S. Di Martino, P. De Luca, D. Di Tuoro, U. Bencivenga, S. Rossi, P. Canciglia, B. De Luca, D. G. Mita, *Electroanalysis* 2007, **19**, 1787.

[26] P.W. Alexander, G.A. Rechnitz, *Electroanalysis* 2000, **12**, 343.

[27] J.C. Claussen, M.M. Wickner, T.S. Fisher, M.D. Porterfield, *ACS Appl. Mater. Interfaces* 2011, **3**, 1765.

[28] M. Delvaux, A. Walcarius, S. Demoustire-Champagne, *Biosens. Bioelectron.* 2005, **20**, 1587.

[29] P. Ugo, L.M. Moretto in Handbook of Electrochemistry (Ed.: C.G. Zoski), Elsevier, Amsterdam, 2007, pp. 678-709.

[30] P. Ugo, N. Pepe, L.M. Moretto, M. Battagliarin, *J. Electroanal. Chem.* 2003, **560**, 51.

[31] F.C. Pereira, L.M. Moretto, M. De Leo, M.V.B. Zanoni, P. Ugo, *Anal. Chim. Acta* 2006, **575**, 16.

[32] M. De Leo, F.C. Pereira, L.M. Moretto, P. Scopece, S. Polizzi, P. Ugo, *Chem. Mater.* 2007, **19**, 5955.

[33] E. Sabatani, J. Rubinstein, *J. Phys. Chem. B* 1987, **91**, 6663.

[34] C. Amatore, J.M. Savéant, D. Tessier, *J. Electroanal. Chem.* 1983, **147**, 39.

[35] B. Brunetti, P. Ugo, L.M. Moretto, C.R. Martin, *J. Electroanal. Chem.* 2000, **491**, 166.

[36] J.L. House, E.M. Anderson, W.K. Ward, *J. Diabetes Sci. Technol.* 2007, **1**, 18.

[37] S. Zhang, N. Wang, H. Yu, Y. Niu, C. Sun, *Bioelectrochem.* 2005, **67**, 15.

[38] P. Alzari, N. Anicet, C. Bourdillon, J. Moiroux, J.M. Savèant, *J. Am. Chem. Soc.* 1996, **118**, 6788.

[39] B. Ballarin, C.J. Brumlik, D.R. Lawson, W.P. Liang, L.S. Vandyke, C.R. Martin, *Anal. Chem.* 1992, **64**, 2647.

[40] A.E.C. Cass, G. Davis, G.D. Francis, H.A. Hill, W.J. Aston, I.J. Higgins, E.V. Plotkin, L.D. Scott, A.P. Turner, *Anal. Chem.* 1984, **56**, 667.

[41] H.J. Bright, M. Appleby, *J. Biol. Chem.* 1969, **244**, 3625.

[42] P. Alzari, N. Anicet, C. Bourdillon, J. Moiroux, J.M. Saveant, *J. Am. Chem. Soc.* 1996, **118**, 6788.

[43] J. H. Pazur, K. Kleppe, *Biochemistry-US* 1964, **3**, 578.

[44] S.B. Bankar, M.V. Bule, R.S. Singhal, L. Ananthanarayan, Biotechnol. Adv. 2009, **27**, 489.

[45] I.H. Boyaci, *Biochem. Eng. J.* 2005, **25**, 55.

[46] B.E. Swoboda, V. Massey, *J. Biol. Chem.* 1965, **240**, 2209.

Chapter 3

Electrochemical nanoimmunosensor for the detection of anti-tissue transglutaminase IgG in serum samples of pediatric celiac patients

3.1   Introduction

For decades, radioimmunoassay (RIA) and ELISA have been the major diagnostic techniques for the determination of disease biomarkers [1-4]. Recently, electrochemical biosensors are dominating in many of the clinical diagnostic protocols mainly due to high sensitivity, specificity, low detection limit, simplicity, affordability, speed and possibility of miniaturization [5-7]. The sensitivity of electrochemical biosensors principally emanates from the localization of electrochemical processes at the electrode interface [7]. In addition to the natural selectivity of the biorecognition elements, the electrochemical selectivity (by an appropriate selection of the detection potential) contributes for the high specificity of electrochemical biosensors. The high specificity in turn, minimizes the matrix interference allowing analysis of complex, colored or turbid samples, e.g. blood, with little or no sample pretreatment procedure [8]. In this context, sensitivity and specificity of a diagnostic method are measures of the diagnostic accuracy. That is, sensitivity of a clinical test refers to the ability of the test to correctly identify those patients with the disease, while specificity refers to the ability of the test to correctly identify those without the disease [9,10].

The analytical performances of electrochemical devices can be further enhanced by miniaturization of the transducers to the nanometer scale. The fact that nanosized electrodes are characterized by high density diffusion flux of electroactive species accompanied by reduced background noise enhances the analytical sensitivity and limit of detection by orders of magnitude making the devices suitable for determination of low concentration of disease biomarkers in clinical diagnosis [8, 11-20].

NEEs are part of such nanosized transducers. It was shown that the use of NEEs can improve the performances of electrochemical determinations by dramatically increasing the signal-to-background current ratios [21,22]. Twenty years back, when Menon and Martin introduced the novel protocol for preparation of metallic nanoelectrode ensembles using nanoporous PC membrane [22], the membrane template was used to control the size, shape and orientation of the nanowires or nanotubes with small roughness and large aspect- ratio.

Following the discovery, researches on the NEEs were typically focused on the refinement of the preparation, optimization, modification and utilization of the metallic surface of the NEEs. The polymeric surface of the templating membrane, on the other hand, did not receive much attention until 2008, when Ugo's group introduced the idea of exploiting for biosensing purposes both the insulating polymeric PC and the metallic nanodisk part of the NEEs, where the PC was used for biorecognition and the nanoelectrodes for transduction [23,24]. This is because, besides its outstanding mechanical, optical and biocompatible properties, PC has strong affinity to proteins [23-28].

The parallel use of the PC portion as substrate for immobilizing the biorecognition element and the electroactive surface for the electrochemical process, significantly improved the electroanalytical performances and the quality of the final analytical results as demonstrated in previous studies conducted in our group [23,24,29].

To achieve that, the capture antibody or antigen was immobilized onto the PC surface, which surrounds the nanoelectrodes, by incubating in a protein solution in suitable electrolyte, typically carbonate buffer [23,24,29,30]. The excellent capabilities of NEEs based immunosensors were previously tested in the determination of disease biomarkers where detection down to 20 pg μL^{-1} level was achieved [24].

In the present study, we use this concept towards a different analytical challenge that is to develop an NEE-based electrochemical immunosensor for CD diagnostics.

CD is one of the major health problems where serological diagnostic methods with the above properties are most sought not only for diagnosis but also for screening and follow-up tests. The serological tests are still conducted by expensive optical ELISA, fluoroenzyme immunoassay (FEIA) and indirect immunofluorescence assay methods [31-33]. Because of the limits

associated to the existing test methods, the diagnosis rate of the disease is hardly more than 15 %. On the other hand, population based surveys show that the global prevalence of the disease is on an increasing trend with incidences from regions where the staple diet is not wheat [34-37]. A number of electrochemical biosensors have been reported in the literature for diagnosis of the disease [5,38]. Yet, their practical application in the clinical arena has not satisfactorily realized. The lengthy and complex biorecognition element immobilization procedures might have contributed for the delayed practical application of the electrochemical biosensors [5,39]. Therefore, our new and simple biomolecule immobilization approach could be attractive for mass production of practically applicable devices for diagnosis of CD.

The goal is to develop a cheap, simple, accurate electrochemical immunosensor, eventually suitable for wide scale production [40-44], able to detect the anti-tTG IgG isotype in serum of pediatric CD patients. As a CD serological biomarker, the IgG isotype of anti-tTG is not commonly determined because of the relatively low sensitivity of the detection methods available up to now. However, the determination of the anti-tTG IgG isotype can offer some attractive advantages including higher specificity, suitability for CD diagnosis in individuals affected by selective IgA deficiency and in children younger than 2 years old, for whom the IgA test does not give reliable results [45-47].

As demonstrated by our group and by other authors like Rauf *et al* [16], NEEs are promising electrochemical transducers for the development of commercializable, sensitive, simple and reliable biosensors. Taking in to account the advantages of using NEEs and the urgent need of suitable diagnostic device for CD, this work was focused on the development of an immunosensor based on immobilizing the capture antigen (tTG) on the PC membrane component of the NEEs.

The architecture and expected functioning scheme of the proposed immunosensor are summarized in Scheme 3.1. The detection scheme used in the present protocol is based on the immobilization of the antigen tTG selectively on the PC surface of the NEEs to serve as a capture for the analyte. After blocking with BSA, the anti-tTG is captured by the tTG-NEE and further incubated with the secondary antibody labeled with the reporter HRP enzyme (SecAb-HRP). Finally, the presence of the label HRP which also indicates the capture of the anti-tTG, is detected by adding the enzyme substrate (namely, H_2O_2) and hydroquinone (H_2Q) as a suitable

redox mediator [48-52]. The electrochemical reaction of the redox mediator occurs at the electroactive Au nanodisks of the NEE.
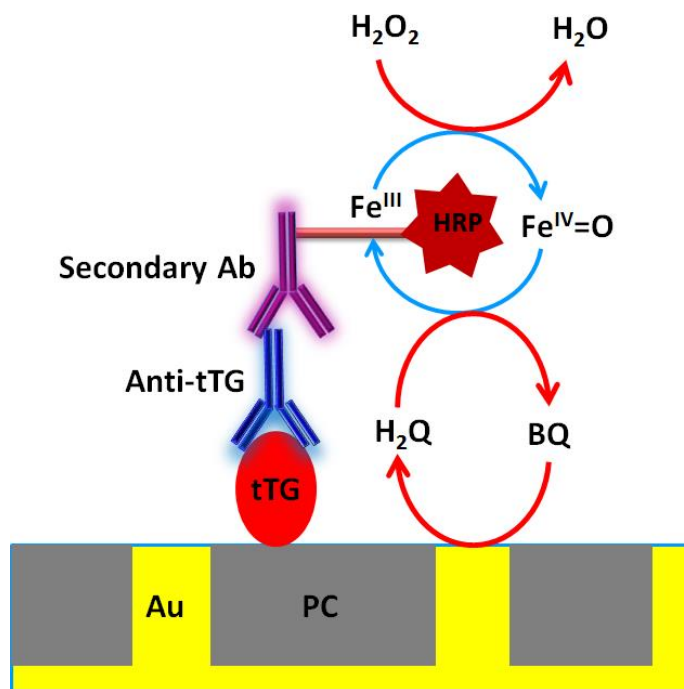
Scheme 3.1 Scheme depicting the immunosensor architecture and the associated electrochemical and enzymatic processes. *NB.* Components are not drawn to scale.

This approach avoids the lengthy electrode modification procedure, and prevents passivation or poisoning of the electrochemically active electrode surface. Since the biochemical process takes place at a distance from the surface where electrochemical processes occur, direct electron exchange between the label and electrochemically active surface may not be possible. In order to effect signal communication between the two, freely diffusible unbound redox mediator should be used. Survey of the literature indicates that hydroquinone is an efficient redox mediator to exchange electrons with the HRP label.

At the best of our knowledge, this is the first report on electrochemical immunosensor for the determination of anti-tTG IgG employing NEEs without the requirement of any preliminary surface modification.

3.2   Experimental

3.2.1 Instruments

Cyclic voltammetric measurements were performed with the CHI 660B potentiostat, an electrochemical cell with three electrodes set up was used comprising Pt spiral counter, Ag/AgCl (in saturated-KCl solution) reference and Au NEEs working (immunosensors) electrodes. Scanning electron microscope (SEM) and energy dispersive X-ray spectroscopy (EDS) analysis were performed using a TM3000 Hitachi table top scanning electron microscope coupled with a SwiftED3000 X-Ray microanalysis system.

Hydrophilic track-etched PC filter membrane (47 mm overall filter diameter, 6 µm thickness) with average pore diameter of 30 nm and pore density of 600 million pores per cm^2 from SPI supplies (West Chester, USA) was used as template for preparation of the nanoelectrode ensembles.

3.2.2 Reagents and immunochemicals

Gold electroless plating solution (Oromerse Part B, Technic Inc.), bovine serum albumin (BSA), Tween 20, hydrogen peroxide 30 % and hydroquinone (H_2Q) 99 % were purchased from Sigma. Buffer solutions, carbonate-bicarbonate buffer pH 9.2, 0.01 M phosphate buffer saline (PBS) pH 7.4 and 0.05 M phosphate buffer (PB) pH 7.4 were prepared with distilled water. All other reagents were of analytical grade. Human recombinant tissue transglutaminase (h-tTG), mouse anti-human tTG monoclonal antibody (CUB 7402), HRP labeled goat anti-human IgG (whole molecule) and serum samples are kindly supplied by Burlo Garofolo Pediatric Institute (Trieste, Italy). HRP labeled goat anti-mouse pAb IgG secondary antibody from Abcam (UK). All the biologicals including BSA, and Tween 20 were diluted using the 0.01 M PBS pH 7.4.

3.3.3 Methods

Fabrication of the NEEs

PC membranes (SPI-pore) typically with nominal 30 nm pore diameter, but also with 200 nm pore diameter as comparison, were used for preparing the NEEs. The electroless deposition of

gold nanofibers into nanopores of PC and the subsequent fabrication of gold nanoelectrode ensembles are detailed in the previous chapters. The NEEs were assembled and their morphology, chemical composition and electrochemical behavior were investigated using SEM, EDS and cyclic voltammetry respectively (see Chapter 2).

Immunosensor construction and electrochemical detection

The antigen human tissue Transglutaminase, tTG, was immobilized on the NEE adapting the method described by Pozzi Mucelli *et al* for Trastuzumab [23,24]. Briefly, after thorough washing of the Au NEE with Mill-Q water, 20 µL of 10 µg mL^{-1} of h-tTG solution in 0.1 M carbonate buffer, pH 9.2, was casted on the NEE and incubated for 2 h. The h-tTG-NEE was washed with 0.01 M 1X PBS, pH 7.4 and subsequently incubated with 1 % BSA in 0.01 M PBS, pH 7.4, for 30 min to block nonspecific binding. The h-tTG-NEE was washed with PBS, pH 7.4, and incubated with 20 µL of 5 µg mL^{-1} mouse anti-h-tTG antibody solution for 60 min. After washing with PBS pH 7.4 containing 0.05 % Tween 20 followed by rinsing with the buffer, the captured primary antibody was reacted with 20 µL of 10 µg mL^{-1} HRP labeled goat anti-mouse IgG secondary antibody for 60 min. Incubations were carried out at room temperature (22 ± 1°C), in a water vapor saturated vessel. All washing procedures were followed by drying with a gentle N_2 flow. Finally, the immunosensor was dipped in an electrochemical cell containing freshly prepared 1 mM H_2Q in 0.05M phosphate buffer (pH 7.4). The H_2Q solution was prepared under N_2, in an amber glass bottle to avoid oxidation by atmospheric O_2 and light. All electrochemical measurements were performed at room temperature, in an electrolyte solution de-aerated with N_2. Cyclic voltammograms were recorded before and after addition of 1.5 mM H_2O_2 at scan rate of 50 mV s^{-1} between -0.65 and +0.85 V. Negative controls were performed in the absence of anti-tTG.

3.3 Results and discussion

3.3.1 Voltammetric behaviors of H_2Q at bare NEEs

The cyclic voltammetric behavior of the H_2Q redox mediator was studied at unmodified flat conventional gold electrode and two kinds of NEEs that differ in the diameter of the nanoelectrodes. In particular, NEEs fabricated using PC templates of 30 nm or 200 nm pore

diameter (hereafter abbreviated as NEE-30 and NEE-200) were compared. The overall geometric area of the three electrodes was kept the same, namely 0.071 cm^2.

The CV patterns recorded with the three electrodes in 1 mM H$_2$Q at scan rate of 50 mV s^{-1} are shown in Figure 3.1. The red colored CV was recorded at a flat gold conventional electrode, while the blue and black line curves represent CVs recorded at NEE-200 and NEE-30, respectively. A pair of well defined anodic and cathodic peaks was recorded, in agreement with previous literature reports conducted on macroelectrodes [49-57] which attributed the signals to the 2-electrons/ 2-protons electrochemical oxidation of H$_2$Q to benzoquinone (BQ).
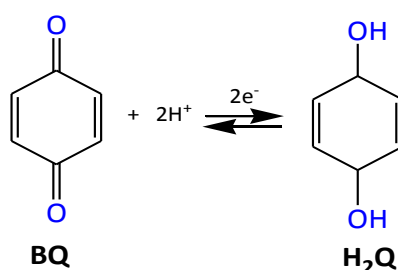
The fact that the transfer of the two electrons occurs under a single voltammetric peak at all electrodes studied here, indicates that the first electron transfer event brings the H$_2$Q to a semiquinone state which favors the very fast transfer of the other electron making the semiquinone undetectable in aqueous solutions [53,56,58,59]. The involvement of protons, on the other hand, makes the electrochemical and chemical processes dependent on the solution pH [54]. Therefore, all electrochemical measurements are carried out in buffer solution to keep the pH of the system constant.

The corresponding anodic to cathodic peak potential separations (ΔE_p), and peak current ratios (I_{pa}/I_{pc}) are calculated at scan rate of 50 mV s^{-1}. The ΔE_p values were found to be 0.100, 0.979 and 1.075 V for the conventional flat Au electrode, for NEE-200 and NEE-30, respectively. The I_{pa}/I_{pc} values were found to be 0.95, 1.01 and 3.18 in the same order. These results indicate that H$_2$Q exhibits better reversibility with the flat conventional gold electrode than with NEEs. Such CV behavior at macro gold electrode was also reported by Zhuo *et al* [60]. While the two types of NEEs offered quasi-reversible electrochemistry.
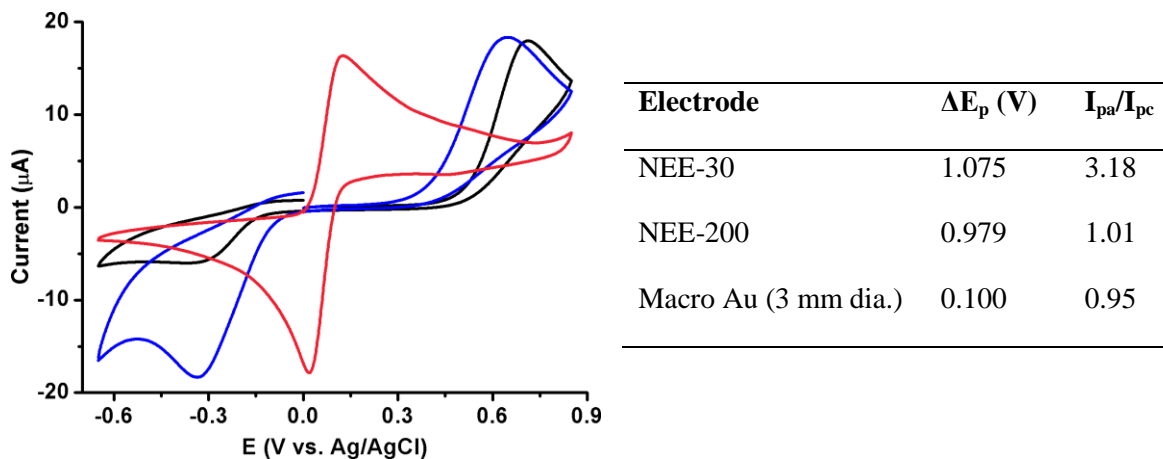
Electrode	ΔE_p (V)	I_{pa}/I_{pc}
NEE-30	1.075	3.18
NEE-200	0.979	1.01
Macro Au (3 mm dia.)	0.100	0.95

Figure 3.1 Cyclic voltammetric behaviors of H_2Q (1 mM in PBS) at Au NEEs prepared using 30 nm (black line) and 200 nm (blue line) pore diameter PC, and at a macro gold electrode (red) with the same geometric area as the NEEs, i.e. 3 mm diam. The corresponding peak potential separations (ΔE_p) and peak current ratios are shown in the *inset* table. NEE-30 and NEE-200 represent NEEs fabricated using PC templates with 30 nm and 200 nm pore diameters respectively. Scan rate 50 mV s^{-1}.

A behavior similar to the one observed here with NEEs, has been similarly observed for H_2Q electrochemistry at chemically modified macroelectrodes [50,57]. This agrees with the fact that NEEs behave as electrodes with partially blocked surface (PBSEs) [22,61,62]. Indeed, as demonstrated by Amatore in 1983 [63] and recent theoretical models [64-66] the nanodisk electrodes of NEEs are the unblocked surfaces while the PC template membrane is the blocking material [67]. Our result also evidenced slower heterogeneous electron transfer kinetics for a NEE with smaller nanodisk electrodes (NEE-30 *vs* NEE-200) typically because the rate of heterogeneous electron transfer is inversely proportional to the extent of blockage. NEEs produce a current response identical to that of a naked electrode of the same overall geometric area, but with a smaller apparent rate constant ($k°_{app}$) for the electron transfer which decreases as the coverage of the surface increases. The apparent rate constant ($k°_{app}$) is related to the true standard rate constant by the following equation [22,63,67]:
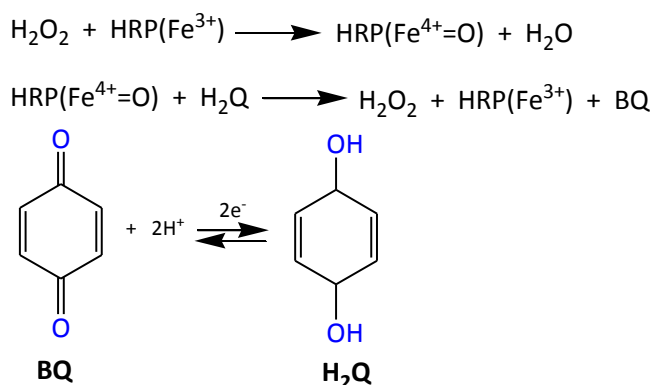
$$k°_{app} = k°(1 - \vartheta) = k° f$$

where $\vartheta = (A_{geom} - A_{act})/A_{geom}$ and f is the fractional electrode area $(f = A_{act} / A_{geom})$.

3.3.2 Detection of anti-tTG antibody

The broken line CV in Figure 3.2A shows the electrochemical behavior of H_2Q at a NEE functionalized with tTG – Anti-tTG – SecAb-HRP, as described in the experimental part. It exhibits a CV pattern for H_2Q comparable with that recorded at a bare NEE (Figure 3.1, black curve). This means that the functionalization of the NEE does not inhibit the electrochemical process of H_2Q at the nanodisks, indicating that the proteins are bound mainly on the PC surface, in agreement with previous observations [23,29], or if they adsorb on the Au surface of the NEE, they do not hinder the electrochemistry.

The full line CV in the same figure, recorded after the addition of 1.5 mM H_2O_2, is characterized by a sharp increase of the reduction peak at -0.4 V and the disappearance of the re-oxidation peak at 0.75 V. This indicates the occurrence of an enzyme mediated electrocatalytic process governed by the following chemical, electrochemical and enzymatic processes [51,52,68]:

$$H_2O_2 + HRP(Fe^{3+}) \longrightarrow HRP(Fe^{4+}=O) + H_2O$$

$$HRP(Fe^{4+}=O) + H_2Q \longrightarrow H_2O_2 + HRP(Fe^{3+}) + BQ$$

BQ $+ 2H^+ \underset{}{\overset{2e^-}{\rightleftharpoons}}$ **H₂Q**

In practice, H_2Q is oxidized to BQ by H_2O_2 in a reaction catalyzed by HRP, and BQ is reduced to H_2Q at the Au nanodisks. On the basis of previous reports [51,52,68], during the initial enzyme-substrate reaction, the $HRPFe^{3+}$ active center of the enzyme is oxidized to a ferryloxyHRP ($HRPFe^{4+}=O$) specie which is then chemically reduced regenerating the original form of the enzyme by a concomitant oxidation of the H_2Q mediator to BQ. The BQ is subsequently reduced back to H_2Q by an electrochemical reaction during the cathodic reverse scan resulting in a steady state current proportional to the enzyme and analyte concentrations.

The broken line in Figure 3.2B, on the other hand, displays the CVs recorded at a NEE functionalized with tTG – anti-tTG – SecAb-HRP in a fresh solution of H_2Q and in a potential

range of 0.2 to -0.65 V. In this case, no recognizable cathodic peak characteristic of reduction of BQ to H_2Q was detected. This observation means that the oxidation of H_2Q did not occur in the system because neither sufficient oxidizing potential (0.7 V) was applied, nor the enzyme is activated. However, following the addition of the H_2O_2, an abruptly increased cathodic peak current was recorded, indicating that the enzymatic reaction is initiated by the presence of the enzyme substrate which eventually produces the oxidized form of the redox mediator.
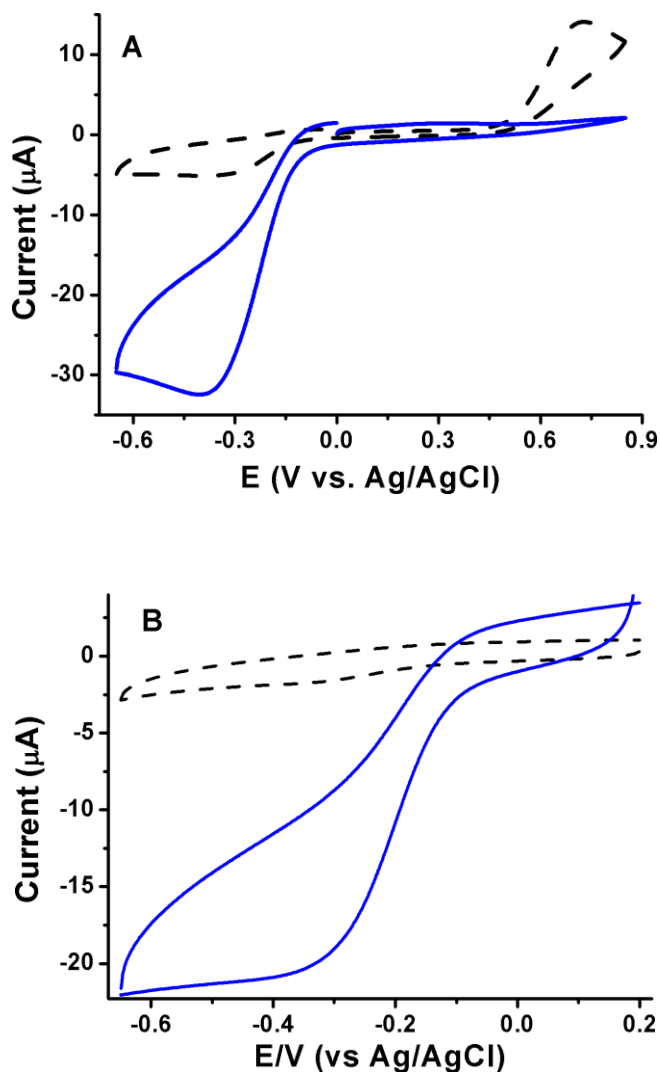
Figure 3.2 Cyclic voltammograms obtained with the 1 μg mL^{-1} anti-tTG immunosensor in deoxygenated 0.05 M PBS (pH 7.4) containing freshly prepared 1 mM H_2Q before (dash lines) and after (solid lines) addition of 1.5 mM H_2O_2. **A**) Initial anodic scan reaching to the H_2Q oxidation potential, and **B**) initial cathodic scan without reaching to the H_2Q oxidation potential during the anodic reverse scan. Scan rate of 50 mV s^{-1}.

Figure 3.3 compares the cyclic voltammetric curves at a well cleaned NEE in 1 mM H_2Q in the absence (dashed line) and presence (full line) of 1.5 mM H_2O_2. The fact that the CV profile of H_2Q is not altered by the presence of H_2O_2 evidences the absence of a direct chemical reaction between H_2O_2 and H_2Q although it is thermodynamically feasible, which is inline with a previous report by Zhou *et al* [52].
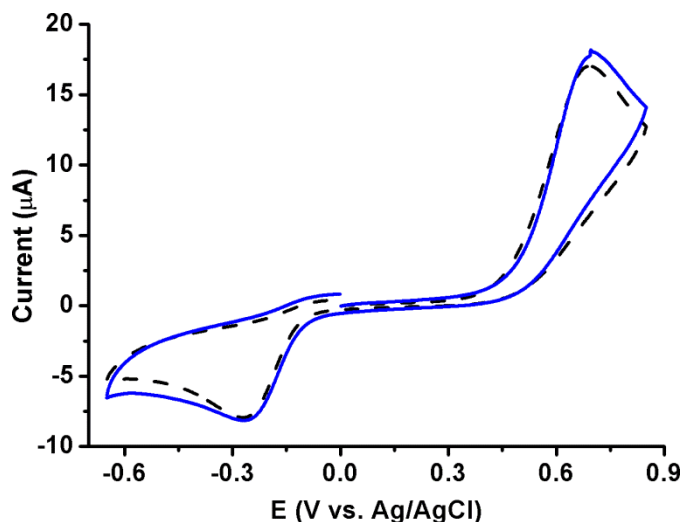

Figure 3.3 Cyclic voltammograms recorded at a bare Au NEE in 0.05 M PBS (pH 7.4) containing 1 mM H_2Q before (dash line) and after (solid line) addition of 1.5 mM H_2O_2. Scan rate 50 mV s^{-1}.

3.3.3 Optimization of signal detection parameters

To maximize the immunosensor response (I_{net}), experimental parameters need to be optimized, namely the concentrations of the enzyme substrate H_2O_2 and the mediator H_2Q. These parameters were optimized keeping constant at 1µg mL^{-1} concentration of the anti-tTG analyte.

Figure 3.4A depicts the change in voltammetric responses of the immunosensor upon increasing of the H_2O_2 concentration (from 0 to 2.5 mM). In this range of concentration, the cathodic catalytic current scales with the H_2O_2 concentration. With concentrations up to 1.5 mM, a well defined cathodic peak was obtained at about the reduction potential of H_2Q. Upon increasing of the concentration above 1.5 mM, the peak becomes unidentifiable and the current continuously increases after the peak potential. The continuous increment in current after the cathodic peak potential of H_2Q may be associated to the electrochemical reduction of the excess H_2O_2 which is inline with the same but slight cathodic current increment observed in Figure 3.3 after addition of

H_2O_2. Concentrations lower than 1.5 mM, on the other hand, seem to be insufficient to achieve an efficient catalytic regime. In order to reliably determine the concentration of the analyte based on the catalytic current of the redox enzyme label (HRP), the catalytic process must be limited by the concentration of the HRP. In other words, the substrate and the redox mediator need to be in suitable excess to insure complete oxidation and reduction of the enzyme, respectively. Therefore, 1.5 mM H_2O_2 was chosen as the optimal substrate concentration for the continuation of this work.

The effect of the concentration of the redox mediator on the cyclic voltammetric behavior of the immunosensor in a solution containing 1.5 mM H_2O_2 is reported in Figure 3.4B.

The cathodic peak current correspondingly increased with the concentration of H_2Q up to 0.75 mM and leveled off for further increment of the concentration to 1.0 mM. This is a typical indicator of a mediated electrochemical process. At low mediator concentration, the current response is limited by the kinetics of the enzyme-mediator reaction. When the mediator concentration is high, the current response becomes independent of the enzyme-mediator step but is limited by enzyme-substrate kinetics. However, a higher concentration, such as 1.25 mM, produces a broad cathodic peak. Based on these results, 1.0 mM of H_2Q is chosen as the best suitable concentration.
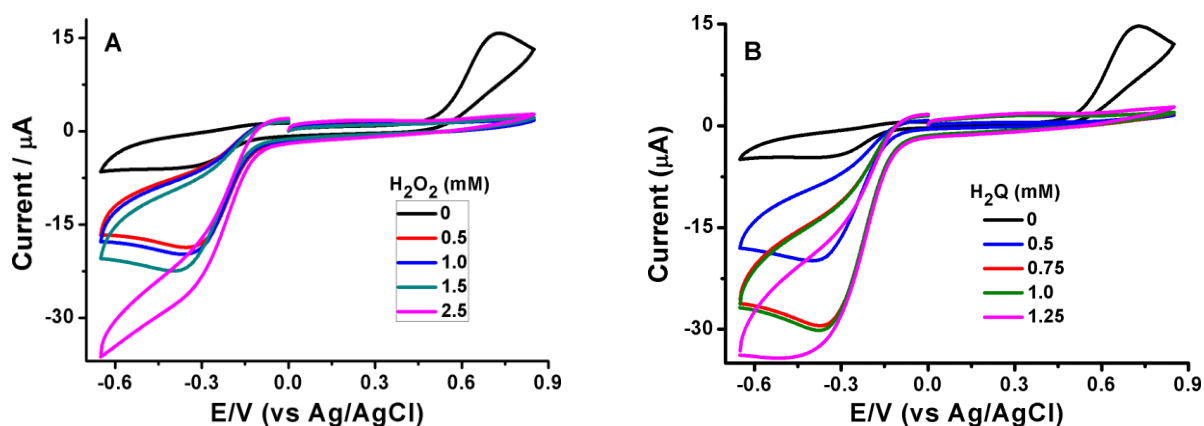

Figure 3.4 Cyclic voltammetric responses of a 1 μg mL^{-1} anti-tTG immunosensor, **A**) in 1 mM H_2Q in PBS containing different concentrations of H_2O_2, and **B**) in 1.5 mM H_2O_2 in PBS containing different concentrations of H_2Q. Scan rate 50 mV s^{-1}.

In addition, the effect of the scanning potential window and direction of the sweep on the CV responses of the immunosensor were (see Figure 3.2) studied and results are reported in Figures 3.5 and 3.6. Since the signal detection strategy in the immunosensor is based on the determination of enzymatically produced BQ, its measurement was carried out in two ways: i) direct electrochemical reduction of the BQ to H_2Q by applying a cathodic potential sweep between +0.2 and -0.65 V, ii) by three segment cyclic voltammetry with an initial scan from 0 to +0.85 V, reversed to -0.65 and finally back to 0. Calibration curves of serial dilutions of anti-tTG were developed based on the two approaches (Figure 3.5); however, for further experiments the second approach was preferred.
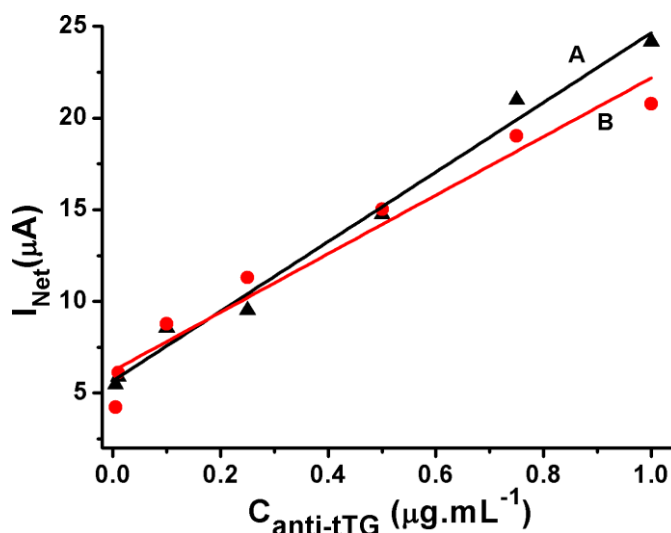
Figure 3.5 Calibration curves of the immunosensor with **A**) an initial anodic scan reaching to the H_2Q oxidation potential, and **B**) an initial cathodic scan without reaching to the H_2Q oxidation potential during the anodic reverse scan.

This choice is supported by the following reasons: i) the second approach offered better sensitivity (as evidenced by the larger value for the slope of the calibration curve) (Figure 3.5), and reproducibility on repetitive scans (Figure 3.6); ii) the observation of the decrease in the anodic peak current resulting from the enzyme catalytic process, offers an additional proof for the occurrence of the enzymatic process (Figure 3.6A).
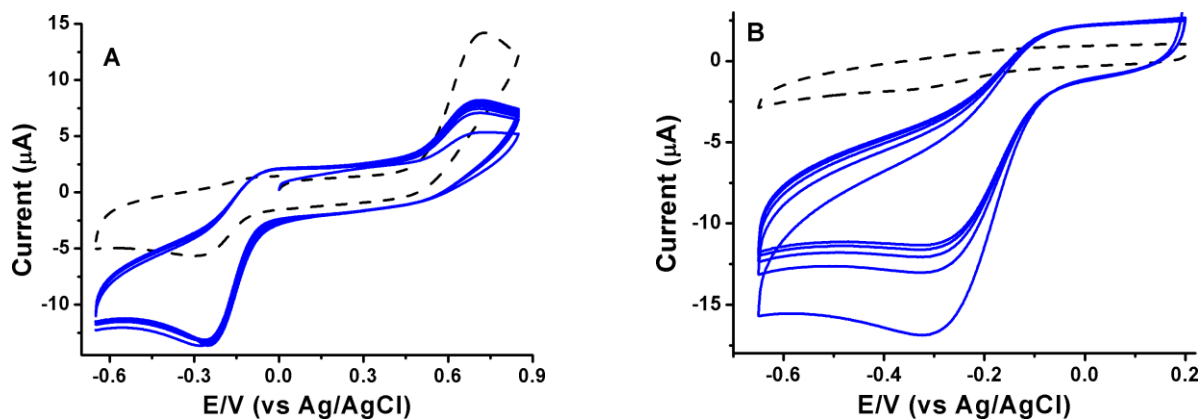
Figure 3.6 Multiple continuous scans with a 0.01 μg mL^{-1} anti-tTG immunosensor at 50 mV.s^{-1}, **A**) with initial anodic scan reaching the H$_2$Q oxidation potential, and **B**) with initial cathodic scan not reaching the H$_2$Q oxidation potential during the anodic reverse scan. Parameters are as in Figure 3.2.

3.3.4 Evaluation of non-specific binding

Figure 3.7A reports CVs recorded at a NEE incubated with 1 % BSA and SecAb-HRP followed by appropriate thorough washing step with 0.05 % Tween 20. The dashed line CV, recorded in H$_2$Q, coincides with the full line curve recorded after addition of 1.5 mM H$_2$O$_2$. This evidence indicates that, the BSA blocking step effectively prevents the non-specific binding of SecAb-HRP on the PC and Au surfaces of the NEE. Indeed, in contrast with the result in Figure 3.2A (which can be considered as a positive control), the addition of H$_2$O$_2$ did not result in the appearance of any electrocatalytic peak during the reverse scan. Also, it does not reflect in any decrease of the anodic peak current of the CV. Both evidences support the absence of HRP on the surface of the NEE.

The CVs in Figure 3.7B were recorded at NEE treated in the same procedure as in Figure 3.2A, but the incubation step with the analyte solution (anti-tTG in PBS) was substituted with incubation with PBS, for the same duration of time. The broken line CV recorded at the modified NEE in H$_2$Q solution overlaps with the broken line CV recorded after addition of H$_2$O$_2$. This negative control further confirms the absence of non-specific adsorption of SecAb-HRP on the surface of the NEE or any of the proteins used in the experiment.

It is reported that the occurrence of nonspecific binding compromises the analytical sensitivity and detection limit of the method [52]. The extra signal generated by the non-specifically bound bioconjugates disproportionate the detected signal and the analyte concentration.
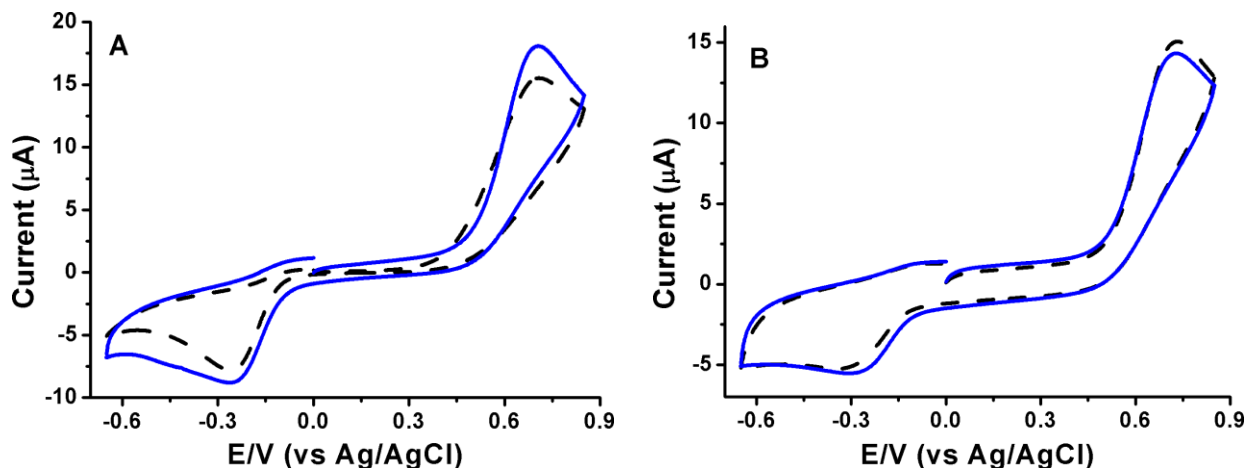

Figure 3.7 Cyclic voltammograms in 1 mM H_2Q in 0.05 M PBS pH 7.4 before (dash lines) and after (solid lines) adding 1.5 mM H_2O_2 at scan rate of 50 mV s^{-1}; **A**) NEE incubated with 1 % BSA, then with SecAb-HRP and thoroughly washed with 0.05 % Tween 20, **B**) negative control in which the anti-tTG, 0.01 M PBS incubation step is replaced by incubation in PBS alone.

3.3.5 Quantitative analyses

The dependence of the detected catalytic peak current signal at the immunosensor on the anti-tTG concentration is shown by data in Figure 3.8. The experiments were performed in triplicates by incubating different NEEs with serial dilutions (0.001 to 10 µg mL^{-1}) of monoclonal standard mouse anti-tTG. The CV responses of four representative concentrations are reported in Figure 3.8A. The parameter analytically useful for identifying and quantifying anti-tTG is the electro-catalytic current increment (I_{net}) defined as the difference between the catalytic current recorded after addition of H_2O_2 and the peak current of H_2Q in the absence of H_2O_2 in absolute value at a potential of -0.35 V:

$$I_{net} = |i_{catalytic(H2Q + H2O2)} - i_{pc(H2Q)}|$$

The I_{net} value taken at -0.35 V scales linearly with the concentration of the anti-tTG ($C_{anti-tTG}$) in the range of 0.005 to 1 µg mL^{-1}, as shown in Figure 3.9B. For concentrations above 1 µg mL^{-1}

(particularly 2.5, 5, and 10 µg mL^{-1}) (Figure 3.8), the curve acquires an asymptotic profile typical of an enzymatic reaction.
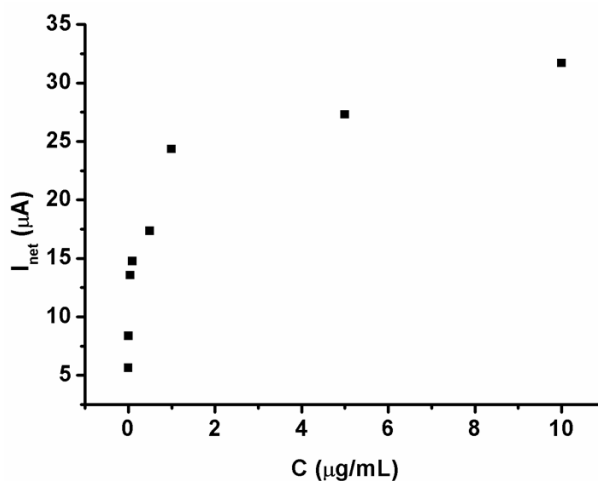

Figure 3.8 A plot of the electrocatalytic current at the immunosensor *vs* concentration of anti-tTG in the concentration range of 0.005 to 10 µg mL^{-1}.

For concentrations < 1 µg mL^{-1}, the resulting high correlation coefficient (R^2 = 0.990), and the short error bars of the calibration plot confirm the excellent reproducibility of the proposed biosensor; note that a different NEE was used for each concentration. The precision (reproducibility) of the method, evaluated as the relative standard deviation (RSD) (n=10) for a concentration of 0.5 µg mL^{-1} anti-tTG, results of 2.6 % while the detection limit (DL) is 1.8 ng mL^{-1}. DL was calculated as DL = 3(SD/m) where, where SD is the standard deviation of y-intercepts of the regression lines and "m" is the slope (sensitivity) of the calibration plot. Besides the simplicity of our protocol, the low detection limit [39], the wide linear range [50,69] and excellent reproducibility indicate that our immunosensor offers better analytical performances than other electroanalytical sensors developed for the same goals [39,69].
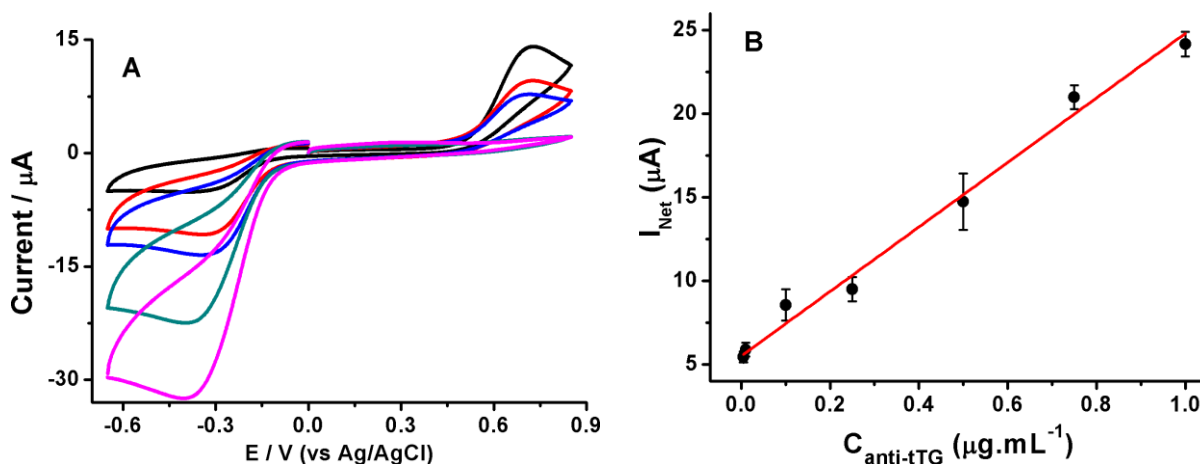
Figure 3.9 A) Cyclic voltammograms of different concentrations of anti-tTG (0, 0.005, 0.01, 0.1 and 1 µg mL^{-1}) using conditions identical to in figure 3.1, and **B**) the corresponding calibration plot of immunosensor net peak current (I_{Net}) vs analyte concentration. Error bars show standard deviations of triplicate measurements (n=3).

3.3.6 Analysis of clinical serum samples

The feasibility of the proposed immunosensor for clinical applications was evaluated by analyzing the anti-tTG IgG level of 28 clinical serum samples of pediatric patients aged between 2 and 16 years. Out of the 28 serum samples, 23 were taken from patients with confirmed CD diagnosis whereas; the other 5 were taken from healthy individuals. The anti-tTG IgA levels of the CD positive samples ranged from 16 to 776 U mL^{-1} (Table 3.1, as determined by the fluoroenzyme immunoassay method.

In order to set optimum dilution of the serum samples, preliminary investigations were performed at 1:10, 1:50, 1:100, and 1:200 dilution ratios with 0.01 M PBS, pH 7.4. The 1:200 dilution was chosen for the analysis of all the serum samples due to better catalytic peak current signal. Moreover, higher dilution minimizes possible interferences form other proteins present in the matrix [39]. Figures 3.10A-D show CV responses recorded on four representative real serum samples. The dashed lines show the CVs recorded at NEEs functionalized in the same way as reported in the experimental part, except that the incubation steps with mouse anti-tTG and HRP labeled goat anti-mouse IgG, were replaced by incubation in diluted serum samples and HRP

labeled goat anti-human IgG respectively. The full line CVs refer to voltammograms recorded after adding 1.5 mM H_2O_2. Each of the 28 serum samples was tested following the same procedure but each was analyzed using different NEEs. The existence and the intensities of the catalytic peak currents recorded at the immunosensors after addition of H_2O_2, allows one to detect both the presence and the concentration of anti-tTG IgG in the serum samples.

Quantification of signals, based on the increase in the catalytic peak current, was performed by interpolation with the calibration plot reported in Figure 3.9B. The final concentrations of the anti-tTG IgG, displayed in Table 3.1, were calculated taking in to account the dilution factor.

As illustrated by the CVs in Figure 3.10A, for serum samples taken from healthy subjects, the recorded catalytic current values are considerably lower. However, signals detected from most of the clinically proved CD patients are reasonably intense (e.g. Figure 3.10B-D), and the trend agrees to a certain extent with anti-tTG IgA concentration determined by fluoroenzyme immunoassay (shown in Figure 3.11).
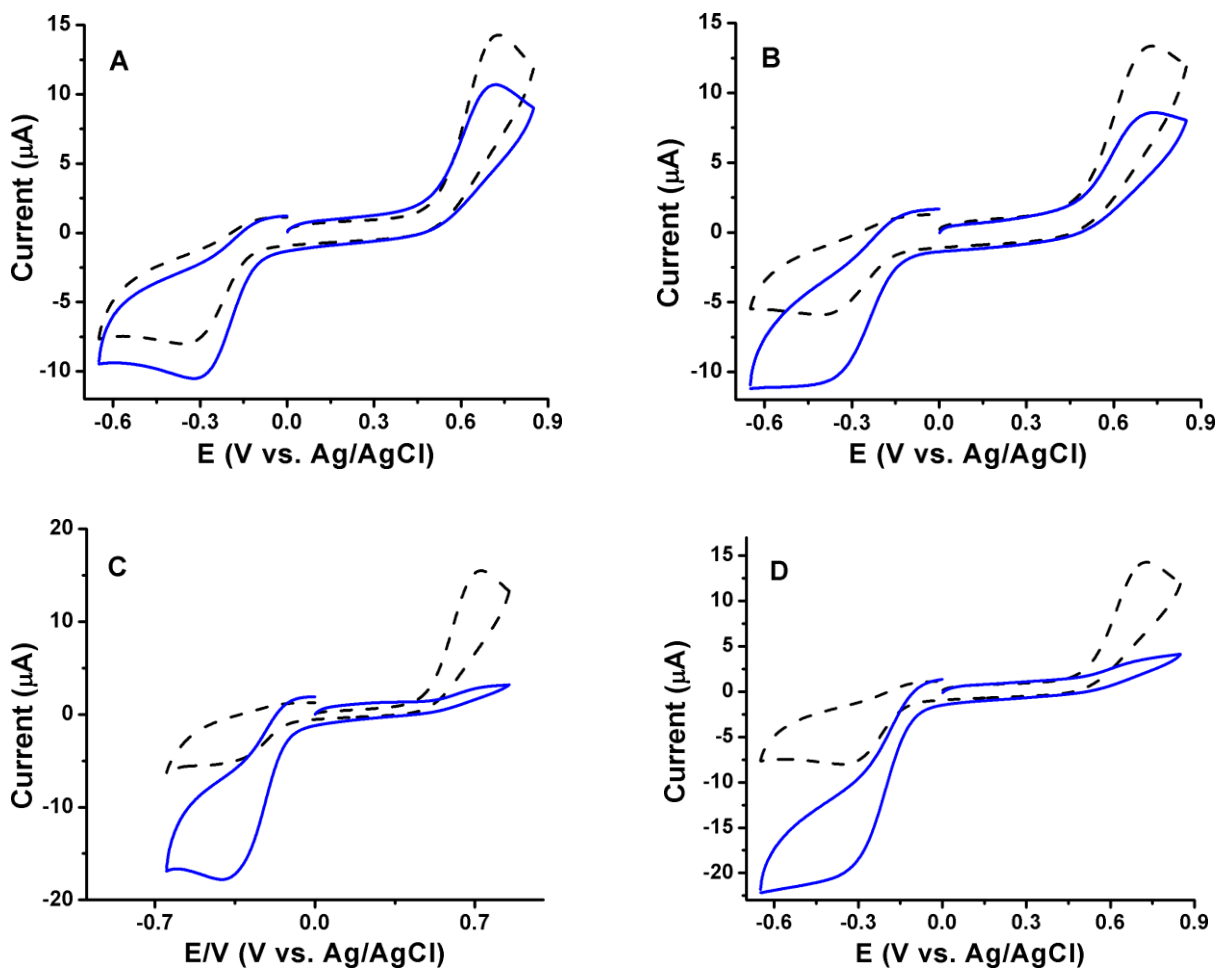
Figure 3.10 Cyclic voltammetric responses of four serum samples 10636 with the proposed immunosensor in deoxygenated 0.05 M PBS (pH 7.4) containing freshly prepared 1 mM H_2Q before (dash lines) and after (solid lines) addition of 1.5 mM H_2O_2: Samples **A**) 10691, **B**) 10623, **C**) 10636 and **D**) 10633. Scan rate 50 mV s^{-1}.

Although the appearance of the catalytic peak current reflects the presence of the anti-tTG IgG in the serum sample, it does not necessarily indicate a positive diagnosis with respect to CD, since the anti-tTG antibody is present also in the blood of healthy individuals. Therefore, in order to discriminate bloods of CD patients from those of healthy individuals, a cut-off limit should be set for the diagnostic method. For an optimized protocol, further dedicated studies are required in order to set a reliable cutoff value. This requires the evaluation of the diagnostic sensitivity (true positive) and specificity (true negative) of the method.

Table 3.1 Average anti-tTG IgG and IgA concentrations determined by the proposed electrochemical immunosensor (ECIS) and clinical fluoroenzyme immunoassay (FEIA) methods respectively.

Serum Sample	IgG (µg/ml) by ECIS	IgA (U/ml) by FEIA	Serum Sample	IgG (µg/ml) by ECIS	IgA (U/ml) by FEIA
10669	41.3	366	10644*	13.22	0.1
10658	15.855	232	10550	27.28	420
10636	37.08	442	10526	36.34	425
10668	1.405	112	10525	0	16
10637	17.12	68	10521	2.15	41
10650	22.4	273	10519	1.75	39
10623	12.06	165	10633	47.88	776
10607	0	57	10645*	0	0
10603	14.14	238	10691*	0	0
10605	7.68	116	9830	10.22	128
10562	29.58	81	9777	25.54	200
10577	20.06	80	9597*	0	0
10594	25.3	643	9463*	0	0
10554	20.38	334	9784	4.42	100

Samples where clinical reports indicated absence of CD (healthy)

In order to compare the performance of the IgG based new method with the clinically used IgA fluoroenzyme immune assay (FEIA), statistical treatments using Spearman's and Pearson's correlations were performed and the respective correlation coefficients are displayed in Figure 3.12.

The Spearman's correlation (r_s) is an important statistical parameter that measures the strength of a monotonic relationship between paired data sets [70-73]. The Pearson's coefficient (r), on the other hand, quantifies the reliability of the existence of a linear relationship between the two data sets. The values of the two correlation coefficients should range between 1 and -1 [70-73].

From our results, the calculated Spearman's correlation coefficient is 0.84 (> 0.8), indicating a *very strong correlation* between the two data sets [72]. The Pearson coefficient is 0.66 showing a *strong positive* linear relationship between the results of the two methods [73].
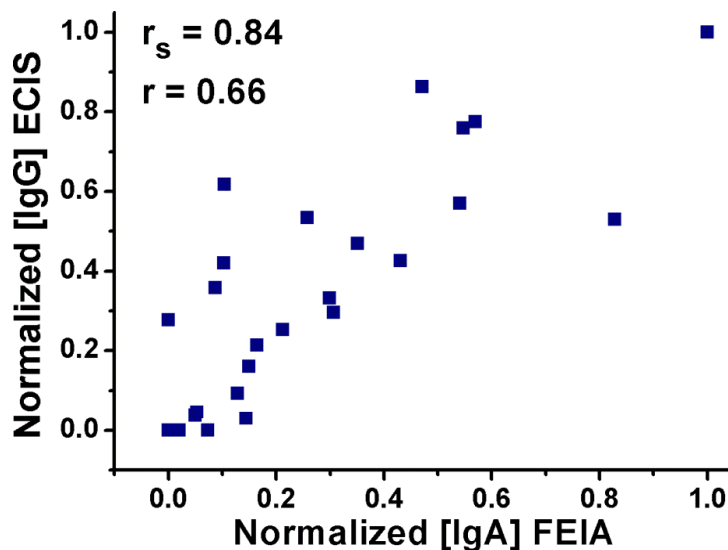
Figure 3.11 Scattered plot of normalized concentrations of real clinical serum samples obtained by the new electrochemical immunosensor (ECIS) vs the standard fluoroenzyme immunoassay (FEIA). Spearman's coefficient (r_s) of 0.84 and Pearson's correlation (r) of 0.66 are obtained.

Besides the strong agreement between the IgG level measured using the new method and the corresponding IgA level determined by the clinical FEIA method, a preliminary set of experiments conducted on few of the serum samples (data not shown) suggests that the new immunosensor can furnish better sensitivity than the clinical FEIA method when the IgG isotype is the analyte of interest.

3.3.7 Precision and stability of the anti-tTG immunosensor

Trial of regenerating the NEEs from the already used immunosensors was not successful. Therefore, each analyte solution was determined using different NEEs. In order to investigate the possible variability between the immunosensors developed from different NEEs, inter-assay precision (or the fabrication reproducibility) was estimated by determining the anti-tTG level in a standard analyte solution with three immunosensors independently. The standard deviation of the catalytic peak currents of CVs of the inter-assay (n=3) was 7.8 %, using 1μg mL^{-1} anti-tTG, that is an acceptable reproducibility.

In order to study the stability of the immunosensor on storage, follow-up studies were carried out by performing repetitive determinations of 1 μg mL^{-1} anti-tTG for a period of 7 days. The storage stability of the immunosensor was investigated by measuring the immunosensors'

catalytic current response every other day (data shown in Table 3.2). When the immunosensor was not in use, it was stored in 0.01 M PBS pH 7.0 at 4 °C. About 5% loss of catalytic peak current was observed on the 3rd day of sensor preparation. The response of the immunosensor decreased to about 75% on day 7 of the preparation. These results suggest that the immunosensor can be stored for few days without losing significant level of its performance. However, further studies on the storage conditions and nature of loss of catalytic current should be conducted in order to maintain its performance for prolonged time.

Table 3.2 The net peak catalytic current (I$_{net}$) values recorded on the 1st, 3rd, 5th and 7th days from the preparation of the immunosensor, and the corresponding decline in catalytic peak current with respect to the response recorded on the 1st day of preparation.

Day	I$_{net}$ (µA)	% decrease in I$_{net}$ (µA) from day 1
1	27.75	-
3	26.33	5.1
5	24.62	11.3
7	20.91	24.6

This indicates that the PC surface provided a biocompatible microenvironment around the biological molecules to retain the biological activity over a sufficiently extended time lag. Moreover, the interaction between the tTG antigenic molecule and the PC surface of the NEE is strong enough that there is no significant leaching of biomolecules on reasonable period of storage and during repetitive electrochemical measurements (Figure 3.5 can be referred).

3.4   Conclusions

A highly sensitive NEEs based electrochemical immunosensor was developed and evaluated for the determination of the IgG anti-tTG isotype involved in celiac disease. This is, up to now, the first report demonstrating the application of NEEs as a platform for the detection of CD biomarkers. The use of a smart biomolecule immobilization approach, where the capture antigen is selectively immobilized on the PC component of the Au NEEs, helped us to retain the desirable advantages of nanoelectrode ensembles, such as high S/N ratio. Moreover, the absence of any surface pretreatment step of the transducer for biorecognition element immobilization

reduces the analytical steps and the reagents required which is advantageous for transforming the proposed protocol to practical application.

The results presented in this work confirm the applicability of NEEs for the reliable detection of disease biomarker with a low detection limit of 1.8 ng mL^{-1}. In the new biosensor design, the use of a redox mediator in the electrolyte solution is mandatory for achieving a high level of sensitivity; note that large proportion of the reporter label is distantly located (approximately up to 200 nm) from the electroactive nanodisks where electrochemical signal is generated but is reached by the mediator since NEEs operate under a total overlap diffusion regime. The immunosensor is able to detect the disease biomarker with a wide calibration linear range (0.005 to 1µg mL^{-1}) and with excellent signal reproducibility.

In addition, the present immunosensor is capable of detecting the anti-tTG IgG biomarker in clinical pediatric serum samples, offering strong agreement with the clinical outcome obtained for IgA isotype using the FEIA method. However, a preliminary experiment conducted on few of the serum samples has shown that the new immunosensor furnishes better sensitivity than the clinical FEIA method when the IgG isotype is measured by both methods. Further studies aimed at standardizing the method and setting an anti-tTG IgG cut-off point to reliably discriminate between positive and negative serum samples is in progress, using standardized blood samples. Based on the results obtained here, the present immunosensor shows interesting prospects to play the role of a real world sensor for the decentralized serological diagnosis of CD, possibly overcoming the requirement of performing an invasive confirmatory biopsy.

References

[1] R. O'Kennedy, M. Byrne, C. O'Fagain, G. Berns, *Biochem. Educ.* 1990, **18**, 126.

[2] A. Voller, A. Bartlett, D. E. Bidwell, *J. Clin. Pathol.* 1978, **31**, 507.

[3] S. J. Goldsmith, *Semin. Nucl. Med.* 1975, **5**, 125.

[4] R. S. Yalow, *Pharmacol. Rev.* 1973, **25**, 161.

[5] D. Martin-Yerga, M.B. Gonzalez-Garcia, A. Costa-Garcia, *Talanta* 2014, **130**, 598.

[6] C. Zhu, G. Yang, H. Li, D. Du, Y. Lin, *Anal. Chem.* 2015, **87**, 230.

[7] L. Ding, D. Du, X. Zhang, H. Ju, *Curr. Med. Chem. 2008*, ***15***, 3160.

[8] N. J. Ronkainen, S.L. Okon, *Materials* 2014, **7,** 4669.

[9] A.K. Akobeng, *Acta Paediatr*, 2007, 96, 338 – 41.

[10] A.G. Lalkhen, A. McCluskey, *Continuing Education in Anaesthesia, Critical Care & Pain* 2008, 8, 221 – 223.

[11] J. Cabaj, J. Soloducho, *Mater. Sci. Appl.* 2014, **5**, 752.

[12] P. Hu, X. Zhou, Q. Wu, *Nanoscale Res. Lett.* 2014, **9**, 76.

[13] A. Chen, S. Chatterjee, *Chem. Soc. Rev.* 2013, **42**, 5425.

[14] P. Tomcik, *Sensors* 2013, **13**, 13659.

[15] J.F. Rusling, *Chem. Rec.* 2012, **12**, 164.

[16] S. Rauf, M.J.A. Shiddiky, A. Asthana, K. Dimitrov, *Sensor. Actuator. B* 2012, **173**, 491.

[17] J.I. Yeh, H. Shi, *WIREs Nanomed. Nanobiotechnol.* 2010, **2**, 176.

[18] J.F. Rusling, G. Sotzing, F. Papadimitrakopoulos, *Bioelectrochemistry* 2009, **76**, 189.

[19] Y.H. Yun, Z. Dong, V. Shanov, W.R. Heineman, H. B. Halsall, A. Bhattacharya, L. Conforti, R.K. Narayan, W.S. Ball, M.J. Schulz, *Nanotoday* 2007,**2**, 30.

[20] C. Jianrong, M. Yuqing, H. Nongyue, W. Xiaohua, L. Sijiao, *Biotechnol. Adv.* 2004, **22**, 505.

[21] P. Ugo, N. Pepe, L.M. Moretto, M. Battagliarin, *J. Electroanal. Chem.* 2003, **560**,51.

[22] V. P. Menon, C.R. Martin, *Anal. Chem.* 1995, **67**, 1920.

[23] S. Pozzi Mucelli, M. Zamuner, M. Tormen, G. Stanta, P. Ugo, *Biosens. Bioelectron.* 2008, **23,** 1900.

[24] M. Zamuner, S. Pozzi Mucelli, M. Tormen, G. Stanta, P. Ugo, *Eur. J. Nanomed.* 2008, **1**, 33.

[25] J. Tamarit-Lopez, S. Morais, R. Puchades, A. Maquieira, *Biosens. Bioelectron.* 2011, **26**, 2694.

[26] S. Morais, L.A. Tortajada-Genaro, T. Arnandis-Chover, R. Puchades, A. Maquieira, *Anal. Chem.* 2009, **81**, 5646.

[27] M. Henry, C. Dupont-Gillain, P. Bertrand, *Langmuir* 2003, **19**, 6271.

[28] R. L. Green, R.W. Scales, S.J. Kraus, *Appl. Microbiol.* 1974, **27**, 475.

[29] F. Bottari, P. Oliveri, P. Ugo, *Biosens. Bioelectron.* 2014, **52**, 403.

[30] M. Silvestrini, L. Fruk, L.M. Moretto, P. Ugo, *J. Nanosci. Nanotechnol.* 2015, **15**, 3437.

[31] J.F Ludvigsson, D.A Leffler, J.C. Bai, F. Biagi, A. Fasano, P.H.R. Green, M. Hadjivassiliou, K. Kaukinen, C.P. Kelly, J.N. Leonard, K.E.A. Lundin, J.A. Murray, D.S. Sanders, M.M. Walker, F. Zingone, C. Ciacci, *Gut* 2013, **62**, 43.

[32] J. C. Bai, M. Fried, G. R. Corazza, D. Schuppan, M. Farthing, C. Catassi, L. Greco, H. Cohen, C. Ciacci, R. Eliakim, A. Fasano, A. Gonzalez, J. H. Krabshuis, A. LeMair, *J. Clin. Gastroenterol.* 2013, **47**, 121.

[33] J. -H. Kim, E.M. Jeong, Y.-J. Jeong, W.J. Lee, J.S. Kang, I-G. Kim, Y. -il Hwang, *Immunol. Lett.* 2012, **147**, 18.

[34] D. H. Kaswala, G. Veeraraghavan, C.P. Kelly, D.A. Leffler, *Diseases* 2015, **3**, 86.

[35] E. M. Barbero, S.L. McNally, M.C. Donohue, M.F. Kagnoff, *BMC Gastroenterol.* 2014, **14**, 42.

[36] S. Guandalini, A. Assiri, *JAMA Pediatrics* 2014, **168**, 272.

[37] G. Lakos, G.L. Norman, M. Mahler, P. Martis, C. Bentow, D. Santora, A. Fasano, *J. Immunol. Res.* 2014, **192**, 1.

[38] S. V. Kergaravat, L. Beltramino, N. Garnero, L. Trotta, M. Wagener, S.N. Fabiano, M.I. Pividori, S.R. Hernandez, *Anal. Chim. Acta* 2013, **798,** 89.

[39] S. Dulay, P. Lozano-Sánchez, E. Iwuoha, I. Katakis, C.K. O'Sullivan, *Biosens. Bioelectron.* 2011, **26**, 3852.

[40] K. A. Scherf, P. Koehler, H. Wieser, *Adv. Chem. Engineer. Sci.* 2015, **5**, 83.

[41] H. Sha, Y. Bai, S. Li, X. Wang, Y. Yin, *Am. J. Orthod. Dentofac.* 2014, **145**, 36.

[42] M.A.M. Rodrigo, Z. Heger, N. Cernei, A.M.J. Jinemez, O. Zitka, V. Adam, R. Kizek, *Int. J. Electrochem. Sci.* 2014, **9**, 3449.

[43] S. Husby, S. Koletzko, I. R. Korponay-Szabo, *J. Pediatr. Gastr. Nutr.* 2012, **54**, 136.

[44] V. Baldas, A. Tommasini, C Trevisiol, I Berti, A Fasano, D Sblattero, A Bradbury, R Marzari, G Barillari, A Ventura, T Not, *Gut* 2000, **47,** 628.

[45] T. D. Pelkowski, A.J. Viera, *Am. Fam. Physician* 2014, 89, 99.

[46] I. Dahlbom, M. Olsson, N.K. Forooz, A.G. Sjoholm, L. Truedsson, T. Hansson, *Clin. Diagn. Lab. Immunol.* 2005, **12**, 254.

[47] A. Rostom, C. Dube, A. Cranney, N. Saloojee, R. Sy, C. Garritty, M. Sampson, L. Zhang, F. Yazdi, V. Mamaladze, I. Pan, J. Macneil, D. Mack, D. Patel, D. Moher, *Gastroenterology* 2005, **128**, S38.

[48] M.I. Pividori , A. Lermo, A. Bonanni, S. Alegret, M. del Valle, *Anal. Biochem.* 2009, **388**, 229.

[49] S. S. Ordonez, E. Fabregas, *Biosens. Bioelectron.* 2007, **22**, 965.

[50] Z. Wang, Y. Yang, J. Li, J. Gong, G. Shen, R. Yu, *Talanta* 2006, **69**, 686.

[51] C. -X. Lei, S.-Q. Hu, G.-L. Shen, R.-Q. Yu, *Talanta* 2003, **59**, 981.

[52] J. Zhou, C. Campbell, A. Heller, A. J. Bard, *Anal. Chem.* 2002, **74**, 4007.

[53] X. Ji, C.E. Banks, D.S. Silvester, A.J. Wain, R.G. Compton, *J. Phys. Chem. C* 2007, **111**, 1496.

[54] P. D. Astudillo, J. Tiburcio, F. J. Gonzalez, *J. Electroanal. Chem.* 2007, **604**, 57.

[55] Z.-M. Liu, Y. Yang, H. Wang, Y.-L. Liu, G.-L. Shen, R.-Q. Yu, *Sensor. Actuator. B* 2005, **106**, 394.

[56] S. Nawar, B. Huskinson, M. Aziz, *Mater. Res. Soc. Symp. Proc.* 2013, **1491**.

[57] C. Camacho, J. C. Matas, B. Chico, R. Cao, L. Gomez, B. K. Simpson, R. Villalonga, *Electroanalysis* 19, **2007**, 2538.

[58] P. Petrangolini, A. Alessandrini, P. Facci, *J. Phys. Chem. C* 2013, **117**, 17451.

[59] T. M. Alligrant, J. C. Hackett, J. C. Alvarez, *Electrochim. Acta* 2010, **55**, 6507.

[60] Y. Zhuo, W.-J. Yi, W.-B. Lian, R. Yuan, Y.-Q. Chai, A. Chen, C.-M. Hu, *Biosens. Bioelectron.* 2011, **26**, 2188.

[61] B. Brunetti, P. Ugo, L.M. Moretto, C.R. Martin, *J. Electroanal. Chem.* 2000, **491**, 166.

[62] P. Ugo, L.M. Moretto, S. Bellomi, V.P. Menon, C.R. Martin, *Anal. Chem.* **1996**, **68**, 4160.

[63] C. Amatore, J. M. Saveant, D. Tessier, *J. Electroanal. Chem.* 1983, **147**, 39.

[64] J. Guo, E. Lindner, *Anal. Chem.* 2009, **81**, 130.

[65] T. J. Davies, R.G. Compton, *J. Electroanal. Chem.* 2005, **585**, 63.

[66] X. -J. Huang, A.M. O'Mahony, R.G. Compton, *Small* 2009, **7**, 776.

[67] M. Ongaro, P. Ugo, *Anal. Bioanal. Chem.* **2013**, **405**, 3715.

[68] B. V. Chikkaveeraiah, A. A. Bhirde, N. Y. Morgan, H. S. Eden, X. Chen, *ACS Nano* 2012, **6**, 6546–6561.

[69] M. Giannetto, M. Mattarozzi, E. Umilta, A. Manfredi, S. Quaglia, M. Careri, *Biosens. Bioelectron.* 2014, **62**, 325.

[70] S.-D. Bolboaca, L. Jentschi, *Leonardo Journal of Science* 2006, **9**, 179.

[71] K.H. Zou, K. Tuncali, S.G. Silverman, *Radiology* 2003, 617.

[72] Stats Tutor, http://www.statstutor.ac.uk/resources/uploaded/spearmans.pdf.

[73] Stats Tutor, http://www.statstutor.ac.uk/resources/uploaded/pearsons.pdf.

Chapter 4

A sensitive electrochemiluminescence immunosensor for celiac disease diagnosis based on nanoelectrode ensembles

4.1 Introduction

Celiac disease (CD) is a gluten-dependent autoimmune disorder occurring in individuals carrying the human leucocyte antigen molecules DQ2/DQ8 [1,2]. It has recently been demonstrated that the prevalence increases over time by age: for instance, in Finland, the prevalence is 1.5 % in children, 2.2% in adults and 2.7% in the elderly [3]. Furthermore, the prevalence of CD increases to $10 - 20\%$ among patients with anemia, to 11% among insulin dependent diabetes mellitus patients, to 8% among first-degree relatives of CD patients, to 7% in children with isolate stature growth defect and to 5% among patients with autoimmune diseases [4,5]. The clinical conditions of CD vary from mild to severe, and some patients can be asymptomatic for years. Classical symptoms include gastrointestinal complaints (malabsorption, diarrhoea) but the extra-intestinal symptoms represent the large majority of the clinical features such as osteoporosis [6], *Dermatitis herpetiformis* [7], psychiatric and neurological disorders [8], arthritis [9] cardiac [10,11] and obstetric disorders [12]. The later the diagnosis of CD, the more likely the occurrence of serious illnesses and excess mortality [13]. Early diagnosis and treatment with gluten-free diet, reduces mortality and the prevalence of CD-associated disorders. Although definitive diagnosis of CD is still based on histological changes in small intestinal mucosa whose detection requires biopsy, serological test for CD screening based on detection of anti-tissue transglutaminase antibodies (anti-tTG) are less invasive [14]. Given the high prevalence of the CD and the implications of a late detection, several simple, cheap and rapid immunoassays were developed as a first step towards speeding up CD diagnosis in the physician's office [15,16]. Of interest, these rapid tests might greatly help the physician to make a preliminary diagnosis of CD in resource-constrained countries where diarrheal disease and malnutrition are common [17]. In this context, making diagnosis of CD and enforcing a gluten-free diet would make a significant

contribution to reduce morbidity and mortality, particularly when the CD-diagnosis is not yet considered [18].

Immunoglobulin A (anti-tTG IgA) is the isotype typically determined as target analyte for serological CD screening [19,20]. However, IgA-deficient CD patients cannot be identified by this analysis [21]. Moreover, focusing on CD diagnosis in very young children for whom biopsy is not an eligible test, it has been found that only 87% of CD patients younger than 2 years of age showed high serum levels of IgA anti-tTG *vs* 96% for celiac children older than 2 years [22]. On the other hand, serological diagnosis based on IgG assays at present do not look as valid alternatives for general screening because IgG based assays are claimed to be poorer in sensitivity than IgA based analysis [23]. From these bases, it is evident that the development of an IgG-based diagnostic method with improved sensitivity and specificity is highly required.

Many trials (using different biomarkers of CD) have been made to develop variety of electrochemical methods [24-29] but, so far, no confirmatory serological method has been adopted for practical use. Accordingly, we propose herein a novel anti-tTG IgG immunosensor utilizing an original ECL detection strategy based on nanoelectrode ensembles as electrochemical transducer.

Given the inherent analytical performances of ECL technique, it has recently attracted enormous attention in bioanalysis. Indeed, since no excitation light source is required to induce the ECL, the background signal is extremely low and thus the technique is highly sensitive at physiological pH with low detection limits [30-34]. Moreover, ECL provides additional advantages such as wide linear dynamic range, selectivity and stability of the luminophore. In addition, it is relatively easy to conjugate the luminescent species to biomolecules such as antibody, DNA or RNA [35-40]. Therefore, the luminophore is classically used as an ECL label in bioassays [41,42]. The model system involving $Ru(bpy)_3^{2+}$ as the light emitting species and TPrA as the co-reactant forms the basis of a large number of commercially available bead-based ECL immunoassays, such as for cardiac and infectious diseases, thyroid, tumor markers, *etc* [36,43-51]. The excellent sensitivity of such immunoassays is due to the fact that ruthenium centers located at micrometric distances from the electrode generate ECL [52,53]. Indeed, in this case, only the co-reactant TPrA is oxidized at the electrode and the resulting radicals, $TPrA^{\bullet+}$ and $TPrA^{\bullet}$, diffuse over short distances and react with the luminophore to generate its excited

state [52]. So this mechanistic path does not require the direct oxidation of Ru(bpy)$_3$$^{2+}$ at the electrode surface to generate *in fine* the ECL emission. In addition, it occurs at a potential ~300 mV lower than for the routes involving oxidation of Ru(bpy)$_3$$^{2+}$. Applying such lower potentials might prevent problems including; (i) interference from side reactions particularly in complex matrix of real samples (e.g. blood, serum), (ii) ECL background arising from the reaction between Ru(bpy)$_3$$^{2+}$ and hydroxide [54], (iii) damages on susceptible proteins and oligonucleotides [55], and (iv) oxide layer formation on Au or other metal electrodes resulting in poor analytical reproducibility.

NEEs are random arrays of nanoscopic electrodes typically prepared by the electroless deposition of gold within the nanopores of track-etched PC membranes [56-59]. The nature of the faradaic current depends on the distance between the nanodisks, on the solution viscosity and on the timescale of the experiment [60-62]. When commercial track-etched membranes are used, the obtained NEEs operate in the total overlap diffusion regime [62,63] which means that electroactive species diffuse *via* semi-infinite planar diffusion with respect to all the surface of the NEE, i.e. nanoelectrodes and insulator between them. Recently, the properties of NEEs have been exploited to develop electrochemical biosensors [64] in which relatively high amounts of bioreceptors were immobilized directly on the PC of the NEEs. The integration between the biorecognition event and the electrochemical acquisition of the signal is ensured by the presence in the electrolytic solution of redox mediators; these can diffuse all over the geometric area of the NEE and shuttle electrons to redox labels bound to the biorecognition layer [64]. This approach has been applied to develop sensitive affinity biosensors suitable to detect the human epidermal growth factor receptor HER2 overexpressed in breast cancer cells [65], DNA sequences for virus genotyping [66,67], ligand proteins of interest for cultural heritage diagnostics [68] and enzyme based glucose sensing [69].

In the present work, we combine for the first time the remarkable properties of NEEs with the excellent detection capability of ECL in order to develop a novel sensing method based on anti-tTG IgG determination, for CD diagnosis in human serum. A major originality of the current approach is to separate physically the location of the initial electrochemical reaction at the Au NEEs (i.e. oxidation of the co-reactant) from the ECL emitting region where the luminophore label is immobilized on the PC substrate. To this aim, the capturing agent tTG is at first bound onto the PC of a NEE so that, when incubated with the sample, it reacts with the target analyte,

namely anti-tTG IgG antibody (Scheme 4.1). The biorecognition chain is continued by coupling the captured anti-tTG antibody with a biotinylated secondary anti-IgG antibody. A streptavidin $Ru(bpy)_3^{2+}$ derivative (SA-Ru) is then used as the ECL label, which binds to the PC surface only in case of positive analytical response. Finally, the ECL emission is generated by using a PBS solution containing the sacrificial TPrA co-reactant and by applying a suitable electrochemical potential. Thanks to the customized architecture of the platform, the TPrA co-reactant is oxidized at the nanoelectrodes and the resulting radicals diffuse all over the geometric area of the NEE to reach the $Ru(bpy)_3^{2+}$ label on the PC to produce ECL. With NEEs, the first advantage is that high local fluxes of reactive radicals are generated due to the size of the electrode. The second advantage is that the radicals are produced in the immediate vicinity of the ECL labels which are immobilized on the PC, so that they can efficiently generate the ECL signal. Finally, they offer the opportunity to miniaturize such an analytical platform.

Scheme 4.1 Scheme showing the design of the immunosensor (not drawn to scale). The PC surface is first modified with the capture protein, tTG. The assay is performed by incubating it with a sample containing the target (i.e. anti-tTG antibody) and then in a solution of a biotinylated detection antibody. The final step consists in attaching the ECL label by exposing the immunosensor to a solution containing a streptavidin-modified $Ru(bpy)_3^{2+}$ complex (SA-Ru). Oxidation of TPrA occurs at each Au nanoelectrode of the NEEs and the resulting radicals, $TPrA^{\bullet+}$ and $TPrA^{\bullet}$, diffuse over short distances and react with the luminophore label attached to the PC to generate the ECL emission. Note that the different elements are not drawn to scale.

4.2 Experimental

4.2.1 Materials

In order to record the ECL as a function of the applied potential, an experimental set up composed of an Autolab PGSTAT30 potentiostat, a Hamamatsu photomultiplier tube (PMT), KEITHLEY 6485 Picoammeter, a high voltage power supply model C9525 (Hamamatsu Photonics) and a three electrode electrochemical cell properly aligned with the PMT are used (Figure 4.1A). All these components of the set up are simultaneously run by PGES software. The PMT and the electrochemical cell (Figure 4.1B) are housed in a dark box to prevent external background light.

Figure 4.1 Photos of **A**) ECL measuring instrumental set up, **B**) alignment of the electrochemical cell and the PMT.

The ECL triggering potential is applied in a cyclic voltammetric pattern in a PBS solution containing the co-reactant.

Morphological study was carried out using high resolution JOEL JSM-6700F field-emission scanning electron microscope (FE-SEM) instrumentation (Figure 4.2). The distribution, size, shape, and recession of Au nanodisks as well as the extent of pores filling are examined with a magnification of up to 250,000X (some images are shown in Figure 4.3).

Figure 4.2 Photograph of a Field Emission Scanning Electron Microscopy (FE-SEM) instrument.

All experiments were performed using an Ag/AgCl reference electrode and a platinum wire as counter electrode. Bis(2,2'-bipyridine)-4'-methyl-4-carboxybipyridine-ruthenium N-succinimidyl ester bis(hexafluorophosphate) and Streptavidin from *Streptomyces avidinii*, Tween 20, bovine serum albumin and biotinylated goat anti-human secondary antibody were purchased from Sigma. Tissue transglutaminase (tTG) was prepared as previously described [1]. Monoclonal mouse anti-tTG (CUB 7402) was purchased from BioOptica and biotinylated goat anti-mouse secondary antibody from Dako. Serum samples were obtained from 5 biopsy proven celiac children tested positive only for IgA anti-tTG (9777, 9782, 9784, 9809, 9830) and from 2

children without autoimmunity and gastrointestinal disorders tested negative for both IgA and IgG anti-tTG (9463, 9597). All patients were diagnosed at the Pediatric Hospital "Burlo Garofolo" (Trieste, Italy). Gold electroless plating solution (Oromerse Part B, Technic Inc.) and hydrophilic track-etched PC filter membranes (47 mm diameter, 6 μm thickness) with a nominal pore diameter of 30 nm, pore density 6×10^8 pores/cm^2 were used for manufacturing NEEs. All other reagents were of analytical grade.

4.2.2 Methods

Modification of streptavidin with Ru(bpy)$_3^{2+}$ complex (SA-Ru)

The modification was done as reported by Deiss *et al* [38] with some modifications. Briefly, 1 mg of streptavidin was dissolved in 1 mL of Milli-Q water. Then 100 μL of this solution was added in to 810 μL of water and 90 μL of 1X PBS pH 7.4 and mixed with 1 mg of Bis(2,2′-bipyridine)-4′-methyl-4-carboxybipyridine-ruthenium N-succinimidyl esterbis(hexa-fluorophosphate), which was dissolved in 100 μL of dried DMSO. The mixture was kept at 4 °C on continuous stirring for 4h. Then it was purified by dialysis in PBS (1X) using Slide-A-Lyzer Dialysis Cassettes 10k molecular weight cut off from Thermo Scientific for about 16h. The Ru-SA complex was stored at +4 °C until used.

Fabrication of the NEEs

The Au NEEs were prepared by electroless deposition of gold in track-etched PC filter membranes [56,57,59,70], with average pores density of 6×10^8 per cm^2 and nominal pore diameter of 30 nm (details are given in Chapter 1). During the electroless deposition of gold from a solution, each pore of the PC membrane was filled with a metal nanowire whose head is exposed to the electrolyte solution. The overall geometric diameters of all the NEEs used in this experiment were 3 mm and hence are composed of millions of randomly spaced gold nanodisks (average diameter of 40 ± 10 nm as determined by the FE-SEM). The membrane bearing the nanodisks was assembled in to electrodes of suitable geometry and size.

Preparation of the immunoassay and analytical protocol

After washing the NEE thoroughly with Milli-Q water, 10 μL 10 μg mL^{-1} tTG solution was dropped on the NEE and incubated for 2 h at 25°C. The tTG-NEE was subsequently blocked

with 1 % BSA (in 1X PBS) for 30 min followed by incubation with 10 µL standard solution of anti-tTG or serum sample in 1X PBS pH 7.4 for 60 min. After washing with 1X PBS pH 7.4 containing 0.05 % Tween 20, the captured primary antibody was coupled with biotinylated goat anti-mouse or anti-human (in cases of serum samples analysis) IgG secondary antibody for 60 min. It was further incubated for 30 min at +4 °C with SA-Ru solution. In all the procedures, 1X PBS impregnated filter paper was put in the incubation container and sealed to avoid evaporation of the solution; incubations were made at 25°C except the last step. All incubation steps were followed by thorough rinsing with the 1X buffer solution. Finally, the biosensor was dipped in a homemade three-electrode electrochemical cell containing 0.1 M TPA in 0.1 M PBS pH 7.4 previously deaerated with nitrogen for 20 minutes. ECL and cyclic voltammograms were recorded concurrently at a scan rate of 100 mV s^{-1}. The ECL intensity was measured using a PMT put in a dark at a bias voltage of -750 V. In addition to the PMT, the experimental setup comprises of a potentiostat, picoammeter and high voltage supply. Maximum care was taken while aligning the sensor surface with the PMT.

Fluoroenzyme immunoassay for anti-tissue transglutaminase antibodies was performed according to manufacturer's instructions (Elia^{TM} Celikey, Phadia 250).

4.3 Results and Discussion

4.3.1 Characterization of the nanoelectrode ensembles

Prior to the immunosensor construction, the fabricated NEEs were evaluated for electrochemical performance, surface morphology and chemical composition.

The FE-SEM images of a typical NEE taken before functionalizing with the capture protein, tTG, are shown in Figure 4.3.
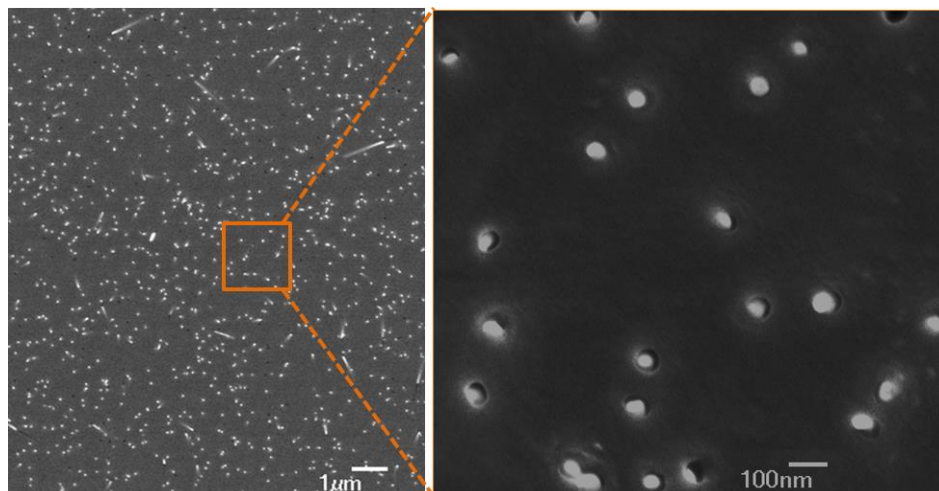
Figure 4.3 Field emission scanning electron microscopy images of a bare gold-NEE at two magnifications.
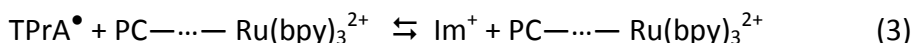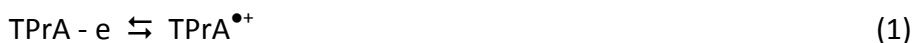
The conductive Au nanoelectrodes can clearly be seen as bright disks surrounded by the insulating PC surface (black part). The pores of the template are filled by electroless deposition of gold producing about 6 μm long nanowires whose upper ends emerge on the surface of the template with the shape of nanodisks of about 40 ± 10 nm in diameter. The distance between the nanoelectrodes is rather variable, ranging between less than 100 and 400 nm. The density of nanoelectrodes measured from these images is 5×10^8 electrodes cm^{-2}. All these morphological data substantially match with those presented previously by Ugo *et al* [71], confirming that the diameter of the nanodisk electrodes is slightly higher than the diameter of the pores declared by the supplier of the track-etched filter membrane (namely, 30 nm) with an electrode density substantially matching with the declared pore density (5×10^8 *vs* 6×10^8, respectively). From the high resolution FE-SEM image, few empty and partially Au filled pores were identified. Some of the nanodisks are slightly recessed below the upper surface of the PC.

In addition to the morphological and chemical composition analysis (as shown in Chapter 2), all the NEEs were electrochemically evaluated before functionalizing with biomolecules.

4.3.2 ECL detection based on immobilized labels and diffusing TPrA radicals

In the present work, an original sensing strategy based on the spatial separation between the electrochemical reaction and the biorecognition event is reported. Considering the global ECL

process, this means that the initial electron-transfer reactions occuring at the Au nanodisks are separated from the final step where light is emitted at the level of the non-conductive PC surface selectively modified by the biomolecules. Such a sensing approach does not require a direct electron transfer between the ECL label and the electrode surface and hence, it is completely based on the so-called "revisited route" of ECL emission [52,72]. In this mechanistic path, only the model co-reactant TPrA is oxidized at the electrode and the resulting radicals, $TPrA^{\bullet+}$ and $TPrA^{\bullet}$, play the central role in the ECL process:

$$TPrA - e \leftrightarrows TPrA^{\bullet+} \tag{1}$$

$$TPrA^{\bullet+} \leftrightarrows TPrA^{\bullet} + H^{+} \tag{2}$$

$$TPrA^{\bullet} + PC\text{—}\cdots\text{—}Ru(bpy)_3^{2+} \leftrightarrows Im^{+} + PC\text{—}\cdots\text{—}Ru(bpy)_3^{2+} \tag{3}$$

$$TPrA^{\bullet+} + PC\text{—}\cdots\text{—}Ru(bpy)_3^{2+} \leftrightarrows TPrA + PC\text{—}\cdots\text{—}Ru(bpy)_3^{2+} \tag{4}$$

$$PC\text{—}\cdots\text{—}Ru(bpy)_3^{2+} \rightarrow PC\text{—}\cdots\text{—}Ru(bpy)_3^{2+} + hv_{ECL} \tag{5}$$

where Im^{+} is the iminium product and $PC\text{—}\cdots\text{—}Ru(bpy)_3^{2+}$ represents the ruthenium label attached to the PC surface *via* the biorecognition chain described on Scheme 4.1.

The radical cation $TPrA^{\bullet+}$ is formed at the surface of the Au nanodisks by TPrA electro-oxidation (*reaction 1*). While diffusing, the radical cation undergoes deprotonation reaction to produce the strong reducing radical $TPrA^{\bullet}$ (*reaction 2*), which reduces the immobilized $Ru(bpy)_3^{2+}$ label to $Ru(bpy)_3^{2+}$ (*reaction 3*). This process is followed by the one-electron oxidation of $Ru(bpy)_3^{2+}$ by the remaining $TPrA^{\bullet+}$ radical cations to generate the excited state $Ru(bpy)_3^{2+}$ on the PC (*reaction 4*). Finally, $Ru(bpy)_3^{2+}$ relaxes to the ground state by photon (ECL) emission (*reaction 5*) [43,63,64].

It is worth mentioning that the factors which affect the life-time of the radical cation, such as the pH of the electrolyte solution [74,75], should be critically controlled to ensure optimum proportion of $TPrA^{\bullet+}$ and $TPrA^{\bullet}$ at the site of emission. Indeed, the unstable nature of the radical cation is one of the factors that determine the maximum distance from the electrode at which ECL emission can occur. In strongly alkaline solutions, deprotonation of $TPrA^{\bullet+}$ is enhanced resulting in shortage of the cation at the site of emission. Based on the 0.2 millisecond half-life (in neutral pH) of the radical cation reported in the literature [72], it can diffuse up to 6 μm from the site of formation [52,72] which is a distance largely exceeding the maximum distance (i.e.

200 nm) of the luminophore label from the nanodisks (i.e. the maximum half-distance between two neighboring nanoelectrodes) in our sensor. This means that both radicals generated by reactions (1) and (2) can live long enough to diffuse to the ruthenium label where reactions (3)-(5) take place on the PC surface (see Scheme 4.1).

4.3.3 ECL immunoassay platform

The ECL platform consists of an ensemble of nanoelectrodes delimited by an insulating PC film which is modified with a capture tTG protein. The assay was performed by incubating the modified NEEs with a sample containing the target anti-tTG IgG antibody and then in a solution of a biotinylated detection antibody. Finally, the streptavidin-modified ECL label is attached to this secondary antibody found on the PC surface. The $Ru(bpy)_3^{2+}$ label should bind only to the PC where the capture tTG protein is present.

The ECL triggering potential is applied in a cyclic voltammetric pattern in a PBS solution containing the co-reactant. Figure 4.4 shows the cyclic voltammetric and ECL responses of the new immunosensor recorded simultaneously in the presence of the TPrA as co-reactant. The PMT detected a single, intense and a well-resolved ECL signal at an applied potential of 0.87 V *vs* Ag/AgCl (Figure 4.4).
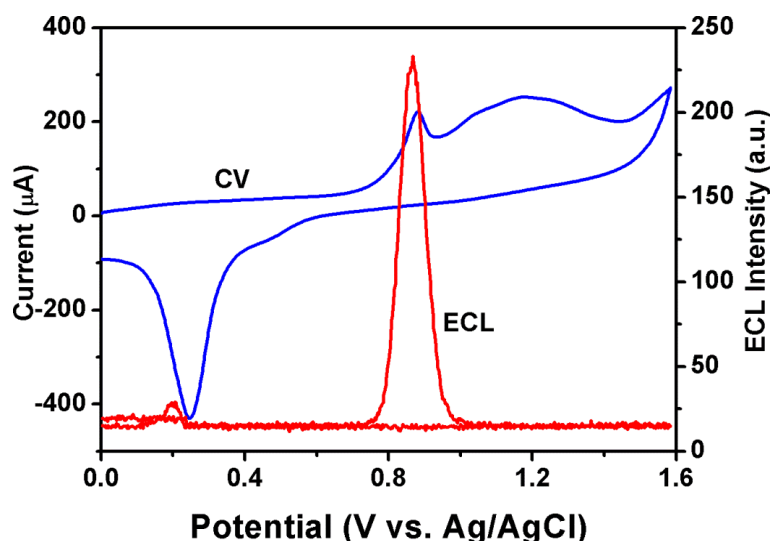
Figure 4.4 Cyclic voltammogram (blue curve) and the corresponding ECL intensity (red curve) of the anti-tTG immunosensor obtained in a deoxygenated PBS (pH 7.4) containing 0.1 M TPrA. Scan rate of 100 mV s^{-1}.

The anodic portion of the voltammetric curve is characterized by an oxidation peak at approximately 0.88 V *vs* Ag/AgCl, followed by a broad signal at about 1.2 V. During the backward scan, a cathodic peak is detected at about 0.25 V. The broad signal at 1.2 V is most likely due to the formation of Au-oxides on the surface of the nanoelectrodes, this oxide layer being reduced at 0.25 V in the backward scan. This agrees with previous literature findings [62] which demonstrated the Au-oxides formation is anticipated at the nanoelectrodes' surface with respect to bulk gold. The voltammetric peak at 0.88 V is attributed to the electrochemical oxidation of TPrA, as confirmed by differential pulse voltammetry (DPV) experiments (Figure 4.5).
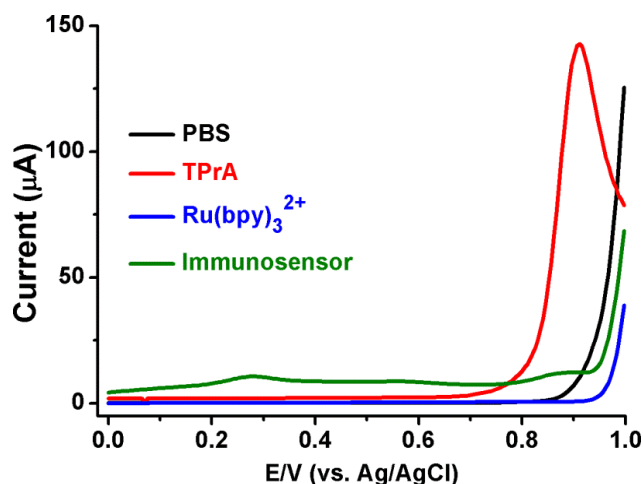
Figure 4.5 Overlay of DPVs of a bare NEE in PBS only, after addition of TPrA or Ru(bpy)$_3^{2+}$ and the immunosensor in PBS. A strong peak at the ECL potential is observed in the presence of TPrA in the electrolyte solution. No sign of oxidation of Ru(bpy)$_3^{2+}$ is observed at around the emission potential (0.87 V).

DPV was preferred to cyclic voltammetry for these measurements since it provides both a better intensity and a better resolution to separate possibly overlapping peaks. DPVs recorded at a bare NEE and the immunosensor in PBS without adding TPrA did not show any noticeable peak close to the ECL potential of 0.87 V. However, peak currents associated to formation of surface oxides are recorded at higher oxidation potential at both the bare NEE and the immunosensor (Figure 4.6). The lower peak current intensity at the immunosensor (modified NEE) but higher capacitive current than at the bare NEE could be due to inhibition of the oxides formation by the adsorbed blocking protein (i.e. BSA) on the metallic surface of the NEE.
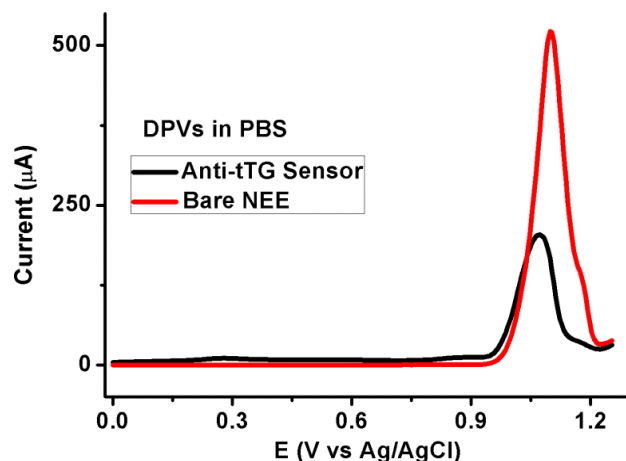
Figure 4.6 Differential Pulse Voltammograms (DPVs) recorded at bare NEE and at the immunosensor in PBS 7.4 in the absence of TPrA.

DPVs recorded at the bare NEEs dipped in different concentrations of $Ru(bpy)_3^{2+}$ but without TPrA did not produce any peak up to 1 V *vs* Ag/AgCl (Figure 4.7B). Data reported in Figure 4.7A indicate that a DPV peak at 0.88 V is clearly detected when a bare NEE is dipped in TPrA solution, and the peak amplitude increases with the TPrA concentration indicating that the ECL is induced by the oxidation of TPrA alone.
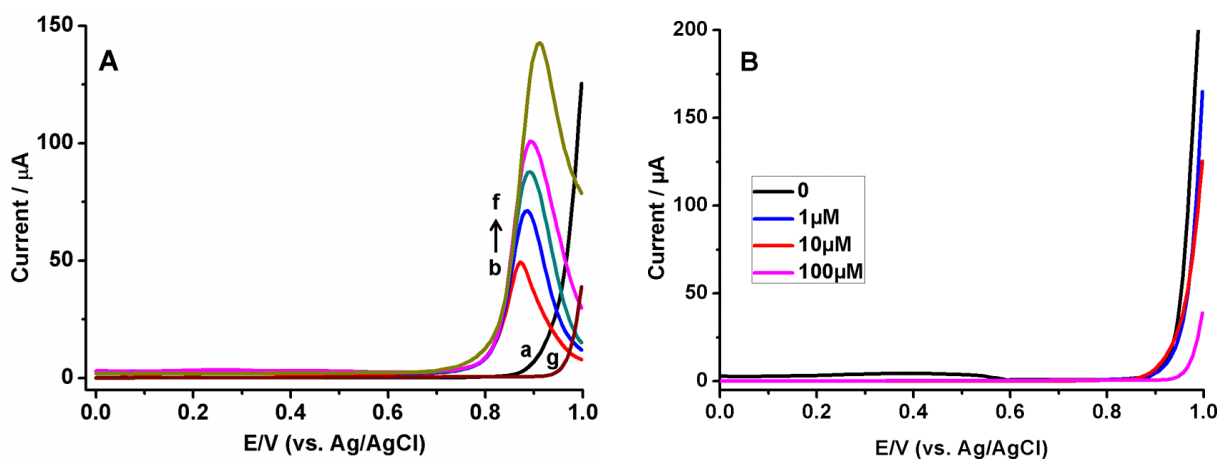
Figure 4.7 Differential pulse voltammograms (DPVs) recorded at bare NEE in PBS: **A)** containing 0, 1, 5, 10, 50, 100 mM (a-f) TPrA or (g) 100 µM $Ru(bpy)_3^{2+}$, and **B)** containing different concentrations of $Ru(bpy)_3^{2+}$.

In addition, voltammetric experiments (Figure 4.4) confirmed that the ruthenium complex is not oxidized on the Au nanodisks, even at the lower anodic potential (i.e. 0.88 V vs Ag/AgCl). As a whole, these results demonstrate that the ECL label is immobilized only on the PC surface.

It is noteworthy that ECL is detected at the potential where TPrA oxidation occurs, while no ECL signal is detected at the potential usually expected for $Ru(bpy)_3^{2+}$ oxidation (namely, 1.2 V vs Ag/AgCl), even after repetitive potential scanning. This evidences that the direct oxidation of $Ru(bpy)_3^{2+}$ at the surface of the Au nanodisks is not occurring since the ruthenium label is specifically linked to the antigen-antibodies chain immobilized on the PC of the NEEs.

Moreover, the central role of the TPrA oxidation in the present analytical strategy was also confirmed by comparing the voltammetric and ECL emission patterns observed when changing the $Ru(bpy)_3^{2+}$ concentration either when dissolved in solution (Figure 4.8A-C) or when bound onto the PC as a SA- $Ru(bpy)_3^{2+}$ label (Figure 4.8D-F). When $Ru(bpy)_3^{2+}$ is dissolved in solution (Figure 4.8A-C), two ECL peaks are recorded at around 0.88 V and 1.2 V. Both ECL signals are better resolved at lower concentrations of ruthenium complex (e.g. 0.5 µM), keeping the TPrA concentration constant at 0.1 M. Such a behavior was already reported in previous works [53,55,72,76] and it agrees with the occurrence of two separated ECL emission processes: one related to TPrA oxidation at 0.88 V (i.e. the "revisited route") and the other due to $Ru(bpy)_3^{2+}$ oxidation at 1.2 V [72] (namely the "catalytic route"). It is worth stressing that the ECL intensity at 1.2 V scales with the concentration $Ru(bpy)_3^{2+}$ in the electrolyte solution. In the CVs in Figure 3A-C, the peak relevant to the formation of Au oxides on the surface of the NEEs, is located just before the $Ru(bpy)_3^{2+}$ oxidation peak, while the reduction of these oxides (return scan) is detected at about 0.45 V, while in Figure 3 D-F (immunosensor) this peak is detected at 0.25 V. Such a difference is related to the different anodic limit adopted for the scans 3A-C and 3D-F, namely 1.25 V vs 1.6 V, respectively. A higher limit corresponds indeed to the formation of a more compact layer of Au-oxides, which is more difficult to re-reduce.

In the case of the immunoassay (Figure 4.8D-F), the amount of ECL label bound on the PC surface was tuned by changing the concentration of anti-tTG in the incubation solution. Higher anti-tTG concentrations favor more bounded secondary antibody and, consequently, more SA-$Ru(bpy)_3^{2+}$ finally attached on the PC. In this case, only one ECL emission peak is detected at 0.88 V, its maximum intensity depending on the amount of anti-tTG (i.e. $Ru(bpy)_3^{2+}$ label). As

expected, the voltammetric signals remain practically unchanged from Figure 4.8D-F because TPrA oxidation and Au-oxides formation occur whatever the amount of label immobilized on the PC. Only for the highly amplified ECL signals in Figure 3D, a very small ECL emission was detected in proximity to the $Ru(bpy)_3^{2+}$ oxidation potential (1.28 V), with an ECL peak emission that is not higher than 1% of the peak at 0.87 V. This confirms the negligible effect of non-specific adsorption of eventual traces of the luminophore on the NEE.
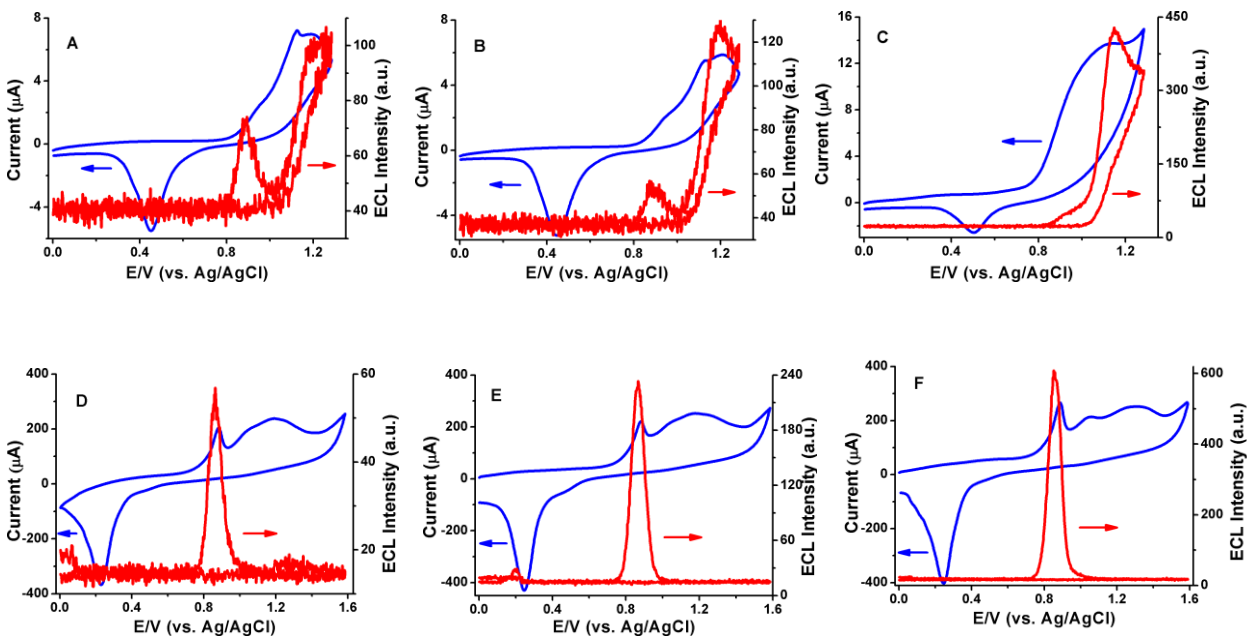
Figure 4.8 Effect of the amount of luminophore either dissolved in solution (curves **A-C**) or immobilized on PC (curves **D-F**) on the voltammetric (blue curves) and ECL responses (red curves) in 0.1 M PBS pH 7.4 solution containing 0.1 M TPrA. **A-C**) Signals recorded at bare NEE after adding **A**) 0.5, **B**) 1.0, and **C**) 10 µM $Ru(bpy)_3^{2+}$ in the solution. **D-F**) Signals recorded with the immunosensor incubated with **D**) 0.5, **E**) 1, and **F**) 10 µg mL^{-1} anti-tTG antibodies.

Moreover, no clear ECL emission was obtained at the $Ru(bpy)_3^{2+}$ oxidation potential. In the same way, the complete absence of the ECL at the oxidation potential of ruthenium (II) is an additional evidence for the absence of any non-specific adsorption of the luminophore on the NEEs and any leakage from the PC surface during the experiment. This indicates that the biologicals and then the luminophore label are selectively and strongly immobilized on the PC portion of the NEEs. If there were luminophore molecules non-specifically adsorbed on the Au

nanodisks, the luminophore can undergoes direct electro-oxidation eventually emitting ECL at around 1.2 V *vs* Ag/AgCl.

An important question that can be raised at this point is, because the Au nanodisks are surrounded by the PC host template, at least weak ECL is expected at 1.2V resulting from the luminophores that are attached to the edge of the PC adjacent to the Au disks. Although this requires further studies, for NEEs where the gaps between the nanodisks and the template are effectively thermos-sealed, the possible reasons could be: i) the nature of the PC adjacent to the nanodisks might have changed during the track-etching process, ii) the nanodisks might be recessed so that the distance from the luminophore is more than the electron tunneling distance, or iii) thick layer of protein might have formed causing a further increase in the net distance between the luminophore label and the electrochemically active Au surface.

To further confirm the selective immobilization of the biomolecules on the PC part of the NEEs without non-specific adsorption on the Au surface, the procedure of the immunosensor development was repeated using a 3 mm electrode prepared from gold deposited PC membrane without peeling off the Au layer from both faces. The electrode behaves like a conventional gold electrode. In this experiment no significant ECL was detected indicating that non-specific adsorption on the Au surface is unidentified.

In addition to TPrA, the performance of the NEE based immunosensor was tested using DBAE as co-reactant. A similar ECL emission profile was generated at the oxidation potential of the co-reactant but, only 20 mM of DBAE generated about the same ECL intensity as 100 mM TPrA which is in agreement with previous literature reports (see Figure 4.9).
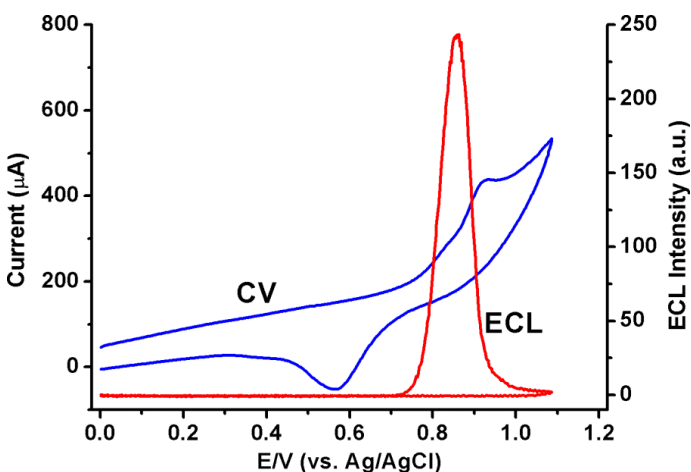

Figure 4.9 Cyclic voltammogram (blue curve) and the corresponding ECL intensity (red curve) of the anti-tTG immunosensor obtained in deoxygenated PBS (pH 7.4) containing 0.02 M DBAE. Scan rate of 100 mV s^{-1}.

However, due to the reason that TPrA is the most widely used co-reactant including in commercial diagnostic devices, further experiments were carried out using TPrA co-reactant.

In order for experimental results involving biomolecules to be valid, negative (in the absence of the biological of interest) and positive (with confirmed presence of the biological of interest) control experiments need to be conducted and results should be consistent. Therefore, in this work, the negative control experiments were performed by measuring the ECL at bare NEEs and with the immunosensor incubated with the secondary antibody and the SA- $Ru(bpy)_3^{2+}$ complex, but in the absence of the monoclonal mouse anti-tTG antibody (Figure 4.10B). ECL intensity comparable to the background level of the immunosensor is recorded in the former case. In the later situation, the lack of any quantifiable ECL signal indicates the absence of non-specific binding of the secondary antibody and/or SA- $Ru(bpy)_3^{2+}$ label. Both experiments confirm that when the anti-tTG target is absent, no $Ru(bpy)_3^{2+}$ label is bound onto the NEEs and no ECL is generated. On the contrary, the CVs recorded at the controls and the immunosensor are similar as displayed in Figure 4.10A. Unlike the DPV in Figure 4.6 which has shown significant peak current intensity difference between the bare NEE and the immunosensor, the CVs of the two electrodes are comparable. This could mainly be attributed to the presence of TPrA in the electrolyte solution.
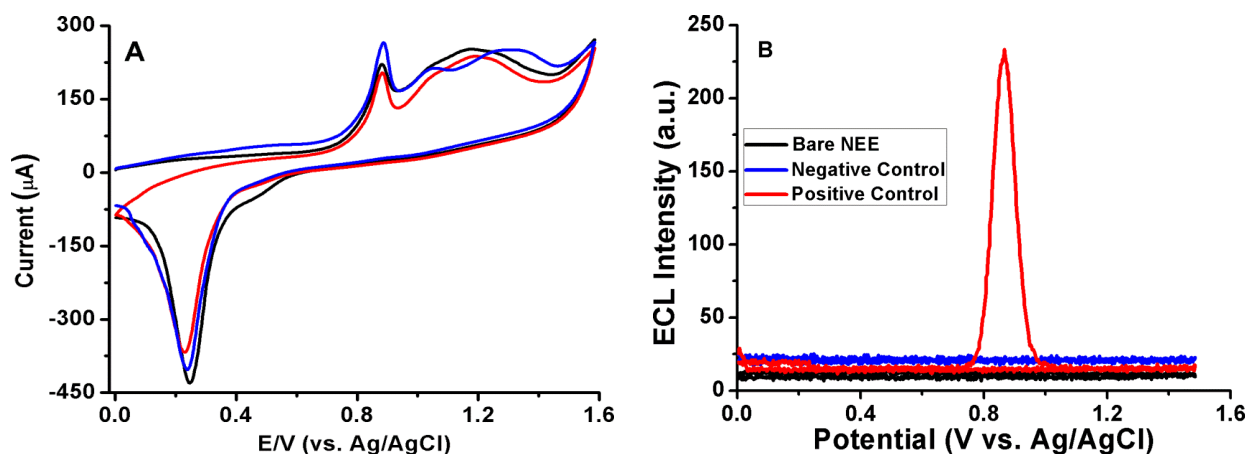

Figure 4.10 CVs (**A**) and the corresponding ECL curves (**B**) of bare NEEs (black curve), of the immunoassay recorded without (negative control - blue curve) and with (red curve) the incubation step in presence of the anti-tTG antibody in a PBS solution (pH 7.4) containing 0.1 M TPrA. Scan rate of 100 mV s^{-1}.

The fact that ECL emission occurs at an applied potential of 0.88 V, instead of 1.2 V as in the usual ECL assays, leads to several analytical advantages. First, it significantly reduces possible interferences from side reactions while dealing with complex samples containing oxidizable interferences. Next, it may reduce the ECL background arising from the reaction between $Ru(bpy)_3^{2+}$ and hydroxide in aqueous systems [54]. Third, concerning the applicability of such biosensors, it may minimize electrochemical damage on sensitive biomolecules and oligonucleotide sequences [54]. Finally, it reduces oxide layer formation on Au or Pt electrode surfaces. The electrochemical performances of the NEEs may be affected by the oxides layer formation on the Au nanodisks. As reported in Figure 4.11A and B, the immunosensor offered better ECL signals reproducibility when the potential was reversed from 1.0 V than reversing from 1.6 V. The ECL signals of the first and second scans are not shown in Figure 4.11, because, most experiments of this work, provided representative ECL signals after the second scan. When the potential was reversed at 1.6 V (Figure 4.11A), the percentage decrease of ECL between the 3rd and 6th measurement was about 28 %, but, when the scan was reversed from 1.0 V the decrease lowered to about 5 % (Figure 4.11B). At the 10th cycle, the ECL signal intensity was further lowered (with respect to the first cycle) by about 84 and 16 %, respectively.
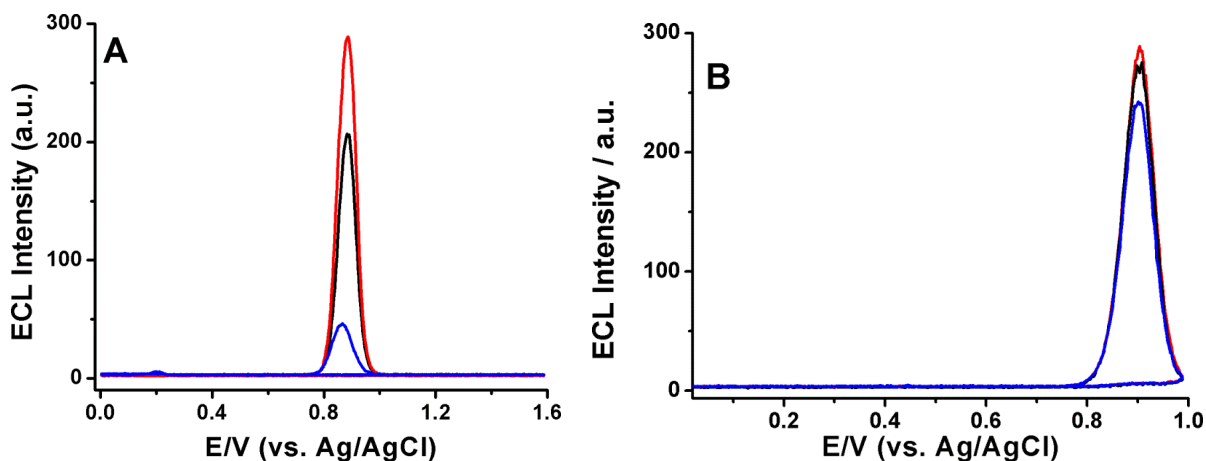

Figure 4.11 Overlays of the 3rd (red curves), 6th (black curves) and 10th (blue curves) ECL curves of repetitive measurements at the immunosensor in PBS containing 0.1 M TPrA. They display the effect of scan reversing potential, 1.6 V (**A**) and 1.0 V (**B**), on the stability of the ECL signal.

4.3.4 ECL imaging

Besides the quantification of ECL intensity using PMT, the emission can be clearly imaged using an EM-CCD camera. The ECL images of unmodified bare NEE and an immunosensor constructed of 100 ng mL^{-1} at an applied potential of +0.9 V are shown in Figure 4.12. Luminescence from scattered spots was captured on the surface of the immunosensor; however, no detectable emission was imaged from the surface of the clean bare NEE. Given the limited spatial resolution capability of classic microscopy, we are unable to distinguish if there is any ECL emission coming from non-specific binding of the luminophore on the Au nanodisks.
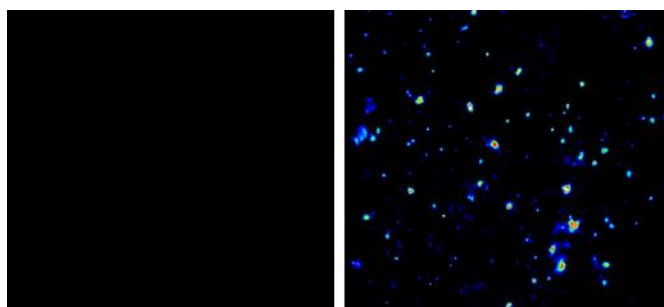
Figure 4.12 ECL images of a clean bare Au NEE before functionalization (left) and the anti-tTG IgG immunosensor in deoxygenated PBS (pH 7.4) containing 0.1 M TPrA. The experimental parameters are imaging potential 0.9 V and exposure time of 6 seconds.

4.3.5 Analytical performance and application to human serum

Since standard human anti-tTG antibody is unavailable in the market, the performance of the developed ECL-based immunosensor was initially evaluated using serial dilutions of standard mouse anti-tTG IgG antibody. The ECL responses of a blank and anti-tTG concentrations ranging from 1 ng mL^{-1} to 10 µg mL^{-1} are shown in Figure 4.13A. The calibration plot in Figure 4.13B shows that the logarithm of the ECL peak intensity increases linearly with the logarithm of the anti-tTG concentration, (correlation coefficient (R^2) = 0.995), over a wide dynamic range (10^{-9} to 10^{-5} g mL^{-1} anti-tTG).
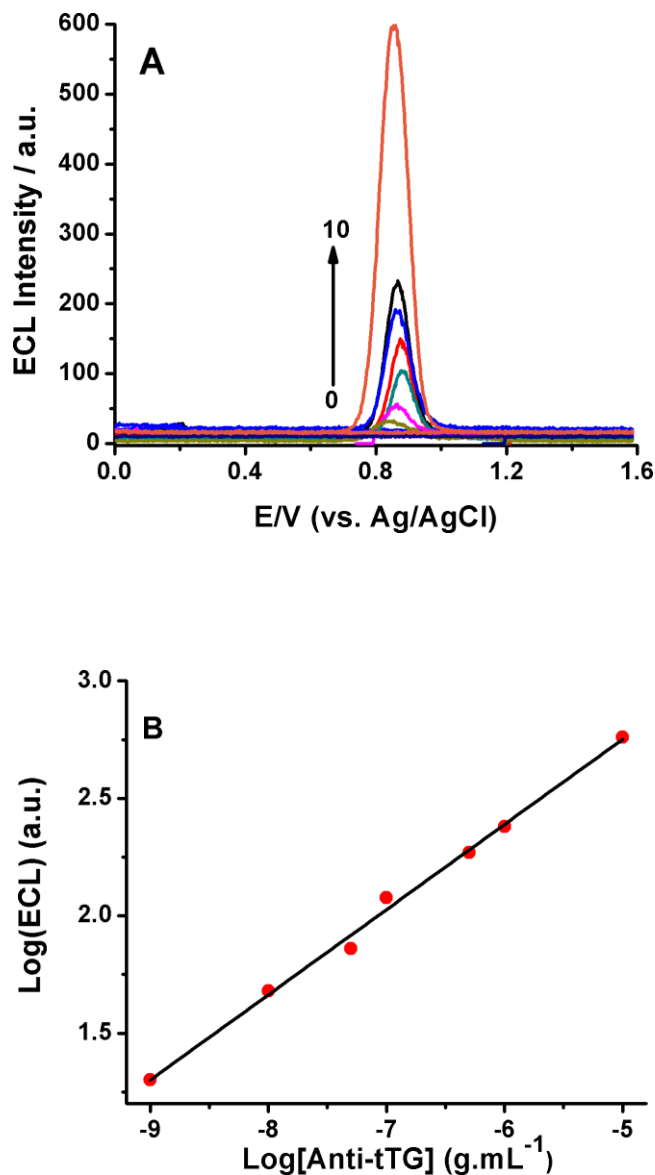
Figure 4.13 A) Relationship between ECL intensity and the concentration of anti-tTG antibody. The arrow indicates increasing concentrations of this target antibody: 0.00, 0.001, 0.01, 0.05, 0.1, 0.5, 1.0 and 10.0 μg mL^{-1}. **B**) Log-log plot of ECL signal output as a function of the concentration of anti-tTG captured on the NEE platform (n = 3). Same experimental conditions as in Figure 4.4.

A linear plot (with R^2 = 0.976) is also obtained for the direct dependence of the ECL intensity *vs.* anti-tTG concentration, in the range 1 to 100 ng mL^{-1} as shown in Figure 4.14.
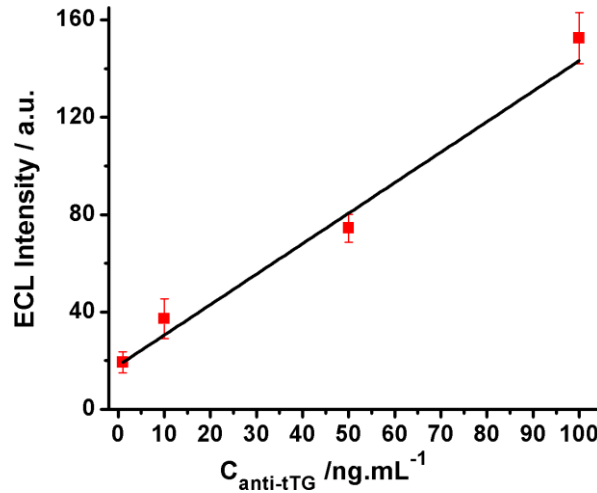
Figure 4.14 Direct dependence of ECL intensity on low concentrations of analyte.

Each analysis was performed with a different NEE which probably binds different amounts of proteins; a slight difference in the surface state of functionalized NEEs [76] could be the cause of the very slight shift in the potential at which the maximum ECL emission is detected (see Figure 4.13A). Indeed, data in Figure 4.13B refer to the ECL intensity measured at the potential of maximum emission. Concerning the reproducibility of the ECL maximum intensity, we conducted measurements repeated on four different NEEs all incubated in 1 ng mL^{-1} anti-tTG solution, which provided a relative standard deviation of 3.35, confirming a satisfactory precision. A limit of detection (LOD) of 470 pg mL^{-1} was calculated by using the equation LOD = $3\sigma_b/m$, where σ_b is the blank standard deviation (background noise) and m is the sensitivity (slope) of the linear calibration plot of ECL intensity *vs* [anti-tTG] [77].

The performances of the proposed immunosensor for the analysis of human serum samples were tested by determining anti-tTG level in seven human serum samples, diluted 1:200 with 1X PBS. The secondary antibody used for these analyses is a biotinylated goat anti-human IgG antibody instead of the goat anti-mouse antibody previously used to determine the mouse anti-tTG standard available in the market. For this reason, concentrations of anti-tTG IgG in the serum samples were not calculated as absolute values, but evaluated comparatively with respect to standard fluoroenzyme immunoassay (FEIA) determinations. The ECL emission curves, reported in Figure 4.15, show well resolved ECL peaks of four of the samples analyzed. Even if the recorded peaks appeared slightly broader in potential than the ECL peaks obtained with the commercial standard solutions (see Figure 4.13A), this did not impair the analyses. Two serum

samples taken from healthy individuals did produce ECL signals not distinguishable from the background noise (i.e. 9463 and 9597 samples).
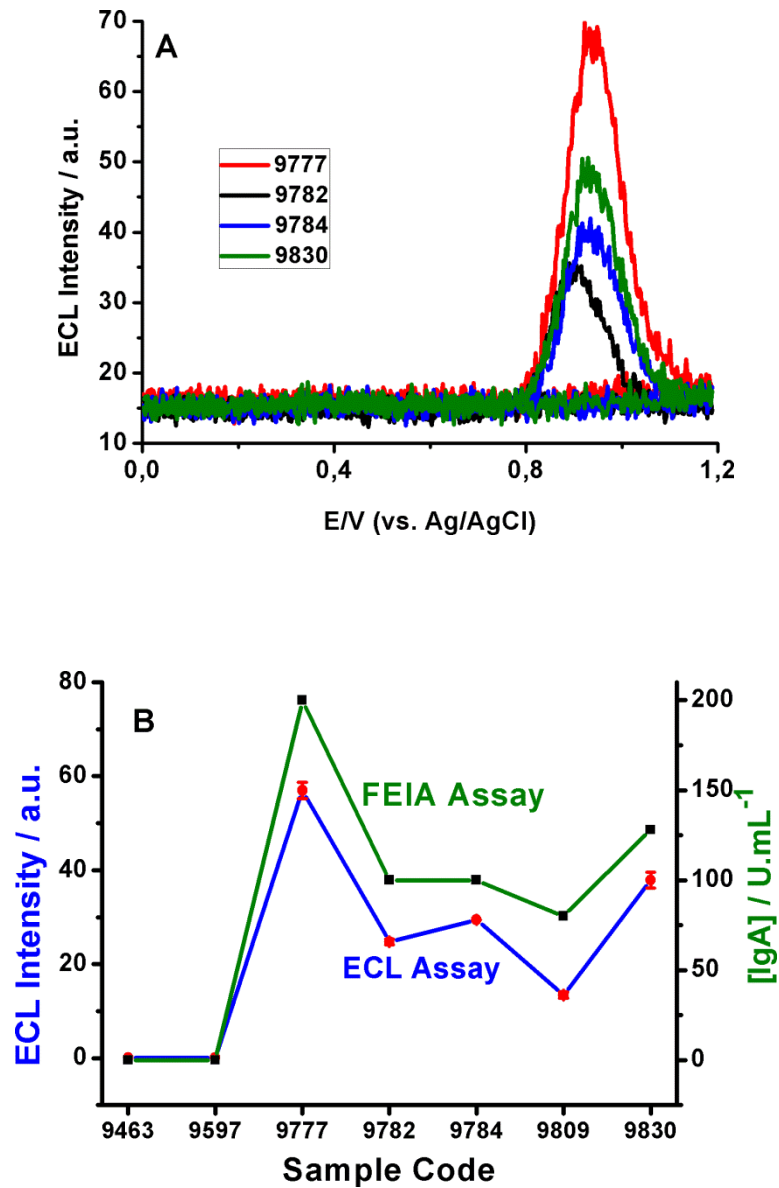

Figure 4.15 A) ECL signals detected with immunosensors for the evaluation of anti-tTG level in human serum samples (diluted 1:200 in 1X PBS); other experimental conditions as in Figure 4.4. **B)** Comparison of ECL intensities measured by the proposed ECL immunoassay with clinical results determined by fluoroenzyme immunoassay of serum samples from 5 CD patients (9777, 9782, 9784, 9809, 9830) and from 2 healthy individuals (9463, 9597).

Results obtained with the ECL immunosensor were compared at first with data for anti-tTG, IgG class obtained by FEIA, however, all the FEIA data were below the cutoff value of the method (normal value < 7 U mL^{-1}). A different situation was observed when comparing ECL results of IgG with FEIA results for IgA anti-tTG. Data reported in Figure 4.15B, shows a good agreement between the ECL and FEIA-IgA results. The two methods show almost parallel trends for both healthy subjects (samples 9463 and 9597) and celiac patients. Interestingly, the ECL results suggest a higher sensitivity to measure the IgG anti-tTG, than the FEIA method which identifies only IgA anti-tTG but not IgG anti-tTG antibodies.

4.4 Conclusions

This study demonstrates for the first time that NEEs can be successfully used for the detection by ECL of target proteins, in particular the anti-tTG antibody used as biomarker for the serological diagnosis of the celiac disease. The composite nature of NEEs, made of Au nanodisk electrodes embedded in a polymeric template, allowed us to exploit the wide surface of the PC membrane to immobilize a capture agent (namely, the antigen tTG) , the analyte and, finally, a luminescent ruthenium(II) label. According to this architecture, the nanoelectrodes act as electrochemical transducers for initiating the ECL emission while PC is exploited to perform the biorecognition event and to bind the luminescent label. Consequently, the electrochemical initiation of the ECL emission results from the electrochemical oxidation of the co-reactant TPrA in solution and not from that of the Ru(II) luminophore. Voltammetric and ECL data indicate indeed that the ruthenium complex is not oxidized directly at the surface of the nanoelectrodes, instead ECL is generated only by the electrochemical oxidation of TPrA, producing the radicals TPrA$^{\bullet+}$ and TPrA$^{\bullet}$ which live long enough to diffuse and to react with the luminophore, immobilized onto the neighboring PC membrane. Concerning the specific application goal, that is the serological diagnosis of the celiac disease, the NEE-based ECL sensors is characterized by high sensitivity, low detection limit (470 pg mL^{-1}), wide dynamic range and it can furnish diagnostically useful information for human serum analysis. The satisfactory agreement between data from the ECL sensor and from fluoroenzyme immunoassays in different clinical samples support the extension of the study to a higher number of samples, in order to evaluate the clinical sensitivity and specificity of the method.

From an analytical point of view, special advantage of the sensor is that the ECL emission is obtained by applying a potential of 0.88 V *vs* Ag/AgCl, that is about 0.3 V lower than in the case when ECL is initiated by the electrochemical oxidation of Ru(bpy)$_3^{2+}$ at 1.2 V *vs* Ag/AgCl . The lower operative potential reduces significantly the possible interference from side reactions in samples containing oxidizable species. Moreover, it reduces the ECL background arising from the reaction between Ru(bpy)$_3^{2+}$ and hydroxide ions in aqueous samples. Finally, it minimizes possible electrochemical damage of sensitive biomolecules and oligonucleotide sequences as well as it reduces the oxide formation on Au or Pt electrode surfaces. These advantages can be extended to other ECL sensors by using the same NEE platform for the immobilization of other capture agents, potentially suitable for the biorecognition of a wide range of antigen or antibody or oligonucleotide targets.

References

[1]   A. Tommasini, T. Not, V. Kiren, V. Baldas, D. Santon, C. Trevisiol, I. Berti, E. Neri, T. Gerarduzzi, I. Bruno, A. Lenhardt, E. Zamuner, A. Spano, S. Crovella, S. Martellossi, G. Torre, D. Sblattero, R. Marzari, A. Bradbury, G. Tamburlini, A. Ventura, *Arch. Dis. Child.* 2004, **89**, 512.

[2]   M. Maki, K. Mustalahti, J. Kokkonen, P. Kulmala, M. Haapalahti, T. Karttunen, J. Ilonen, K. Laurila, I. Dahlbom, T. Hansson, P. Hopfl, M. Knip, *N. Engl. J. Med.* 2003, **348**, 2517.

[3]   S. Lohi, K. Mustalahti, K. Kaukinen, K. Laurila, P. Collin, H. Rissanen, O. Lohi, E. Bravi, M. Gasparin, A. Reunanen *et al. Aliment. Pharmacol. Ther.* 2007, **26**, 1217.

[4]   Ventura, A.; Facchini, S. *Clin. Pediatr.* 2001, **40**, 575.

[5]   H. Hin, G. Bird, P. Fischer, N. Mahy, D. Jewell, *BMJ* 1999, **318**, 164.

[6]   M.L. Bianchi, M.T. Bardella, *Calcif. Tissue Int.* 2002, **71**, 465.

[7]   D. Bolotin, V. Petronic-Rosic, *J. Am. Acad. Dermatol.* 2011, 64, 1017.

[8]   M. Hadjivassiliou, D.S. Sanders, R.A. Grunewald, N. Woodroofe, S. Boscolo, D. Aeschlimann, *Lancet Neurol.* 2010, 9, 318.

[9]   L. Lepore, S. Martelossi, M. Pennesi, F. Falcini, M.L. Ermini, R. Ferrari, S. Perticarari, G. Presani, A. Lucchesi, M. Lapini, A. Ventura, *J. Pediatr.* 1996, 129, 311.

[10] T. Not, E. Faleschini, A. Tommasini, A. Repetto, M. Pasotti, V. Baldas, A. Spano, D. Sblattero, R. Marzari, C. Campana, A. Gavazzi, L. Tavazzi, F. Biagi, G.R. Corazza, A. Ventura, E. Arbustini, *Eur. Heart J.* 2003, **24**, 1455.

[11] A. Frustaci, L. Cuoco, C. Chimenti, M. Pieroni, G. Fioravanti, N. Gentiloni, A. Maseri, G. Gasbarrini, *Circulation* 2002, **105**, 2611.

[12] J. Ludvigson, S. Montgomery, A. Ekbom, *Gastroenterology* 2005, **129**, 454.

[13] G. Corrao, G.R. Corazza, V. Bagnardi, G. Brusco, C. Ciacci, M. Cottone, C.S. Guidetti, P. Usai, P. Cesari, M.A. Pelli, S. Loperfido, U. Volta, A. Calabro, M. Certo, *Lancet* 2001, **358**, 356.

[14] I.D. Hill, *Gastroenterology* 2005, **128** *(Suppl.)*, S25 .

[15] I.R. Korponay-Szabo, K. Szabados, J. Pusztai, K. Uhrin, E. Ludmany, E. Nemes, K. Kaukinen, A. Kapitany, L. Koskinen, S. Sipka *et al. BMJ* 2007, **335**, 1244.

[16] G. Nemec, A. Ventura, M. Stefano, G. Di Leo, V. Baldas, A. Tommasini, F. Ferrara, A. Taddio, A. Città, D. Sblattero, R. Marzari, T. Not, *Am. J. Gastroenterol.* 2006, **101**, 1597.

[17] P. Singh, N. Wadhwa, M.K. Chaturvedi, V. Bhatia, S. Saini, N. Tandon, G.K. Makharia, M. Maki, T. Not, A. Phillips, S. Bhatnagar, *Arch. Dis. Child.* 2014, **99**, 1004.

[18] P. Byass, K. Kahn, A. Ivarsson, *Plos One* 2011, **6**, e22774.

[19] S. Holding, F. Wilson, D. Spradbery, *J. Immunol. Methods* 2014, **405**, 29.

[20] A. Lerner, *International Journal of Celiac Disease* 2014, **2**, 64.

[21] I. Dahlbom, M. Olsson, N.K. Forooz, A.G. Sjoholm, L. Truedsson, T. Hansson, *Clin. Diagn. Lab. Immun.* 2005, **12**, 254.

[22] M. Maglio, A. Tosco, F. Paparo, R. Auricchio, V. Granata, B. Colicchio, V. Indolfi, E. Miele, R. Troncone, *JPGN* 2010, **50,** 43.

[23] N. Wang, L. Truedsson, K. Elvin, B.A. Andersson, J. Ronnelid, L. Mincheva-Nilsson, A. Lindkvist, J.F. Ludvigsson, L. Hammarstrom, C. Dahle, *PLOS ONE* 2014, **9**, e93180.

[24] K.A. Scherf, P. Koehler, H. Wieser, *Adv. Chem. Engineer. Sci.* 2015, **5**, 83.

[25] M. Giannetto, M. Mattarozzi, E. Umiltà, A. Manfredi, S. Quaglia, M. Careri, *Biosens. Bioelectron.* 2014, **62**, 325.

[26] S.V. Kergaravat, L. Beltramino, N. Garnero, L. Trotta, M. Wagener, M. I. Pividori, S.R. Hernandez, *Biosens. Bioelectron.* 2013, **48**, 203.

[27] M.M.P.S. Nevesa, M.B. González-Garcíac, H.P.A. Nouws, A. Costa-Garcíac, *Biosens. Bioelectron.* 2012, **31**, 95.

[28] S. Dulay, P. Lozano-Sánchez, E. Iwuoha, I. Katakis, C. K. O'Sullivan, *Biosens. Bioelectron.* 2011, **26**, 3852.

[29] M.I. Pividori, A. Lermo, A. Bonanni, S. Alegret, M. del Valle, *Anal. Biochem.* 2009, **388**, 229.

[30] Z. Liu, W. Qi, G. Xu, *Chem. Soc. Rev.* 2015, **44**, 3117.

[31] W. Miao, *Chem. Rev.* 2008, **108**, 2506.

[32] N.P. Sardesai, J.C. Barron, J.F. Rusling, *Anal. Chem.* 2011, **83**, 6698.

[33] L. Hu, G. Xu, *Chem. Soc. Rev.* 2010, **39**, 3275.

[34] R.J. Forster, P. Bertoncello, T.E. Keyes, *Annu. Rev. Anal. Chem.* 2009, **2**, 359.

[35] E.H. Doeven, G.J. Barbante, E. Kerr, C.F. Hogan, J.A. Endler, P.S. Francis, *Anal. Chem.* 2014, **86**, 2727.

[36] B.V. Chikkaveeraiah, A.A. Bhirde, N.Y. Morgan, H.S. Eden, X. Chen, *ACS Nano* 2012, **6**, 6546.

[37] M. Milutinovic, S. Sallard, D. Manojlovic, N. Mano, N. Sojic, *Bioelectrochemistry* 2011, **82**, 63.

[38] F. Deiss, C.N. LaFratta, M. Symer, T.M. Blicharz, N. Sojic, D. R. Walt, *J. Am. Chem. Soc.* 2009, **131**, 6088.

[39] W. Miao, A.J. Bard, *Anal. Chem.* 2003, **75**, 5825.

[40] G. F. Blackburn, H.P. Shah, J.H. Kenten, J. Leland, R.A. Kamin, J. Link, J. Peterman, M.J. Powell, A. Shah, D.B. Talley, S.K. Tyagi, E. Wilkins, T.-J. Wu, R.J. Massey, *Clin. Chem.* 1991, **37**, 1534.

[41] K. Muzyka, *Biosens. Bioelectron*. 2014, **54**, 393.

[42] N. Sardesai, S. Pan, J. Rusling, *Chem. Commun.* 2009, 4968.

[43] H. Zhang, Z. Han, X. Wang, F. Li, H. Cui, D. Yang, Z. Bian, *ACS Appl. Mater. Interfaces* 2015, **7**, 7599.

[44] K. Kadimisetty, S. Malla, N. P. Sardesai, A. A. Joshi, R. C. Faria, N. H. Lee, J. F. Rusling, *Anal. Chem.* 2015, **87**, 4472.

[45] W.-J. Shen, Y. Zhuo, Y.-Q. Chai, Z.-H. Yang, J. Han, R. Yuan, *ACS Appl. Mater. Interfaces* 2015, **7**, 4127.

[46] X. Jiang, H. Wang, R. Yuan, Y. Chai, *Biosens. Bioelectron.* 2015, **63**, 33.

[47] J. Zhou, N. Gan, T. Li, F. Hu, X. Li, L. Wang, L. Zheng, *Biosens. Bioelectron.* 2014, **54**, 199.

[48] Y. Zhuo, G. Gui, Y. Chai, N. Liao, K. Xiao, R. Yuan, *Biosens. Bioelectron.* 2014, **53**, 459.

[49] H. Qi, X. Qiu, D. Xie, C. Ling, Q. Gao, C. Zhang, *Anal. Chem.* 2013, **85**, 3886.

[50] J. Jiang, Y. Chai, H. Cui, *RSC Advances* 2011, **1**, 247.

[51] N. Sardesai, S. P. J. Rusling, *Chem. Commun.* 2009, 4968.

[52] M. Sentic, M. Milutinovic, F. Kanoufi, D. Manojlovic, S. Arbault, N. Sojic, *Chem. Sci.* 2014, **5**, 2568.

[53] W. Miao, A.J. Bard, *Anal. Chem.* 2004**, 76**, 7109.

[54] M.-J. Li, Z. Chen, V.W.-W. Yam, Y. Zu, *ACS Nano* 2008, **2**, 905.

[55] F. Li, Y. Zu, *Anal. Chem.* 2004, **76**, 1768.

[56] F.C. Pereira, L.M. Moretto, M. De Leo, M.V.B. Zanoni, P. Ugo, *Anal. Chim. Acta* 2006, **575**, 16.

[57] B. Brunetti, P. Ugo, L.M. Moretto, C.R. Martin, *J. Electroanal. Chem.* 2000, **491**, 166.

[58] P. Ugo, L.M. Moretto, S. Bellomi, V.P. Menon, C.R. Martin, *Anal. Chem.* 1996, **68**, 4160.

[59] V.P. Menon, C.R. Martin, *Anal. Chem.* 1995, **67**, 1920.

[60] L.M. Moretto, M. Tormen, M. De Leo, A. Carpentiero, P. Ugo, *Nanotechnology* 2011, **22**, 185305.

[61] P. Ugo, L.M. Moretto, M. De Leo, A.P. Doherty, C. Vallese, S. Pentlavalli, *Electrochim. Acta* 2010, **55**, 2865.

[62] J.C. Hulteen, V.P. Menon, C.R. Martin, *J. Chem. Soc., Faraday Trans.* 1996, **92,** 4029.

[63] P. Ugo, L.M. Moretto, In *Hand Book of Electrochemistry*; Zoski, C., Ed.; Elsiver: Amsterdam, 2007; pp 678 – 709.

[64] M. Ongaro, P. Ugo, *Anal. Bioanal. Chem.* 2013, **405**, 3715.

[65] S.P. Mucelli, M. Zamuner, M. Tormen, G. Stanta, P. Ugo, *Biosens. Bioelectron.* 2008, **23**, 1900.

[66] M. Silvestrini, L. Fruk, P. Ugo, *Biosens. Bioelectron.* 2013, **40**, 265.

[67] M. Silvestrini, P. Ugo, *Anal. Bioanal. Chem.* 2013, **405**, 995.

[68] F. Bottari, P. Oliveri, P. Ugo, *Biosens. Bioelectron.* 2014, **52**, 403.

[69] H.B. Habtamu, P. Ugo, *Electroanalysis* 2015, **27**, 2187.

[70] P. Ugo, N. Pepe, L.M. Moretto, M. Battagliarin, *J. Electroanal. Chem.* 2003, **560**, 51.

[71] W. Miao, J.P. Choi, A. J. Bard, *J. Am. Chem. Soc.* 2002, **124**, 14478.

[72] V.A. Zamolo, G. Valenti, E. Venturelli, O. Chaloin, M. Marcaccio, S. Boscolo, V. Castagnola, S. Sosa, F. Berti, G. Fontanive, M. Poli, A. Tubaro, A. Bianco, F. Paolucci, M. Prato, *ACS Nano* 2012, **6**, 7989.

[73] Z. Chen, Y. Zu, *J. Phys. Chem. C* 2009, **113**, 21877.

[74] R. M. Wightman, S.P. Forry, R. Maus, D. Badocco, P. Pastore, *J. Phys. Chem. B* 2004, **108**, 19119.

[75] L.M. Moretto, T. Kohls, D. Badocco, P. Pastore, N. Sojic, P. Ugo, *J. Electroanal. Chem.* 2010, **640**, 35.

[76] M. Silvestrini, P. Schiavuta, P. Scopece, G. Pecchielan, L.M. Moretto, P. Ugo, *Electrochim. Acta* 2011, **56**, 7718.

[77] J.D. Winefordner, G.L. Long, *Anal.Chem.* 1983, **55**, 712A.

5. Concluding remarks

This thesis demonstrates the applicability of Au NEEs for developing enzymatic and affinity sensors suitable for advanced molecular diagnostic purposes.

The composite nature of Au NEEs allowed us to immobilize adequate amounts of biorecognition molecules on the wide polycarbonate surface, while the metallic portion of the NEEs is exclusively dedicated to the electrochemical reaction. This smart biomolecule immobilization approach helped us to retain the desirable advantages of NEEs, in particular, high signal to background current ratios, enhanced mass fluxes and high miniaturizability. Moreover, the absence of any electrode pretreatment procedure reduced the analytical steps and reagents required. Since the biologicals are deposited on an organic polymer, biological processes occur in a more "natural" environment, being less exposed to electrical and electrochemical stress.

This innovative approach has been previously demonstrated by our group for the development of immuno- and DNA-sensors. Here, we extended the concept to the development of miniaturized enzyme biosensor, and to immunosensors specifically devoted to the detection of celiac disease biomarkers.

In the former case, taking advantage of the high density of nanodiscs in the NEEs, we demonstrated the miniaturization of the overall size of NEEs down to sub-mm dimension without deteriorating the inherent analytical advantages. The miniaturized NEEs are used to develop an efficient glucose microbiosensor *via* immobilizing GOx on the polycarbonate part.

In the second case, we demonstrated the feasibility of this innovative approach for development of two kinds of anti-tTG based celiac disease immunosensors differing in the detection method, namely: electrochemical and ECL detection formats.

The electrochemical detection relies on the use of HRP as label and hydroquinone as a mediator. By this way, a highly sensitive electrochemical immunosensor was developed and evaluated for the determination of the anti-tTG IgG isotype involved in CD. So far, this is the first report demonstrating the application of NEEs as detection platform for CD biomarker.

Furthermore, for the first time we integrated the advantages of NEEs with state-of-the art ECL detection. With this design, the electrochemical reaction and the location of ECL emission are spatially separated, allowing us to develop a highly sensitive anti-tTG immunosensor that works at an applied potential lower than the usual ECL systems.

The electrochemical and ECL immunosensors of CD are applied to human serum samples, showing to be suitable to discriminate between healthy and celiac patients. A comparison between the two approaches indicated that the ECL based immunosensor achieved a lower detection limit than the electrochemical detection.

Future research efforts need to be devoted to the investigation of the nature of interaction between macromolecules and PC membrane, as well as the utilization of NEEs for development of multiplexed biosensors. The sensors here developed show anyway excellent detection capabilities which allow the extension of their application to a wide number of samples, in order to examine and hopefully validate their applicability for clinaicl diagnostics purposes.

Appendix

A. Preliminary experiments with arrays of micro- and nano-electrodes

During my study on NEE based biosensors, I examined also the possibility to apply, for similar goals, different types of arrays of micro- and nano-electrodes. Preliminary experiments with these electrochemical devices allowed me to point out some interesting properties whose description constitute the topic of this Appendix.

A1. Modification of individually addressable microelectrode arrays

Individual addressing of microelectrode arrays (MEAs) is realized by connecting each electrode by its own to a corresponding bond pad on the chip border or by an integrated circuit [1]. Individually addressable MEAs offer substantial advantages including rapid response, high spatial resolution, the possibility of simultaneous multi-analyte detection, and probing signal transmission in a network of biological cells [2-3]. The most common methods for the fabrication of MEA include photolithography, reactive ion etching, screen printing, and sonochemical ablation [4-6].

However, these techniques are expensive and time consuming. As an innovative alternative, a simple and cheap way to fabricate arrays of gold microelectrodes was reported by Nascimento *et al* in 1997 [7]. In this method surplus, defective, damaged (but not overheated) or low priced brand new integrated circuit chips can constitute the 'raw material' for the manufacture of individually addressable gold MEA. This opens interesting prospects for the development of cheap arrays of electrochemical sensors with multiplexed detection capabilities.

In this preliminary work, we present the fabrication, characterization and electrochemically directed modification of each element in the microelectrode arrays. The characterization was conducted by cyclic voltammetry to test for cross talk among the microelectrodes in the array and to distinguish good electrodes from non-functioning ones. Each electrode was run individually and investigated in different combinations [8].

In order to use the individual microelectrodes in an array independently for development of multiplex biosensors, the individual elements should be independently modified and biorecognition elements should be immobilized on each element independently. This can be achieved by electrochemically directed modification technique. Here, the electrodes are electrochemically modified with conducting polymers (polypyrrole and polyanthranilic acid) and Prussian blue. These modifiers are chosen due to two main reasons, i) suitability for electrochemical polymerization in order to achieve controlled modification of each element in the array and ii) their conductive nature reduces the possible insulation of the feeble current at the microelectrodes. Moreover, the conducting polymers can be used as suitable matrixes for biomolecules immobilization [9,10], whereas, the Prussian blue is suitable for further investigation of electrochemical directability of the modifier and to investigate the electrochemical performances of the modified microelectrodes analyte detection e.g. H_2O_2 [11-13].

A1.1 Experimental

Instruments and Materials

For electrochemical measurements CHI 660B potentiostat (TX, USA), electrolyte cell with three electrodes-Pt wire counter electrode, Ag/AgCl (in Sat. KCl), Au microelectrode arrays, Faraday cage. All chemicals including pyrrole and anthranilic acid are reagent grades. (Ferrocenylmethyl)trimethylammonium hexafluorophosphate ($FA^+PF_6^-$) was prepared by metathesis of the (ferrocenylmethyl)trimethylammonium iodide with potassium hexafluorophosphate (Alfa Aesar), Alce Natural honey bought from the market.

Methodology

Fabrication and characterization of the MEAs

The arrays of individually addressable gold microelectrodes were fabricated from discarded computer chips and epoxy resin as proposed by Nascimento *et al* 1997 [7]. Briefly, integrated circuit chips of discarded computer were sawed in cross-section through the middle, normal to the longest axis (as shown in Figure A1) in order to destruct the silicon circuit and expose the gold wires that are connected to the external pins (Figure A2).
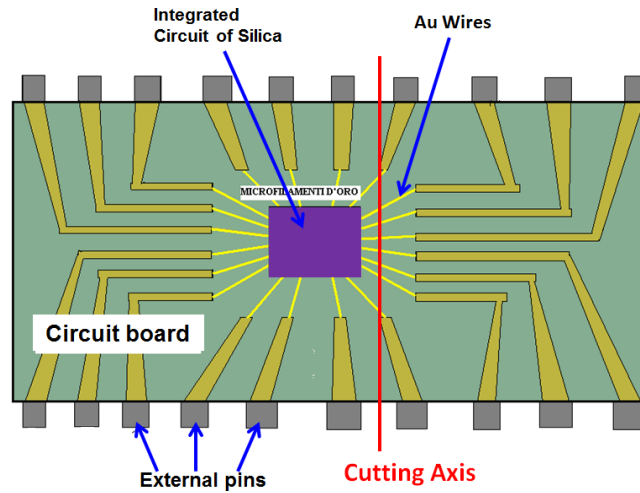
Figure A1 Scheme of an integrated circuit chip showing the cutting axis
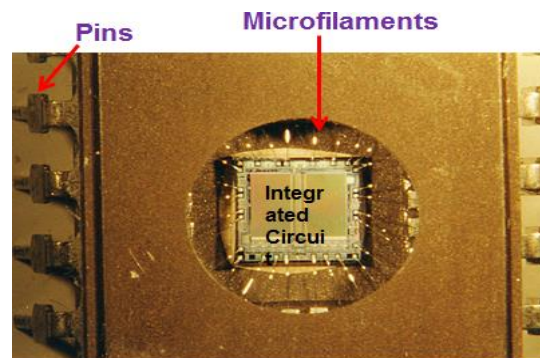

Figure A2 Conventional integrated electronic circuit (chip) with exposed gold filaments and external pins.

Polishing the resulting rough surface exposes the tips of the wires of the chip in the form of arrays of microdisks. Electric contact was established for each microdisk from the external pins and the body of the electrodes was insulated using epoxy resin (Figure A3).
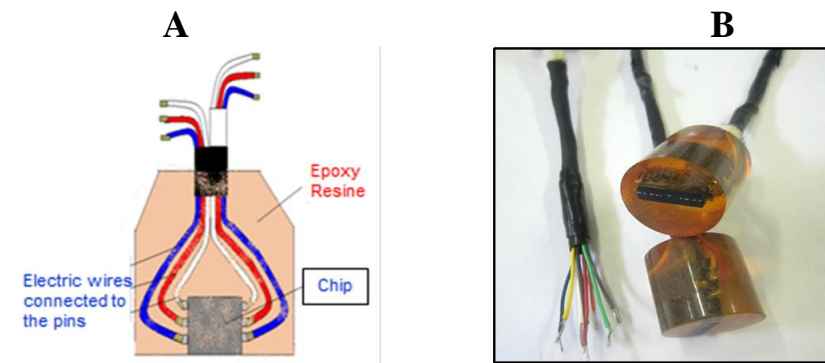

Figure A3 A) Scheme showing how the electric contacts are established and the insulation with epoxy resine, **B**) photograph of the fabricated microelectrode arrays.

The number of microelectrodes of an array is determined by the number of pins in the chip. Some of the wires can be destructed while cutting and up to 12 microelectrodes can be found in each array. The surfaces of the electrodes were smoothed by polishing with abrasive paper. The microarrays were further cleaned by sonication in deionized water and by electrochemical cycling in 0.1 M H_2SO_4. The individual elements in an array as well as different external combinations were electrochemically characterized using $FA^+PF_6^-$ as redox probe.

Modifications of the microelectrode arrays

Potentiodynamic or potentiostatic method is used depending on the efficiency of polymerization, film quality and uniformity all over the surface of the microelectrodes [2]. At least one microelectrode in an array was left free of the polymerization potential as a control for electrochemical directability of the modifiers.

Modification with polypyrrole (PPY)

One of the MEAs containing 6 microelectrodes was dipped in to phosphate buffer pH 7.4 electrolyte solution containing 0.5M pyrrole previously purified by distillation. PPY was potentiostatically polymerized on each of the five microelectrodes at +0.8 V for 5, 30, 60, 90, or 120 s. The sixth microelectrode of the array was left as a control. The effect of polymerization potential was also investigated using another MEA.

Modification with polyanthranilic acid (PAA)

PAA was electropolymerized as reported by Taleat *et al* [14]. Briefly, PAA was electrochemically polymerized from a solution of 1 M H_2SO_4 + 0.1 M KCl containing 0.05 M the monomer, anthranilic acid, by cyclic voltammetry between 0 and +1.0 V *vs* Ag/AgCl at scan rate of 50 mV s^{-1} for 15 cycles. After deposition of the polymer film, the modified array was transferred to a fresh supporting electrolyte solution for film characterization.

Modification with Prussian blue (PB)

PB was electrodeposited from a solution containing 2.5 mM $FeCl_3$ + 2.5 mM $Fe(CN)_6$ in a supporting electrolyte of 0.1 M KCl + 0.1 M HCl pH 1 potentiostatically at +0.4 V for 40 s [15-17]. The modified electrode was carefully transferred to a solution of 0.1 M KCl + 0.1 M HCl pH 1 and electrochemically cycled 25 times between -0.05 and 0.35 V at scan rate 50 mV s^{-1}.

Electrode was immersed in to 0.05 M K_2HPO_4/KH_2PO_4 + 0.1 M KCl pH 6.5 and conditioned at -0.05 V for 10 min and by cycling between -0.05 and 0.35 V for 25 cycles. The PB modified microelectrodes were used for the preliminary determination of GOx in natural honey.

A1.2 Results and discussions

Characterization of the arrays

Prepared arrays were electrochemically characterized before modification. The CV shown in Figure A4 was recorded at a single microelectrode in H_2SO_4 during the electrochemical cleaning. Because the CV is typical characteristic of gold electrodes, it proofs that the micro-disc arrays are made up of gold electrodes.
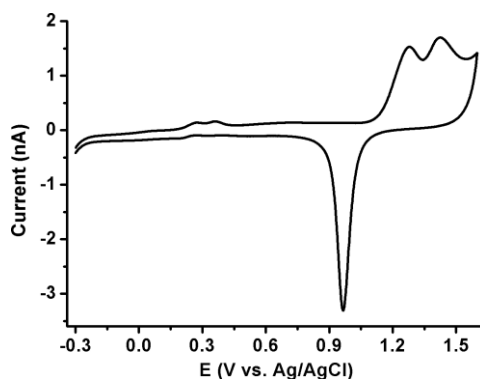
Figure A4 Cyclic voltammogram recorded at a single microelectrode of an array in 0.1 M H_2SO_4 at scan rate of 100 mV s^{-1}.

The electrochemical behaviors of the microelectrode arrays were further studied by cyclic voltammetry in 2.5 mM $FA^+PF_6^-$ in 0.1 M $NaNO_3$ supporting electrolyte at different scan rates. Figure A5 shows CVs of a typical microelectrode at scan rates ranging from 0.005 to 1 V s^{-1}. The CVs were recorded with the electrochemical set up in a Faraday cage as the measured current at or below nano-amperes level. As the scan rate increases, the diffusion behavior changes resulting in the transition of the CVs from sigmoidal to peak shape. Sigmoidally shaped voltammograms instead of peak-shaped ones, at medium scan rates, is typical for a microelectrode. Thus, these CVs clearly characterize the array electrodes as microelectrodes [1].
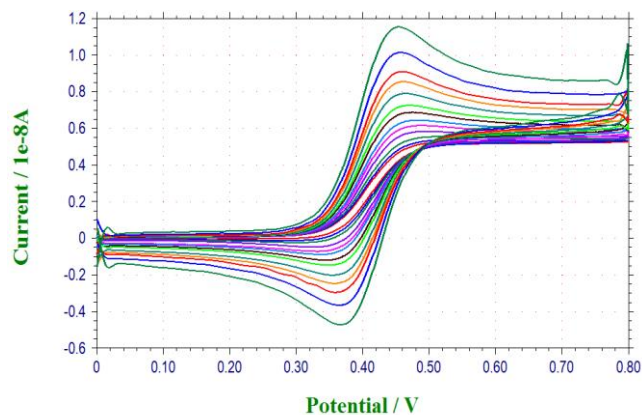
Figure A5 CVs recorded at a single microelectrode of an array at scan rates ranging from 0.005 to 1 V s^{-1}.

The transition from sigmoidal to peak shape can be clearly seen from representative CV given in Figure A6. At scan rates up to about 100 mV s^{-1}, radial diffusion dominates producing sigmoidal CVs; but above this scan rate characteristic CVs of transitional diffusion mode were observed. At very fast scan rates, the peak-shaped CVs indicate that the electrodes work at planar diffusion behavior.
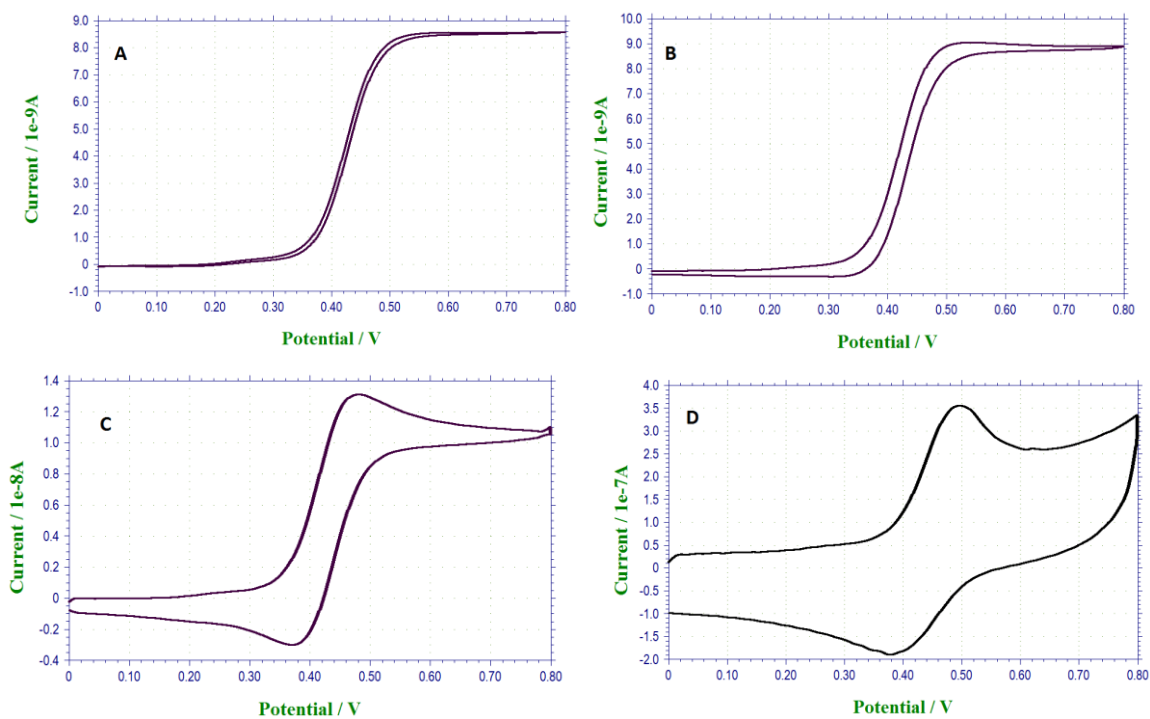

Figure A6 CVs recorded at a single microelectrode of an array at different scan rates **A**) 0.001, **B**) 0.02, **C**) 0.5 and **D**) 500 V s^{-1} in 0.1 M NaNO$_3$ containing 2.5 mM FA$^+$PF$_6^-$.

In addition to the investigation of the electrochemical behaviors of the individual and groups of microelectrodes, the characterization helped us to identify any cross talk among the individual elements in the arrays, to identify defective elements of the array, and to estimate the size and distances between the microelectrodes in the array.

External interconnection between the elements of the array allows to amplify the current by a factor of n, where n is the number of microelectrodes of the array (typically, n = 6-12). Figure A7 shows the CVs of different combinations of microelectrodes in an array where the numbers of microelectrodes externally combined is indicated on each CV (n=1, 2, 3, or 6).

When different numbers of electrodes are externally combined, the total limiting current is the same as the sum of the limiting currents at the individual elements in the combination, if there is no cross-talk among the elements combined. The sigmoidally shaped curves resulted from combination of all microelectrodes in an array clearly indicates that the distance between the microelectrodes in the array is large enough so that diffusion layers are not overlapping. This is in agreement with the report by Nescimento *et al* 1997 [7], where x-ray images of the chips and micrographs of the resulting surface of the arrays have revealed variable distances between neighbor microelectrodes, which are, however, larger than 10 times the radius of the disks. This feature of the microelectrodes prevents diffusional cross-talk between the electrodes.
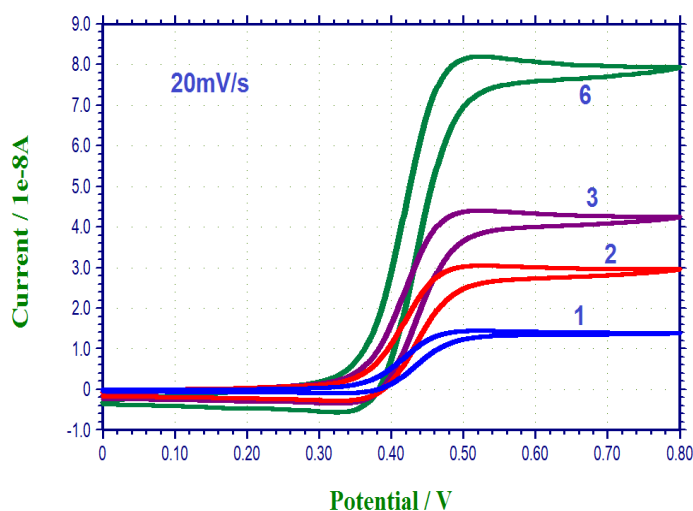

Figure A7 CVs recorded in 0.1 M $NaNO_3$ containing 2.5 mM $FA^+PF_6^-$ at different combination of microelectrodes of an array at scan rate of 20 mV s^{-1}. The numbers on each CV indicate the number of microelectrodes of an array externally combined.

The fact that the current density does not significantly depend on whether only an individual electrode is addressed or combination of array electrodes are addressed, proves the absence of cross talk among electrodes, size uniformity of the members of the arrays and absence of diffusion layers overlap. Therefore, the 6 individual electrode signals can be regarded as 6 independent current signals at long or intermediate time scales.

Data in Figure A8 Show the difference in CVs among the microelectrodes of the same or different arrays. The significant difference in the limiting currents of some elements of an array is most likely due to the electrode size difference resulted from the different angles of the micro-wires to the cutting axis of the chips. As can be seen from Figure A1, wires at the center of the cutting axis provide somehow microdisks with diameter same as the diameter of the microwires. However, those at the edge of the sawing axis can be cut diagonally and hence their exposed surface diameter could be more than the diameter of the micro gold wires. The microelectrodes in chip A seem to be more uniform in area than those in chip B of Figure A8.
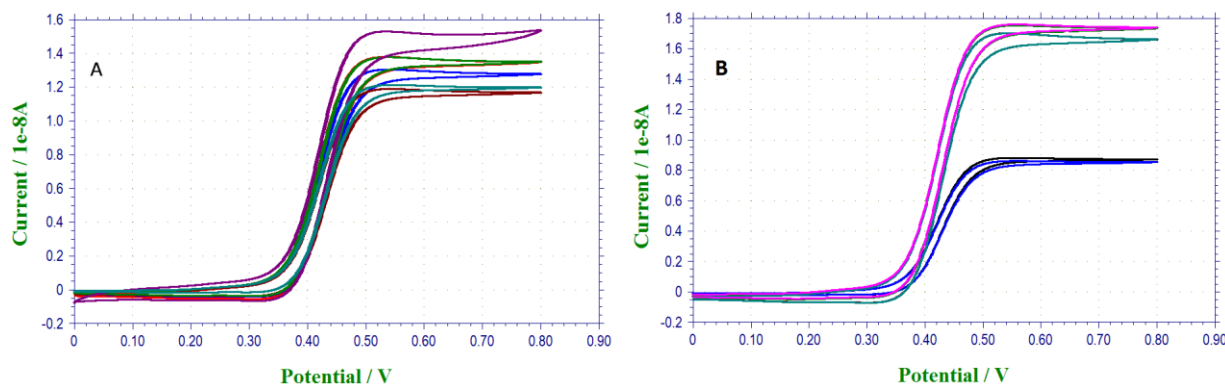

Figure A8 CVs recorded at each microelectrode of two representative arrays (chips) in 0.1 M NaNO$_3$ containing 2.5 mM FA$^+$PF$_6^-$ at scan rate of 10 mV s^{-1}; **A**) represents an array composed of uniform elements, while **B**) represents variable sized electrodes in the array.

For calculating the radius of each microelectrode, two scan rates were used. A CV recorded at very fast scan rate which can produce peak shaped voltammogram where the peak current is governed by the Randles-Sevcik equation (Eq. 1), whereas a second CV recorded at slow scan rate that can produce perfectly sigmoidal CV where steady-state current equation for disk-shape microelectrodes can be applied (Eq. 2). Using the two equations of current and applying the mathematical concept of simultaneous equation, the radius of each microelectrode was calculated [18]. From this calculation an average radius of 33.1 ± 5 μm was obtained.

$$i_p = 2.69 \text{X} 10^5 n^{3/2} A C D^{1/2} v^{1/2} \qquad \text{Eq. 1}$$

$$i_m = 4mnFDCr \qquad \text{Eq. 2}$$

Modification of individual elements of the arrays

Polypyrrol (PPY)

The chronoamperograms of five microelectrodes of an array recorded during the polymerization of PPY for different duration of time at 0.8 V are displayed in Figure A9. Although the rate of current decline and the level where it stabilizes differ among the electrodes, they follow the same profile where an initial abrupt decline in current is followed by more stable current signal. This indicates that initial formation of the polymer film creates an additional diffusion layer causing significant reduction in current. However, the rate of decline decreases as the polymer deposition continues due to the conductive nature of the polymer.
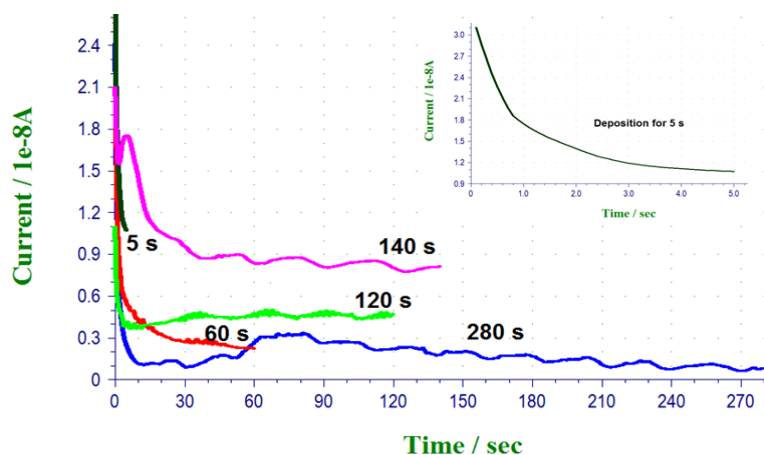
Figure A9 Chronoamperograms recorded during potentiostatic (at +0.8 V) synthesis of PPY at five microelectrodes of an array (chip) each for different time interval (5, 60, 120, 140, and 280 s). *Inset*: magnified chronoamperogram of 5 s PPY polymerization.

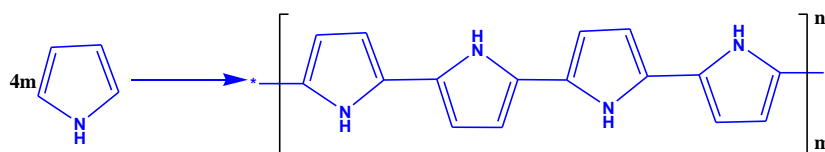The net equation for the mechanism of PPY polymerization is shown below [19,20].

Figure A10 shows CVs at a typical PPY modified as well as control microelectrodes of an array. A microelectrode, to which the polymerization potential was applied, has shown characteristic

CV of PPY while the microelectrode in the same array to which the polymerization potential was not applied, has not show this characteristic CV. This indicates that the polymerization is electrochemically directed. The CVs presented in Figure A11, recorded at the PPY modified microelectrodes, have shown characteristic voltammograms of PPY except the control (dashed line of Figure A11). The behavior of the polymer film was studied at different time and deposition potentials. Generally, the peak current increased with an increase in deposition time (Figure A11.A) and deposition potential (Figure A11.B).
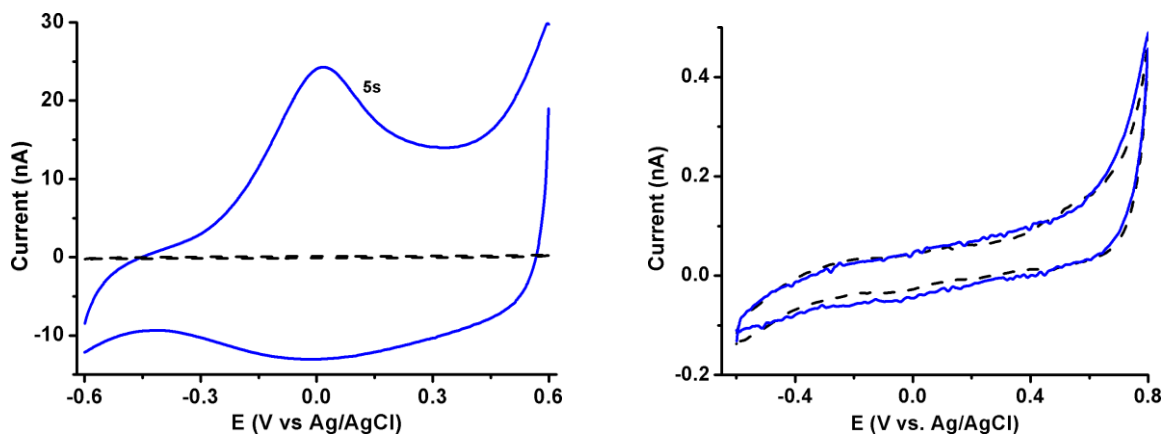

Figure 10 CVs recorded in PBS before (dash line) and after (full line) polymerization at two microelectrodes of an array A) to which PPY is deposited at 0.8 V for 5 s, and B) to which polymerization potential was not applied. Scan rate 20 mV s^{-1}.
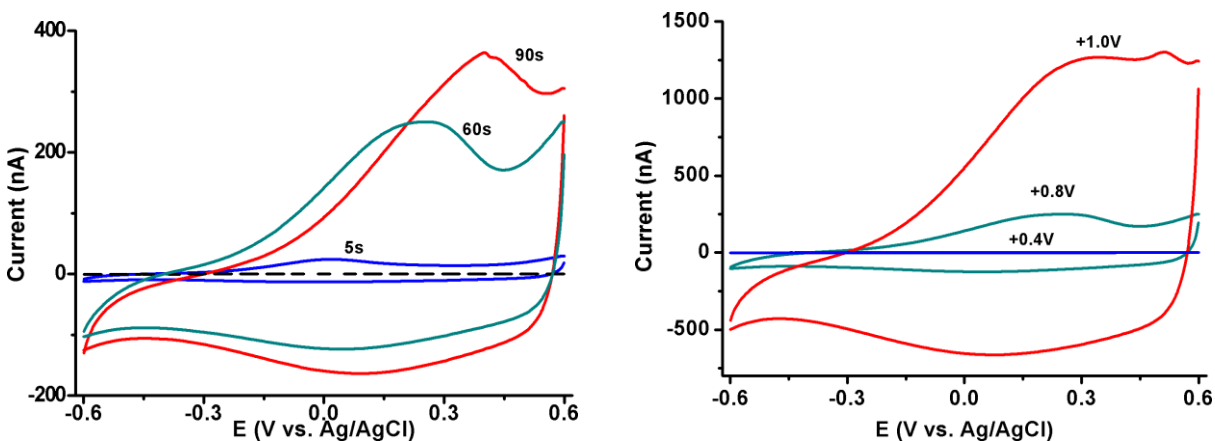

Figure A11 CVs recorded at PPY modified microelectrodes of a chip; **A**) after potentiostatic polymerization at +0.8 V but for different polymerization time (0, 5, 60 and 90s), **B**) after polymerization at different potential but at constant polymerization time (i.e. 5 s). Scan rate 20 mV s^{-1}. NB: the dashed CV in A represents the control microelectrode.

In both cases the anodic peak of PPY is anodically shifted with deposition potential and time. The electrochemical performance of the polymer was dependent on the potential applied; at potentials cathodic to about -0.3 V, the polymer is less conductive however at potentials anodic to this value, the polymer is a good conductor as evidenced by the increase in current. The changes in the chemical state of the polymer at different potentials are discussed by Ateh *et al.* [20].

The control electrodes which were not exposed to the polymerization potential did not show any change in current after modification of the other electrodes in the same array. This indicates that the polymerization is well directed to the electrode of interest in the array. Interestingly, one of the control microelectrodes of the array (after modification of its neighbors) has shown characteristic CV of PPY which evidenced the deposition of the polymer film without intentional application of the polymerization potential. This result in combination with the identical steady state current value of two elements of the array during the CV characterization evidenced that the two electrodes are in electrically contact.

Polyanthranilic acid (PAA)

Figure A12A shows the CVs recorded during the PAA polymerization from a solution of 1 M H_2SO_4 and 0.1 M KCl containing 0.05 M anthranilic acid. The potential was scanned between 0 and +1.0 V. During the first anodic scan, the two characteristic oxidation peaks of PAA between 0.25 and 0.55 V did not appear.

However, a strong irreversible oxidation peak around 0.9 V evidences the formation of the radical cation of the monomer which spontaneously couple either with another radical cation or neutral monomer molecule [19-20]. In the progressive scans, the growth of the electroactive polymer film can be inferred from the progressive increment of the two pairs of peak currents at around 0.271 V/0.296 V and 0.511 V/0.308 V (Figure A12.A). It is inline with literature reports where the anodic peak at lower oxidation potential is attributed to removal of electron from the nitrogen atom forming a radical cation [21]. The second oxidation peak is due to the oxidation of the semiquinone radical cation (polaron state) to quinonimin (bipolarone state) [21]. The decrease in the current at potentials cathodic from 0 indicates the passivation of the polymer becoming non-conductive (Figure A12.B). These two pairs of peaks resemble those characteristic of polyaniline that are usually assigned to the polaron and bipolaron formation [22].

These characteristic peaks of PAA were not observed at the control microelectrodes to which potential was not applied during the polymerization step. Stability of the polymer film was studied at pH values convenient for biomolecule immobilization.
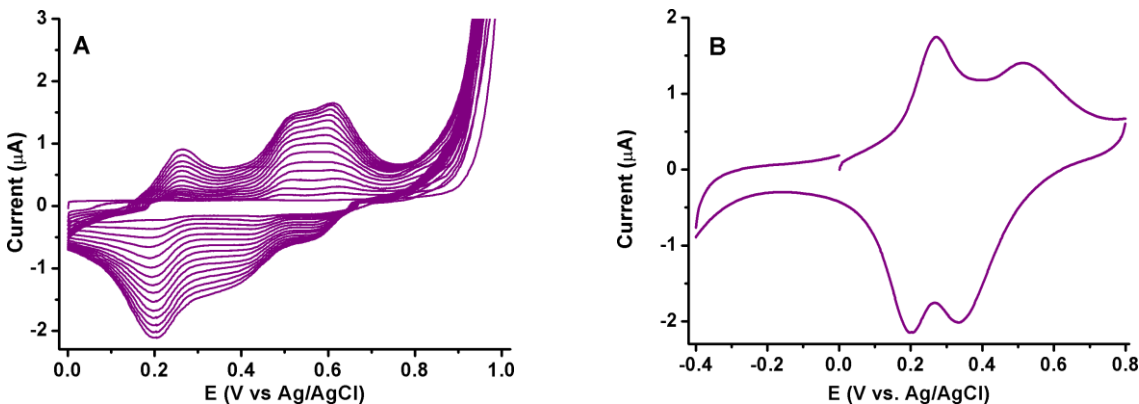

Figure A12. A) Electropolymerization of PAA by CV from 1M H_2SO_4 + 0.1M KCl solution containing 0.05 M anthranilic acid monomer between 0 and +1.0 V at 50 mV s^{-1} for 15 cycles; **B**) CV at PAA modified electrode in the supporting electrolyte solution.

Although, the polymer film is intact and quite stable at strong acidic medium, increasing the pH of the test solution to weakly acidic, neutral and then basic pHs, resulted in the disappearance of the characteristic voltammetric peaks almost completely. In order to get information on whether the disappearance of the peaks is due to polymer loss or deactivation, after recording the CVs at pH 7.4, the polymer modified electrode was transferred again to the strongly acidic solution and CV was recorded. But, the characteristic features of PAA CV were not regained suggesting partial or complete loss of the polymer film (Figure A13). Reports in the literature are contradicting; many indicating that the polymer dissolves at solutions other than strong acid but there are still reports on biosensors developed using the polymer in basic media [9,14].
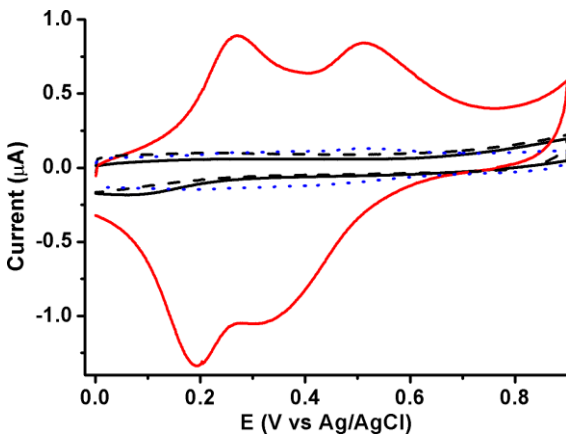

Figure A13 CVs of a bare electrode in supporting electrolyte (black solid line), PAA coated electrode in strong acid (red solid line), PAA coated electrode in PBS pH 7.4 (dashed line) and PAA coated electrode in strong acid after cycling in the PBS solution (dotted line).

Trials of immobilizing GOx and tTG enzymes after EDC/sulfo-NHS system activation were not successful basically due to the unstable nature of the polymer film at weakly acidic, neutral and basic pHs that are convenient to work with biological molecules.

Despite its instability, this polymer could be advantageous for development of biosensors due to the presence of free –COOH for covalent bonding with proteins [23].

Prussian blue (PB)

Figure A14 shows repetitive cycles of PB modified microelectrode of an array. It was recorded during the 25 cycle activation step of the deposited film. The peak currents progressively increase with number of cycles.
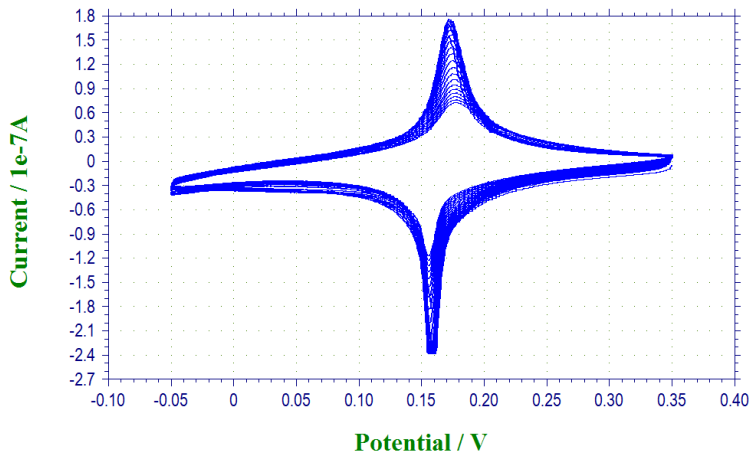

Figure A14 Repetitive cycling of PB modified Au microelectrode in a solution of 0.1 M KCl/HCl at scan rate of 20 mV s^{-1}.

The stability of the PB film was significantly improved by drying the modified electrode at 100°C for 1 h [17,24]. Then the modified electrodes were used to determine glucose oxidase enzyme in honey sample. Because the wound healing effect of natural honey is associated to the antiseptic property of H_2O_2 produced by the action of GOx on the glucose of diluted honey [11,12,25].

The full line in Figure A15 is recorded at a PB modified microelectrode of a chip in buffer solution. The dashed line CV in Figure A15.A, is recorded in 40 % diluted Alce honey sample after 30 minutes of dilution as previously reported by Bang *et al* 2003 [26]. The increase in current recorded during the cathodic scan is most likely due to the H_2O_2 produced in the honey by the GOx enzyme. The reduction in the anodic peak current is an additional evidence for the enzymatic production of H_2O_2. The cathodic current resulting from the enzyme catalyzed

reaction was further increased on addition of external 1 µg mL^{-1} GOx as shown by the dashed line CV in Figure 15B. Addition of Catalase enzyme (which consumes the H_2O_2) into the solution has caused the disappearance of the increased catalytic current (see dash-dot line of Figure 15B). This indicates that the cathodic current in the honey solution, is caused by the H_2O_2 produced by the GOx in the honey solution. It is important to note that after dilution and filtration, the honey solution is still slightly viscose creating problem on the development of diffusion controlled electroanalytical methods with macroelectrodes. However, microelectrodes are typically suitable for such electrochemical experiments in viscous solutions. The analysis of the honey sample cannot be done without dilution due to two reasons; i) the sample is too viscous, and ii) the GOx enzyme found in the concentrated honey starts oxidizing the glucose after dilution of the sample [11,12,25].
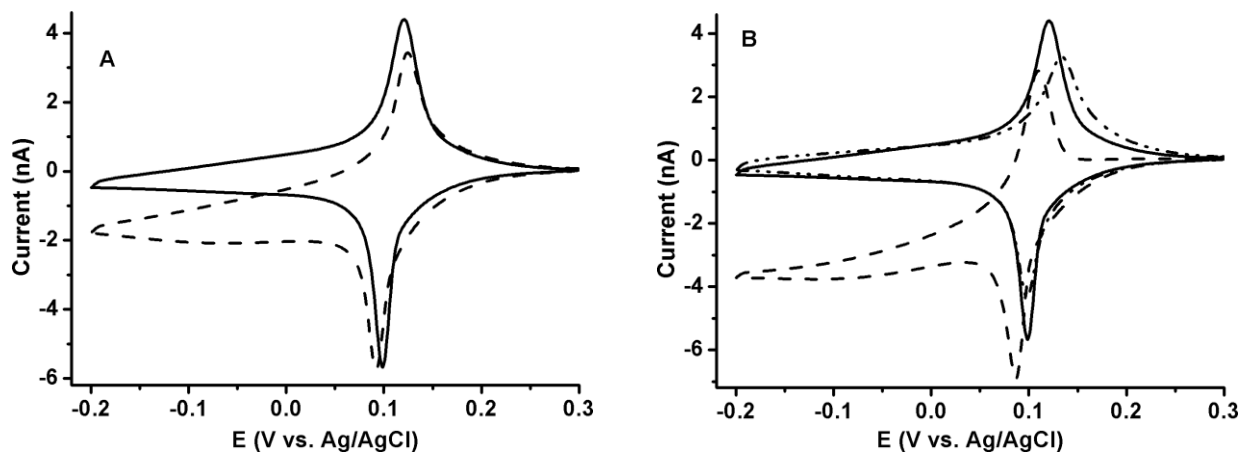

Figure A14 Cyclic voltammograms at PB modified gold microelectrode in potassium phosphate buffer pH 7.4 (solid lines), **A**) in 40% diluted Alce honey with buffer (dash line), **B**) after addition of 1 µg mL^{-1} GOx in to the 40% honey solution (dash line) and after addition of Catalase enzyme in to the honey containing solution (dash dot line). Scan rate 5 mV s^{-1}.

A2. Anti-tTG functionalization of Arrays of boron doped diamond nanoelectrodes

Besides the development of anti-tTG ECL immunosensor using nanoelectrode ensembles (presented in chapter 4), we examined the same protocol using arrays of boron doped diamond micro-/nano-electrodes (MNEA) which are manufactured by e-beam lithographic (EBL) technique. Each MNEA consisted of 16 small arrays of dots and bands (Figure A16). This experiment was conducted with the goal of utilizing the advantageous properties of BDD electrodes (e.g. wide potential window) and investigating the effect of electrodes' geometry and spacing on the ECL. Each line of the sample includes a series of four arrays in which the centre-to-centre distance (for dots) or pitch (for bands) is kept constant, while the radius of dots or bands width is increased. Note that all the arrays are electrically connected by the BDD under-layer.
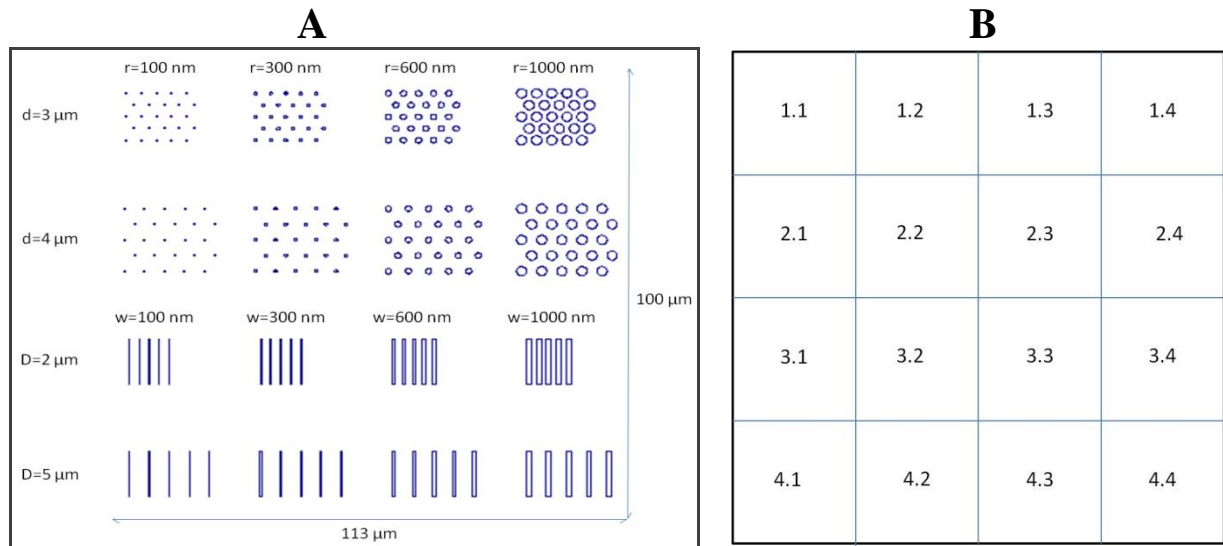

Figure A16 A) Schematic draw of MNEAP fabricated for preliminary ECL experiments: r is dots radius, d is centre-to-centre distance between dots, D represents the pitch between lines and w is the width of lines; **B**) Identification key of the NEAs in the platform.

A2.1 Experimental

Fabrication of the MNEA

A detail of the fabrication procedure is given in Virgilio *et al* 2013 [27]. Briefly; Si substrate coated with a 400 nm thick layer of BDD sample was treated with O_2 plasma for 15 seconds and

then a layer of PC was deposited on it by spin coating. Structures shown in Figure 16 were exposed by EBL and developed in 5M NaOH. Process parameters are reported in Table 1.

Table A1 Conditions used for the microfabrication of the MNEAP.

Resist	PC 3%
Spin Speed	2000 rpm
Bake	180 ^{o}C for 30 minutes
Dose	8000 μC cm^{-2}
Developer	5M NaOH
Temperature	35 ^{o}C

The electrochemical performances of the arrays were evaluated using a suitable redox mediator.

Immunosensor protocol

The same materials and immunosensor protocol as in Chapter 4 are used.

A2.2 Results and discussion

Typical CVs of a bare MNEA in Ru(bpy)$_3$$^{2+}$ at scan rates of 10, 50, and 100 mV s^{-1} are shown in Figure A17 the obtained CVs are sigmoidal in shape.
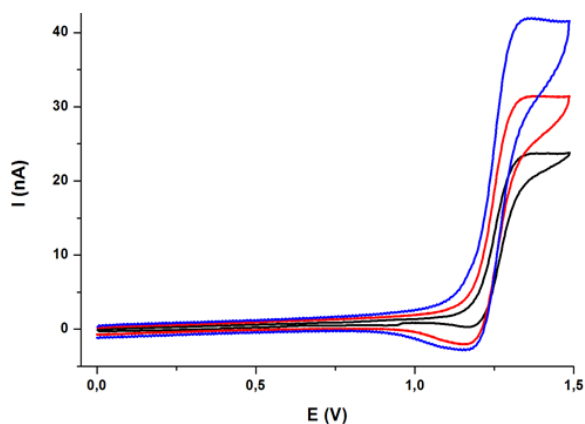

Figure A17 Cyclic voltammograms recorded at bare MNEA in PBS pH 7.4 containing 0.1 mM Ru(bpy)$_3$$^{2+}$ at scan rates of 10 (black line), 50 (red line) and 100 mV s^{-1} (blue line).

Figure A18 shows the CVs recorded at clean BDD electrode in phosphate buffer solution pH 7.4 before (blue line) and after (red line) addition of 100 mM TPrA. The increase in the oxidation peak of the CV after addition of TPrA is associated to the oxidation of TPrA at the electrode.
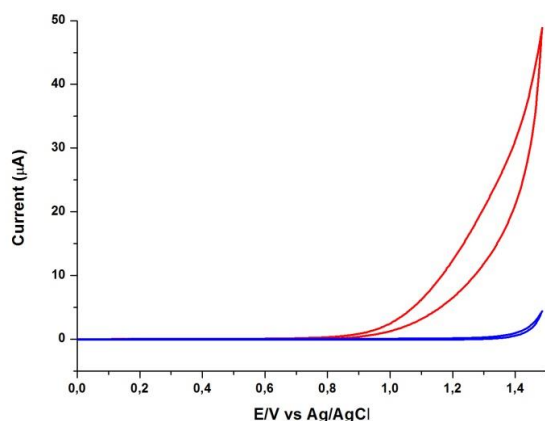
Figure A18 CVs at BDD electrode in PBS pH 7.4 (blue) and in the presence of 100 mM TPrA (red). Scan rate 50 mV s^{-1}.

The ECL and the corresponding CV recorded at the functionalized BDD electrodes are displayed in Figure A19. The ECL signal is weak and noisy. This emission might be resulted from the luminophore molecules adsorbed on the surface of the BDD electrodes which can allow the direct electrochemical oxidation of the luminophore. However, it is difficult to clearly locate where the luminophore is, i.e. on the PC part or on the BDD electrodes. Because of the very weak nature of the signal, no ECL could be imaged by the EM-CCD camera. In order to understand the reason for such weak ECL, further studies are on progress.
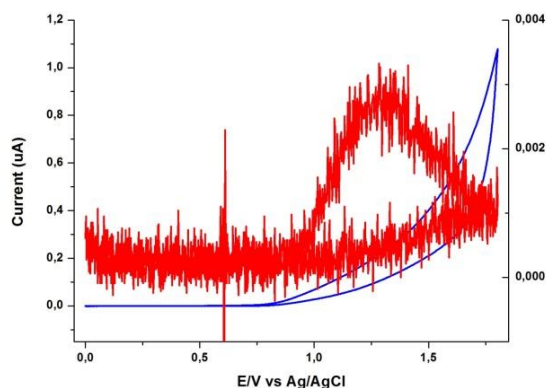

Figure A19 Cyclic voltammogram (blue) and ECL (red) recorded at the anti-tTG sensor of a NEA in 100 mM TPrA in PBS pH 7.4

References

[1] H. Meyer, H. Drewer, B. Ortindig, K. Cammann, *Anal. Chem.* 1995, **67**, 1164.

[2] B. Zhang, K.L. Adams, S.J. Luber, D.J. Eves, M.L. Heien, A.G. Ewing, *Anal. Chem.* 2008, **80**, 1394.

[3] B. Ross, K. Cammann, *Talanta* 1994, **41**, 977.

[4] J. Wang, R. Trouillon, Y. Lin, M. I. Svensson, A. G. Ewing, *Anal. Chem.* 2013, **85**, 5600.

[5] Y. Zhang, H. Wang, J. Nie, Y. Zhang, G. Shen, R. Yu, *Biosens. Bioelectron.* 2009, **25**, 34.

[6] W. Thormann, P. van den Bosch, A. M. Bond, *Anal. Chem.* 1985, **57**, 2764.

[7] V.B. Nascimento, M.A. Augelli, J.J. Pedrotti, I.G.R. Gutz, L. Angnes, *Electroanalysis* 1997, **9**, 335.

[8] B. A. Patel, M. Arundell, R.G.W. Quek, S.L.R. Harvey, I.R. Ellis, M.M. Florence, A.E.G. Cass, A.M. Schor, D. O'Hare, *Anal. Bioanal. Chem.* 2008, **390**, 1379.

[9] A. Benyoucef, F. Huerta, M.I. Ferrahi, E. Morallon, *J. Electroanal. Chem.* 2008, **624**, 245.

[10] M.P. Dash, M. Tripathy, A. Sasmal, G.C. Mohanty, P.L. Nayak, *J. Mater. Sci.* 2010, **45**, 3858.

[11] C. Chen, L. T. Campbell, S.E. Blair, D. A. Carter, *Front. Microbiol.* 2012, **3**, 1.

[12] K. Brudzynski, K. Abubaker, L. St-Martin, A. Castle, *Front.Microbiol.* 2011, **2**, 1.

[13] K. Derwinska, K. Miecznikowski, R. Koncki, P.J. Kulesza, S. Glab, M.A. Malik, *Electroanalysis* 2003, **15**, 1843.

[14] Z. Taleat, A. Ravalli, M. Mazloum-Ardakani, G. Marrazza, *Electroanalysis* 2013, **25**, 269.

[15] A.V. Mokrushina, M. Heim, E.E. Karyakina, A. Kuhn, A.A. Karyakin, *Electrochem. Commun.* 2013, **29**, 78.

[16] Y. Li, X. Liu, X. Zeng, Y. Liu, X. Liu, W. Wei, S. Luo, *Microchim. Acta* 2009, **165**, 393.

[17] I.L. de Mattos, L. Gorton, T. Ruzgas, A.A. Karyakin, *Anal. Sci.* 2000, **16**, 795.

[18] S. Daniele, P. Ugo, G.-A. Mazzocchin, *Anal. Chim. Acta* 1988, **211**, 325.

[19] M. Zhou, J. Heinze, *J. Phys. Chem. B* 1999, **103**, 8443.

[20] D.D. Ateh, H.A. Navsaria, P. Vadgama, *J. R. Soc. Interface* 2006, **3**, 741.

[21] S.M. Sayyah, M.M. El-Rabieh, S.S. Abd El-Rehim, R.E. Azooz, *J. Appl. Polym. Sci.* 2008, **109**, 1643.

[22] A. Preechaworapun, T.A. Ivandini, A. Suzuki, A. Fujishima, O. Chailapakul, Y. Einaga, *Anal. Chem.* 2008, **80**, 2077.

[23] B. Gupta, R. Prakash, *Polym. Adv. Technol.* 2011, **22**, 1982.

[24] A.V. Borisova, E.E. Karyakina, S. Cosnier, A.A. Kryakin, *Electroanalysis* 2009, **21**, 409.

[25] P.J. Taormina, B. A. Niemira, L.R. Beuchat, *Int. J. Food Microbiol.* 2001, **69**, 217.

[26] L.M. Bang, C. Buntting, P. Molan, *J. Altern. Complem. Med.* 2003, **9**, 267.

[27] F. Virgilio, M. Prasciolu, P. Ugo, M. Tormen, *Microelectron. Eng.* 2013, **111**, 320.

B. Scientific Publications and Communications

Publications

- <u>Henok B. Habtamu</u>, Paolo Ugo, Miniaturized Enzymatic Biosensor *via* Biofunctionalization of the Insulator of Nanoelectrode Ensembles. *Electroanalysis*, 2015, 27, 2187-2193.

- <u>Henok B. Habtamu</u>, Milica Sentic, Morena Silvestrini, Luigina De Leo, Tarcisio Not, Stéphane Arbualt, Dragan Manojlovic, Neso Sojic, Paolo Ugo, Highly Sensitive Electrochemiluminescent Detection of Celiac Disease Biomarkers at Gold Nanoelectrode Ensembles. *Anal. Chem.*, DOI: 10.1021/acs.analchem.

- <u>Henok B. Habtamu</u>, Paolo Ugo, Electrochemical Nanoimmunosensor for the detection of the Anti-tissue Transglutaminase IgG in Serum Samples of Pediatric Celiac Patients. *In Preparation.*

- Morena Silvestrini, <u>Henok Baye Habtamu</u>, Ligia Maria Moretto, Paolo Ugo (Conference proceeding). Electrochamical Biosensors for Sensitive Molecular Diagnosis. *Cross border Italy-Slovenia research,* e-ISBN 978-88-8303-573-9. EUT, 2014.

Oral Presentations on International Scientific Meetings

- The Bioelectrochemical Society (BES), XXIII International Symposium on Bioelectrochemistry and Bioenergetics, held in Malmoe (Sweden) from 14 to 18 June 2015. *"Nanoelectrode Ensembles-Based ECL Immunosensor for Celiac Disease Diagnosis."* <u>H.B. Habtamu</u>, M. Sentic, S. Arbault, D. Manojlovic, L. De Leo, T. Not, N. Sojic, P. Ugo.

- Ethiopian Pharmaceutical Association 34th Annual Conference, held in Addis Ababa (Ethiopia) on 23 and 24 August 2014. **"New Electrochemical Glucose Biosensor Using Gold Nanoelectrode Ensembles."** <u>H.B. Habtamu</u>, P. Ugo.

- 20th Young Investigators' Seminar on Analytical Chemistry (YISAC 2013), held in Maribor (Slovenia) from 26 to 29 June 2013. *"Characterization and Functionalization of Arrays of Individually Addressable Microelectrodes."* <u>H.B. Habtamu</u>, P. Ugo.

Poster Contributions on International Scientific Meetings

- International Meeting on Electrogenerated Chemiluminescence (ECL2014), held in Bertinoro (Italy) from 7 to 10 September 2014. *"A novel strategy for Electrogenereted Chemiluminescence Based Immunosensing Using Nanoelectrode Ensembles."* <u>H.B. Habtamu</u>, M. Sentic, S. Arbault, D. Manojlovic, L. De Leo, T. Not, N. Sojic, P. Ugo.

- SPSASECS, held in Sao Paulo (Brazil) from 7 to 14 December 2013. *"Electrochemically directed modification of each element in arrays of homemade individually addressable microelectrode arrays."* <u>H.B. Habtamu</u>, P. Ugo.

- SMCBS'13, held in Lochow Palace, Warsaw (Poland) from 8 to 12 November 2013. *"Electrochemically directed modification of each element in arrays of homemade individually addressable microelectrode arrays."* <u>H.B. Habtamu</u>, P. Ugo.